博士論文

Interaction of angular momentum between light and plasmonic nanostructure

(光とプラズモニックナノ構造間の角運動量の相互作用)

呉　安安

Contents

Acknowledgments

The work described in this dissertation was carried out between April 2017 and September 2020 at the Institute of Industrial Science, the University of Tokyo under the supervision of Professor Tsutomu Shimura and Research Associate Yoshito Tanaka. I would not have been able to complete the dissertation without the support of numerous individuals and institutions. I express my sincere gratitude to them here.

I am deeply grateful to Professor Tsutomu Shimura, Institute of Industrial Science, the University of Tokyo, for his constant encouragement, useful and smart advice on my research. His excellent insight and guidance based on wealthy knowledge led me to the proper direction in this work. I learned a lot of useful knowledge in science, not only in optics, during his lectures and discussions.

I am greatly indebted to Research Associate Yoshito Tanaka, Institute of Industrial Science, the University of Tokyo, for his smart and useful advice on all the aspects of my research. His physical sense enriched this work and gave me good hints for better research activity. His views on research life and planning are very enlightening to me. I appreciate for his kind help and useful advice on the manuscript preparation.

I would like to express my sincere gratitude to Professor Satoshi Ashihara, Institute of Industrial Science, the University of Tokyo, for his constant encouragement and guidance. The discussions we had and his helpful advice have brought a lot of inspiration to my research.

I would like to express my sincere thanks to Professor Iwamoto Satoshi, Institute of Industrial Science, the University of Tokyo, Associate Professor Yoshioka Kosuke, Graduate School of Engineering, the University of Tokyo, and Chief Scientist Takuo Tanaka, Metamaterials Laboratory, RIKEN Cluster for Pioneering Research, for their acceptance to be referees of my doctoral dissertation with pleasure. Their constructive suggestions

and comments based on wealthy experiences enriched my work a great deal.

I am really grateful to Dr. Sanpon Vantasin, a former postdoctor of Shimura laboratory, for giving me a lot of advice on the modeling in COMSOL Multiphysics.

I would like to thank Technical Officical Kumiko Kamada and Secretary Yoshimi Tachibana for their assistance on laboratory affairs and constant encouragement.

I would like to thank the technical staffs of VLSI Design and Education Center (VDEC) at the University of Tokyo for their kind advice on the fabrication of nanostructures.

I am really grateful to Mr. Ryo Omori, a former member of Shimura laboratory, for his kind help in my early doctoral period. He was my tutor and helped me adapt to the life in Japan. He helped me a lot in the preparation of my doctoral entrance examination. I appreciate our friendship very much.

I am really grateful to Mr. Ryoma Fukuhara, a member of Shimura laboratory, for his useful advice on my research and kind help in my life. He also helped me a lot in the preparation of my doctoral entrance examination. We often discuss our research together. He can always put forward a lot of good ideas, which bring me a lot of inspiration. I appreciate our friendship very much.

I am really grateful to Mr. Tomoya Kimura, a member of Shimura laboratory, for his useful advice on the fabrication of nanostructures and COMSOL Multiphysics.

I would like to thank my colleagues in Shimura laboratory and Ashihara laboratory: Mr. M. Shigaki, Mr. S. Hirayama, Mr. J. Won, Mr. K. Niihara, Dr. K. Imasaka, Mr. S. Sakama, Ms. X. Luo, Mr. D. kim, Ms. H. Nishimoto, Dr. J. Liu, Dr. F. Fan, Dr. Y. Liu, Dr. X. Xiao, Dr. G. Dayal, Dr. I. Morichika, Mr. D. Okazaki, Mr. W. Song, Mr. K. Arai, Mr. T. Takahashi, Dr. A. Sakurai, Mr. S. Kitade, Mr. T. Kaji, Mr. W. Su, Mr. Y. He, and Mr. S. Chen.

Besides the individuals mentioned above, many people helped me, for example through discussions in conferences and symposiums. I would like to thank them for their kind help.

Last but not the least, I am deeply thankful to my family for their love, support, and sacrifices. Without them, this dissertation would never have been written.

Chapter 1

Introduction

1.1 Background

Angular momentum, as a basic property to describe the rotation of light, can be separated into spin angular momentum (SAM) associated with the polarization of light and orbital angular momentum (OAM) determined by the spatial degrees of freedom of light [1–3]. The SAM was first explicitly considered by Poynting and experimentally demonstrated by Beth in 1936 [4, 5]. However, it was a long time before the idea of the OAM of light was pioneered by Allen et al. in 1992 [6]. They discovered that a light beam with a helical phase front carries OAM. From then on, the study of optical angular momentum has developed into a flourishing field of research, leading to a rich variety of research and applications [7–11].

The interaction of angular momentum between light and matter gives rise to a variety of striking optical phenomena and has been attracting extensive attention due to the physical significance in optics. Especially, with the development of plasmonics and nanotechnology, these studies have been greatly promoted in recent years because of the strong interaction between light and plasmonic structures. Therefore, in this dissertation, we carry out our work based on the three interesting phenomena in the interaction of angular momentum between light and matter.

■ Optical spin-orbit interaction

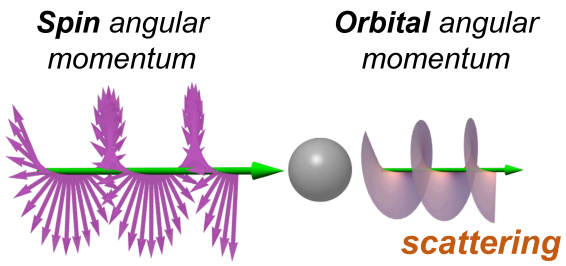

Figure 1.1: Schematic illustration of spin-orbit interaction of light

When light interacts with matter, there is a transformation between the spin and orbital parts of the angular momentum carried by the light as shown in Figure 1.1. This spin-obit interaction of light is highly related to the polarization and spatial degrees of freedom of light, which plays a crucial role in the manipulation and control of light. Most of the spin-orbit interaction phenomena appear at subwavelength scales [12–14]. Therefore, numerous spin-orbit interaction effects can be observed in the research fields of nano-optics, photonics, and plasmonics [15–19]. The description of the polarization and spatial properties of light at subwavelength scales provides a new viewpoint for the physical insight at subwavelength scales. Moreover, the interaction between spin and orbital degrees of freedom makes it possible for optical nano-devices to have novel functionalities. In the past three decades, with the rapid development of nano-optics, photonics, and plasmonics, the spin-orbit interaction of light has been attracting rapidly growing interest due to its promising potential in many practical applications, such as the optical manipulation of nanoparticles and molecules [20,21], subwavelength optical probing [22], and generation of vortex beams [23,24].

■ Optical torque

Optical torque induced by the angular momentum transfer in light-matter interaction enables a particle to rotate (as shown in Figure 1.2) through both the absorption and scattering [25–27]. It provides a rotational mechanical degree of freedom to manipulate objects. Particularly, the localized surface plasmon resonances (LSPRs) in noble metal nanostructures can significantly enhance the absorption and scattering in light-matter interaction, enabling these structures to overcome the Brownian motion and the other fluctuations

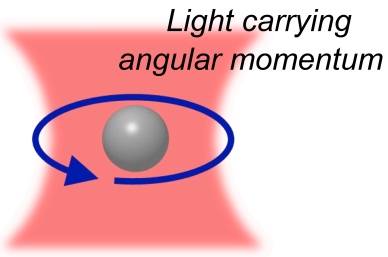

Figure 1.2: Schematic illustration of optical torque

for the manipulation. The magnitude of the optical torque is strongly dependent on the LSPR properties of the plasmonic structures [27]. It has been reported that the optical torque on individual plasmonic nanoparticle can reach hundreds of $pN \cdot nm$ [28], which is sufficient to propel nanomachines and to address single-molecule processes in biological matter. Therefore, optically driven plasmonic nanostructures establish an extremely interesting platform for nanomechanical engineering and sensing applications. Over many decades, optical torque has been attracting widespread attention owing to its crucial role in optical manipulations, with a variety of applications in atomic and molecular physics, nanotechnology, and biology [29–33].

■ Chiroptical response

Chiral objects are those objects which cannot be superimposed with their mirror image [34, 35]. Chirality is very common in our daily life as well as microscopically down to molecular levels, reflecting a fundamental property of materials. Many biomolecules, such as amino acids, nucleotides, and sugars, are inherently chiral. Chiral material can manifest a chiroptical response via the different absorption of left- and right-handed cir-

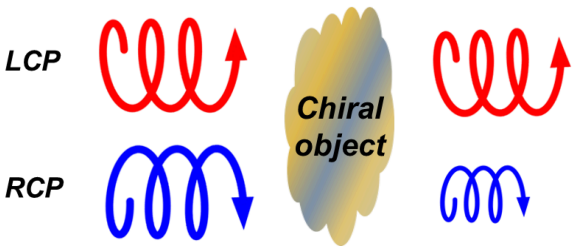

Figure 1.3: Schematic illustration of the chiroptical response

cularly polarized light as shown in Figure 1.3. It can be evaluated by the dissymmetry factor (g factor) defined as [36, 37]

$$g_{abs} = \frac{A^l_{abs} - A^r_{abs}}{A^l_{abs} + A^r_{abs}},, \tag{1.1}$$

where A^l_{abs} and A^r_{abs} are the absorption cross sections for left- and right-handed circularly polarized light, respectively. The chiroptical phenomenon is of great significance in fundamental research and successfully applied in many different fields [38–40]. However, this chiroptical response is inherently weak for most natural chiral materials due to the small size of molecules [41, 42], which limits its further studies and applications. Recently, with the advancement of nanotechnology, the progress in plasmonics provides an effective route for the g factor enhancement. It is now possible to artificially create chiral plasmonic nanostructures or metasurfaces, which have been attracting widely scientific interest because they can strongly interact with circularly polarized light [43–48].

1.2 Motivation and objectives of this study

As mentioned above, in recent years, the rapid development of plasmonics and nano-optics has extremely facilitated the study of the interaction of angular momentum between light and matter with numerous applications. However, in such a large research field, there are still many research topics that have not been studied. In this dissertation, based on the three interesting phenomena introduced above in the interaction of angular momentum between light and plasmonic nanostructures, we study the urgent issues in each phenomenon to improve the insights into the physics of light-matter interaction and to expand the applications.

■ Quantification of the optical spin-orbit transformation in light-matter interaction

The spin-orbit interaction of light has been attracting rapidly growing interest due to its promising potential in nano-optics, photonics, and plasmonics [15–24]. Therefore, it is of great significance to find a method that can separately analyze the SAM and OAM in the interaction between light and matter. As shown in Figure 1.1, when a circularly polarized

light carrying SAM interacts with a nanosphere, the scattered light from the nanosphere possesses OAM. In this case, because the nanosphere is a very simple nanoparticle illuminated by a simply structured incident light, the transformation between SAM and OAM can be easily analyzed based on the model of rotating dipole scattering [49,50]. However, when we consider a complex-shaped nanoparticle or incident light, the quantification of the spin-orbit transformation would be very difficult because it is difficult to find an effective model to evaluate the angular momentum, especially the OAM, in the field. In other words, thus far, there is no general way to quantify the optical spin-orbit transformation in light-matter interaction.

In this topic, therefore, our objective is to find a method that can realize the quantification of the spin-orbit transformation, which will greatly benefit the design and analysis of a spin-orbit interaction system. To realize this, we should know the changes of the SAM and OAM in the light-matter interaction. These are induced by the transfers of SAM and OAM between light and matter, which can be clearly described by their continuity equations. It is worth pointing out that the total angular momentum, as the sum of the SAM and the OAM, is a conserved quantity. The continuity equation for total angular momentum is a well-known continuity equation, which explicates the transfer of total angular momentum between light and matter. Consequently, in order to realize our objective, we should find the continuity equation for SAM or OAM.

■ Optical torque between twisted metal nanorods induced by plasmon coupling

As introduced in the background part, many remarkable achievements have been made in the study of optical torque, however, these studies mainly focus on an individual nanoparticle. Few works are trying to study the optical torque in a multi-particle system. When two nanoparticles are close to each other, plasmon coupling occurs due to the strong interaction between them, resulting in an appearance of two plasmon coupling modes different from individual constituents and a drastically enhanced near field in the narrow gap separating them [51–53]. In some previous studies, it has been reported that the plasmon coupling can produce a large interaction optical force on each nanoparticle [54–56], which plays a significant role in the optical arrangement. Intuitively, interaction optical torque is also very important in the optical arrangement because it provides another mechanical

degree of freedom for the manipulation of particles. Therefore, it is indispensable to study the interaction optical torque in a plasmon coupling system.

In this topic, our objective is to study the interaction optical toque induced by the plasmon coupling. Here, our study is based on a dimer of twisted metal nanorods because it is the simplest dimer system that can easily observe the plasmon coupling modes, which can simplify the analysis of the physical mechanism. In this dimer, we investigate the plasmon coupling between the nanorods depending on its configuration which is determined by the gap size and twisted angle between the two nanorods. Then, we study the interaction optical torque between the nanorods and the relation with the plasmon coupling.

■ Enhancement of *g* factor of twisted metal nanorods by plasmon coupling

Chiral plasmonic structures with large *g* factor have shown promising potential for detecting and sensing applications [48,57,58], negative refraction materials [59–61], and optical elements with strong chiroptical effects [45,46]. Therefore, the study of the enhancement of *g* factor will be of great significance to improve the insights into controllable chirality of nanostructure and to expand its applications. However, in the previous studies, almost all the studies of the *g* factor enhancement are limited to the geometry design of the structure. Inspired by the results in the second topic concerning the SAM in the interaction between light and the twisted metal nanorods, it implies that the plasmon coupling between the twisted nanorods results in a strong chiroptical response of the structure. This may provide a new route for the *g* factor enhancement.

In this topic, therefore, our objective is to experimentally demonstrate that the plasmon coupling can enhance the *g* factor of the twisted nanorods. Firstly, we try to fabricate the twisted nanorods structures with different gap sizes and twisted angles. Then, we experimentally characterize the plasmon coupling and *g* factor of the twisted nanorods structure depending on the gap size and twisted angle. The relation between the plasmon coupling and *g* factor will be discussed to show a new perspective for the study of *g* factor enhancement.

1.3 Synopses of this dissertation

This dissertation is composed of six chapters.

In Chapter 2, we review two fundamentals of this dissertation: angular momentum of light and localized surface plasmon.

In Chapter 3, by introducing the quantity of optical chirality density, the continuity equation for spin angular momentum is derived, providing a method to realize the quantification of the optical spin-orbit transformation in light-matter interaction

In Chapter 4, based on the structure of twisted gold nanorods, we investigate the optical torques on the twisted nanorods induced by the plasmon coupling between them. The rotational behaviors of the nanorod at different plasmon modes induced by the optical torques are analyzed.

In Chapter 5, inspired by the results in Chapter 4, we experimentally demonstrate that plasmon coupling can enhance the g factor of the dimer of twisted nanorods. The relation between the plasmon coupling and g factor is discussed.

In Chapter 6, we summarize our works and describe the prospects.

References

[1] K. Y. Bliokh and F. Nori, "Transverse and longitudinal angular momenta of light," *Phys. Rep.*, vol. 592, pp. 1–38, 2015.

[2] I. Bialynicki-Birula and Z. Bialynicka-Birula, "Canonical separation of angular momentum of light into its orbital and spin parts," *J. Opt.*, vol. 13, no. 6, p. 064014, 2011.

[3] S. M. Barnett, L. Allen, R. P. Cameron, C. R. Gilson, M. J. Padgett, F. C. Speirits, and A. M. Yao, "On the natures of the spin and orbital parts of optical angular momentum," *J. Opt.*, vol. 18, no. 6, p. 064004, 2016.

[4] J. H. Poynting, "The wave-motion of a revolving shaft, and a suggestion as to the angular momentum in a beam of circularly-polarized light," *Proc. R. Soc. Lond. Ser. A*, vol. 82, pp. 560–567, 1909.

[5] R. A. Beth, "Mechanical detection and measurement of the angular momentum of light," *Phys. Rev.*, vol. 50, no. 2, pp. 115–125, 1936.

[6] L. Allen, M. W. Beijersbergen, R. Spreeuw, and J. Woerdman, "Orbital angular momentum of light and the transformation of laguerre-gaussian laser modes," *Phys. Rev. A*, vol. 45, no. 11, p. 8185, 1992.

[7] M. Antognozzi, C. R. Bermingham, R. L. Harniman, S. Simpson, J. Senior, R. Hayward, H. Hoerber, M. R. Dennis, A. Y. Bekshaev, K. Y. Bliokh, and F. Nori, "Direct measurements of the extraordinary optical momentum and transverse spin-dependent force using a nano-cantilever," *Nat. Physics*, vol. 12, no. 8, pp. 731–735, 2016.

[8] L. Liu, A. Di Donato, V. Ginis, S. Kheifets, A. Amirzhan, and F. Capasso, "Three-dimensional measurement of the helicity-dependent forces on a mie particle," *Phys. Rev. Lett.*, vol. 120, no. 22, p. 223901, 2018.

[9] L. Allen, M. J. Padgett, and M. Babiker, "The orbital angular momentum of light," *Prog. Opt.*, vol. 39, pp. 291–372, 1999.

[10] S. Franke-Arnold, L. Allen, and M. J. Padgett, "Advances in optical angular momentum," *Laser Photonics Rev.*, vol. 2, no. 4, pp. 299–313, 2008.

[11] J. Ng, Z. Lin, and C. Chan, "Theory of optical trapping by an optical vortex beam," *Phys. Rev. Lett.*, vol. 104, no. 10, p. 103601, 2010.

[12] D. O ' connor, P. Ginzburg, F. J. Rodríguez-Fortuño, G. A. Wurtz, and A. V. Zayats, "Spin–orbit coupling in surface plasmon scattering by nanostructures," *Nat. Commun.*, vol. 5, no. 1, pp. 1–7, 2014.

[13] B. Le Feber, N. Rotenberg, and L. Kuipers, "Nanophotonic control of circular dipole emission," *Nat. Commun.*, vol. 6, no. 1, pp. 1–6, 2015.

[14] N. Shitrit, I. Bretner, Y. Gorodetski, V. Kleiner, and E. Hasman, "Optical spin hall effects in plasmonic chains," *Nano Lett.*, vol. 11, no. 5, pp. 2038–2042, 2011.

[15] K. Y. Bliokh, F. J. Rodríguez-Fortuño, F. Nori, and A. V. Zayats, "Spin–orbit interactions of light," *Nat. Photonics*, vol. 9, no. 12, p. 796, 2015.

[16] S. Sukhov, V. Kajorndejnukul, R. R. Naraghi, and A. Dogariu, "Dynamic consequences of optical spin–orbit interaction," *Nat. Photonics*, vol. 9, no. 12, p. 809, 2015.

[17] K. Y. Bliokh, D. Smirnova, and F. Nori, "Quantum spin hall effect of light," *Science*, vol. 348, no. 6242, pp. 1448–1451, 2015.

[18] F. Cardano and L. Marrucci, "Spin–orbit photonics," *Nat. Photonics*, vol. 9, no. 12, pp. 776–778, 2015.

[19] J. E. Vázquez-Lozano and A. Martínez, "Classical emergence of intrinsic spin-orbit interaction of light at the nanoscale," *Phys. Rev. A*, vol. 97, no. 3, p. 033804, 2018.

[20] F. J. Rodríguez-Fortuño, N. Engheta, A. Martínez, and A. V. Zayats, "Lateral forces on circularly polarizable particles near a surface," *Nat. Commun.*, vol. 6, p. 8799, 2015.

[21] H. Adachi, S. Akahoshi, and K. Miyakawa, "Orbital motion of spherical microparticles trapped in diffraction patterns of circularly polarized light," *Phys. Rev. A*, vol. 75, no. 6, p. 063409, 2007.

[22] O. G. Rodríguez-Herrera, D. Lara, K. Y. Bliokh, E. A. Ostrovskaya, and C. Dainty, "Optical nanoprobing via spin-orbit interaction of light," *Phys. Rev. Lett.*, vol. 104, no. 25, p. 253601, 2010.

[23] L. Huang, X. Chen, H. Mühlenbernd, G. Li, B. Bai, Q. Tan, G. Jin, T. Zentgraf, and S. Zhang, "Dispersionless phase discontinuities for controlling light propagation," *Nano Lett.*, vol. 12, no. 11, pp. 5750–5755, 2012.

[24] E. Karimi, S. A. Schulz, I. De Leon, H. Qassim, J. Upham, and R. W. Boyd, "Generating optical orbital angular momentum at visible wavelengths using a plasmonic metasurface," *Light: Sci. Appl.*, vol. 3, no. 5, pp. e167–e167, 2014.

[25] D. Gao, W. Ding, M. Nieto-Vesperinas, X. Ding, M. Rahman, T. Zhang, C. Lim, and C.-W. Qiu, "Optical manipulation from the microscale to the nanoscale: fundamentals, advances and prospects," *Light: Sci. Appl.*, vol. 6, no. 9, pp. e17039–e17039, 2017.

[26] M. Padgett and R. Bowman, "Tweezers with a twist," *Nat. photonics*, vol. 5, no. 6, pp. 343–348, 2011.

[27] Y. E. Lee, K. H. Fung, D. Jin, and N. X. Fang, "Optical torque from enhanced scattering by multipolar plasmonic resonance," *Nanophotonics*, vol. 3, no. 6, pp. 343–350, 2014.

[28] P. Ruijgrok, N. Verhart, P. Zijlstra, A. Tchebotareva, and M. Orrit, "Brownian fluctuations and heating of an optically aligned gold nanorod," *Phys. Rev. Lett.*, vol. 107, no. 3, p. 037401, 2011.

[29] A. Ashkin, "History of optical trapping and manipulation of small-neutral particle, atoms, and molecules," *IEEE J. Sel. Top. Quantum Electron.*, vol. 6, no. 6, pp. 841–856, 2000.

[30] M. Liu, T. Zentgraf, Y. Liu, G. Bartal, and X. Zhang, "Light-driven nanoscale plasmonic motors," *Nat. Nanotechnol.*, vol. 5, no. 8, pp. 570–573, 2010.

[31] M. Friese, T. Nieminen, N. Heckenberg, and H. Rubinsztein-Dunlop, "Optical alignment and spinning of laser-trapped microscopic particles," *Nature*, vol. 394, no. 6691, pp. 348–350, 1998.

[32] R. W. Bowman and M. J. Padgett, "Optical trapping and binding," *Rep. Prog. Phys.*, vol. 76, no. 2, p. 026401, 2013.

[33] W. D. Phillips, "Nobel lecture: Laser cooling and trapping of neutral atoms," *Rev. Mod. Phys.*, vol. 70, no. 3, p. 721, 1998.

[34] G. H. Wagnière, *On chirality and the universal asymmetry: reflections on image and mirror image*. John Wiley & Sons, 2007.

[35] W. T. B. Kelvin, *The molecular tactics of a crystal*. Clarendon Press, 1894.

[36] T. Liu, L. V. Besteiro, T. Liedl, M. A. Correa-Duarte, Z. Wang, and A. O. Govorov, "Chiral plasmonic nanocrystals for generation of hot electrons: Toward polarization-sensitive photochemistry," *Nano Lett.*, vol. 19, no. 2, pp. 1395–1407, 2019.

[37] M. Wakabayashi, S. Yokojima, T. Fukaminato, K.-i. Shiino, M. Irie, and S. Nakamura, "Anisotropic dissymmetry factor, g: Theoretical investigation on single molecule chiroptical spectroscopy," *J. Phys. Chem. A*, vol. 118, no. 27, pp. 5046–5057, 2014.

[38] H. Tsukube and S. Shinoda, "Lanthanide complexes in molecular recognition and chirality sensing of biological substrates," *Chem. Rev.*, vol. 102, no. 6, pp. 2389–2404, 2002.

[39] H. Rhee, Y.-G. June, J.-S. Lee, K.-K. Lee, J.-H. Ha, Z. H. Kim, S.-J. Jeon, and M. Cho, "Femtosecond characterization of vibrational optical activity of chiral molecules," *Nature*, vol. 458, no. 7236, pp. 310–313, 2009.

[40] A. Ben Moshe, D. Szwarcman, and G. Markovich, "Size dependence of chiroptical activity in colloidal quantum dots," *ACS Nano*, vol. 5, no. 11, pp. 9034–9043, 2011.

[41] L. D. Barron, *Molecular light scattering and optical activity*. Cambridge University Press, 2009.

[42] Y. Tang and A. E. Cohen, "Enhanced enantioselectivity in excitation of chiral molecules by superchiral light," *Science*, vol. 332, no. 6027, pp. 333–336, 2011.

[43] M. Kuwata-Gonokami, N. Saito, Y. Ino, M. Kauranen, K. Jefimovs, T. Vallius, J. Turunen, and Y. Svirko, "Giant optical activity in quasi-two-dimensional planar nanostructures," *Phys. Rev. Lett.*, vol. 95, no. 22, p. 227401, 2005.

[44] M. Hentschel, M. Schäferling, X. Duan, H. Giessen, and N. Liu, "Chiral plasmonics," *Sci. Adv.*, vol. 3, no. 5, p. e1602735, 2017.

[45] M. Decker, R. Zhao, C. Soukoulis, S. Linden, and M. Wegener, "Twisted split-ring-resonator photonic metamaterial with huge optical activity," *Opt. Lett.*, vol. 35, no. 10, pp. 1593–1595, 2010.

[46] N. Yu, F. Aieta, P. Genevet, M. A. Kats, Z. Gaburro, and F. Capasso, "A broadband, background-free quarter-wave plate based on plasmonic metasurfaces," *Nano Lett.*, vol. 12, no. 12, pp. 6328–6333, 2012.

[47] M. Hentschel, M. Schäferling, T. Weiss, N. Liu, and H. Giessen, "Three-dimensional chiral plasmonic oligomers," *Nano Lett.*, vol. 12, no. 5, pp. 2542–2547, 2012.

[48] E. Hendry, T. Carpy, J. Johnston, M. Popland, R. Mikhaylovskiy, A. Lapthorn, S. Kelly, L. Barron, N. Gadegaard, and M. Kadodwala, "Ultrasensitive detection and characterization of biomolecules using superchiral fields," *Nat. Nanotechnol.*, vol. 5, no. 11, pp. 783–787, 2010.

[49] C. Schwartz and A. Dogariu, "Conservation of angular momentum of light in single scattering," *Opt. Express*, vol. 14, no. 18, pp. 8425–8433, 2006.

[50] K. Y. Bliokh, E. A. Ostrovskaya, M. A. Alonso, O. G. Rodríguez-Herrera, D. Lara, and C. Dainty, "Spin-to-orbital angular momentum conversion in focusing, scattering, and imaging systems," *Opt. Express*, vol. 19, no. 27, pp. 26132–26149, 2011.

[51] W. Rechberger, A. Hohenau, A. Leitner, J. Krenn, B. Lamprecht, and F. Aussenegg, "Optical properties of two interacting gold nanoparticles," *Opt. Commun.*, vol. 220, no. 1-3, pp. 137–141, 2003.

[52] K.-H. Su, Q.-H. Wei, X. Zhang, J. Mock, D. R. Smith, and S. Schultz, "Interparticle coupling effects on plasmon resonances of nanogold particles," *Nano Lett.*, vol. 3, no. 8, pp. 1087–1090, 2003.

[53] L. Gunnarsson, T. Rindzevicius, J. Prikulis, B. Kasemo, M. Käll, S. Zou, and G. C. Schatz, "Confined plasmons in nanofabricated single silver particle pairs: experimental observations of strong interparticle interactions," *J. Phys. Chem. B*, vol. 109, no. 3, pp. 1079–1087, 2005.

[54] H. Xu and M. Käll, "Surface-plasmon-enhanced optical forces in silver nanoaggregates," *Phys. Rev. Lett*, vol. 89, no. 24, p. 246802, 2002.

[55] V. Demergis and E.-L. Florin, "Ultrastrong optical binding of metallic nanoparticles," *Nano Lett.*, vol. 12, no. 11, pp. 5756–5760, 2012.

[56] N. A. Kostina, D. A. Kislov, A. N. Ivinskaya, A. Proskurin, D. N. Redka, A. Novitsky, P. Ginzburg, and A. S. Shalin, "Nanoscale tunable optical binding mediated by hyperbolic metamaterials," *ACS Photonics*, vol. 7, no. 2, pp. 425–433, 2019.

[57] W. Li, Z. J. Coppens, L. V. Besteiro, W. Wang, A. O. Govorov, and J. Valentine, "Circularly polarized light detection with hot electrons in chiral plasmonic metamaterials," *Nat. Commun.*, vol. 6, no. 1, pp. 1–7, 2015.

[58] C. Jack, A. S. Karimullah, R. Leyman, R. Tullius, V. M. Rotello, G. Cooke, N. Gadegaard, L. D. Barron, and M. Kadodwala, "Biomacromolecular stereostructure me-

diates mode hybridization in chiral plasmonic nanostructures," *Nano Lett.*, vol. 16, no. 9, pp. 5806–5814, 2016.

[59] J. Pendry, "A chiral route to negative refraction," *Science*, vol. 306, no. 5700, pp. 1353–1355, 2004.

[60] S. Zhang, Y.-S. Park, J. Li, X. Lu, W. Zhang, and X. Zhang, "Negative refractive index in chiral metamaterials," *Phys. Rev. Lett.*, vol. 102, no. 2, p. 023901, 2009.

[61] E. Plum, J. Zhou, J. Dong, V. Fedotov, T. Koschny, C. Soukoulis, and N. Zheludev, "Metamaterial with negative index due to chirality," *Phys. Rev. B*, vol. 79, no. 3, p. 035407, 2009.

Chapter 2

Fundamentals: angular momentum of light and localized surface plasmon

2.1 Introduction

In this chapter, we summarize the fundamental facts and phenomena that form the basis of this study. In Section 2.2, we briefly review the concept of optical angular momentum. Starting with Maxwell's equations, we look at the conservation laws for energy, linear momentum, and angular momentum in a system of a charged particle in an electromagnetic field. Then, we discuss the theoretical derivation of separating the angular momentum into spin and orbit parts. In Section 2.3, we introduce the second essential knowledge in our study, that is, the localized surface plasmon in metal nanoparticles. The basic physics of localized surface plasmon is described by exploring the resonance condition in the interaction between metal nanoparticles and an electromagnetic field.

2.2 Angular momentum of light

2.2.1 Maxwell's equations and conservation laws

We start from Maxwell's equations to describe the properties of electric and magnetic fields and how they relate to each other in the following form [1]:

$$\nabla \cdot \boldsymbol{\mathcal{D}} = \rho, \tag{2.1}$$

$$\nabla \cdot \boldsymbol{\mathcal{B}} = 0, \tag{2.2}$$

$$\nabla \times \boldsymbol{\mathcal{E}} = \frac{\partial \boldsymbol{\mathcal{B}}}{\partial t}, \tag{2.3}$$

$$\nabla \times \boldsymbol{\mathcal{H}} = \frac{\partial \boldsymbol{\mathcal{D}}}{\partial t} + \boldsymbol{j}, \tag{2.4}$$

where $\boldsymbol{\mathcal{E}}$ is the electric field, $\boldsymbol{\mathcal{D}}$ is the electric displacement, $\boldsymbol{\mathcal{H}}$ is the magnetic field, $\boldsymbol{\mathcal{B}}$ is the magnetic induction, ρ and $\boldsymbol{j}$ are the external charge density and current density. The electromagnetic properties of a medium are further linked together via the polarization $\boldsymbol{\mathcal{P}}$ and magnetization $\boldsymbol{\mathcal{M}}$ by

$$\boldsymbol{\mathcal{D}} = \varepsilon_0 \boldsymbol{\mathcal{E}} + \boldsymbol{\mathcal{P}}, \tag{2.5}$$

$$\boldsymbol{\mathcal{H}} = \mu_0^{-1} \boldsymbol{\mathcal{B}} - \boldsymbol{\mathcal{M}}, \tag{2.6}$$

where ε_0 and μ_0 are the dielectric permittivity and magnetic permeability of vacuum, respectively. Eq. (2.1)~Eq. (2.6) builds the foundation of the classical electromagnetic theory. These equations provide a complete description of the classical dynamics of interacting charged particles and electromagnetic fields by combining with the Lorentz force equation and Newton's second law of motion.

In an isotropic, linear, and non-magnetic medium (typically considered in this dissertation), we can define the following relation

$$\boldsymbol{\mathcal{D}} = \varepsilon_0 \varepsilon_r \boldsymbol{\mathcal{E}} = \varepsilon \boldsymbol{\mathcal{E}}, \tag{2.7}$$

$$\boldsymbol{\mathcal{B}} = \mu_0 \mu_r \boldsymbol{\mathcal{H}} = \mu \boldsymbol{\mathcal{H}}, \tag{2.8}$$

where ε_r is the dielectric constant or relative permittivity, ε is the dielectric permittivity, $\mu_r = 1$ is the relative magnetic permeability of the non-magnetic medium, and μ is the magnetic permeability. In this case, the relation between $\boldsymbol{\mathcal{P}}$ and $\boldsymbol{\mathcal{E}}$ can be described by $\boldsymbol{\mathcal{P}} = \varepsilon_0 \chi \boldsymbol{\mathcal{E}}$, where χ is the dielectric susceptibility.

In the following, we will discuss the mechanical interaction between light and a

charged particle. In relation to an electromagnetic field in vacuum, we regard the particle with volume V enclosed by a surface S as a distribution of charges with density $\rho(\mathbf{r},t)$ and currents with density $\boldsymbol{j}(\mathbf{r},t)$. For more details, please refer to Refs [1, 2]

■ Poynting's theorem

We first consider the conservation of energy which is often called Poynting's theorem. The rate of work done on the charged particle by the field can be expressed as $\int_V \boldsymbol{j} \cdot \boldsymbol{\mathcal{E}}\, dV$, which describes a conversion of electromagnetic energy into mechanical or thermal energy. This must correspond to a rate of the decrease of energy in the electromagnetic field. Therefore, by using Maxwell's equations, we can get the Poynting's theorem in integral form as

$$\int_V (\frac{\partial U}{\partial t} + \nabla \cdot \boldsymbol{\mathcal{S}})\, dV = -\int_V \boldsymbol{j} \cdot \boldsymbol{\mathcal{E}}\, dV, \tag{2.9}$$

$$U = \frac{1}{2}(\boldsymbol{\mathcal{E}} \cdot \boldsymbol{\mathcal{D}} + \boldsymbol{\mathcal{B}} \cdot \boldsymbol{\mathcal{H}}), \tag{2.10}$$

$$\boldsymbol{\mathcal{S}} = \boldsymbol{\mathcal{E}} \times \boldsymbol{\mathcal{H}}, \tag{2.11}$$

where U is the energy density of the electromagnetic field. The vector $\boldsymbol{\mathcal{S}}$ can be regarded as the energy flux density, which is often called the Poynting vector. Eq. (2.9) can be rewritten into the form of a differential continuity equation for energy,

$$\frac{\partial U}{\partial t} + \nabla \cdot \boldsymbol{\mathcal{S}} = -\boldsymbol{j} \cdot \boldsymbol{\mathcal{E}}, \tag{2.12}$$

which is the most elementary continuity equation that explicates the exchange of energy between the field and sources (charges and currents).

■ Conservation of linear momentum

Similarly, we can consider the conservation of linear momentum. Based on the Lorentz force equation and Newton's second law of motion, the total Lorentz force on the charged particle can be expressed as

$$\frac{d}{dt}\mathbf{P}_{mech} = \int_V (\rho\boldsymbol{\mathcal{E}} + \boldsymbol{j} \times \boldsymbol{\mathcal{B}})\, dV, \tag{2.13}$$

where $\mathbf{P}_{mech}$ is the mechanical linear momentum of the particle. By using Maxwell's equations in vacuum, we can obtain the symmetric form of Eq. (2.13):

$$\begin{aligned}\frac{d}{dt}\mathbf{P}_{mech} = &\int_V \varepsilon_0[(\nabla\cdot\boldsymbol{\mathcal{E}})\boldsymbol{\mathcal{E}} + c_0^2(\nabla\cdot\boldsymbol{\mathcal{B}})\boldsymbol{\mathcal{B}} - \boldsymbol{\mathcal{E}}\times(\nabla\times\boldsymbol{\mathcal{E}}) - c_0^2\boldsymbol{\mathcal{B}}\times(\nabla\times\boldsymbol{\mathcal{B}})]\,dV \\ &- \int_V \varepsilon_0\frac{\partial}{\partial t}(\boldsymbol{\mathcal{E}}\times\boldsymbol{\mathcal{B}})\,dV,\end{aligned} \tag{2.14}$$

where $c_0 = 1/\sqrt{\varepsilon_0\mu_0}$ is the light speed in vacuum. The integrand of the second term on the right-handed side of Eq. (2.14) can be regarded as the time derivative of the linear momentum density of the field, which can be related to the Poynting vector: $\varepsilon_0(\boldsymbol{\mathcal{E}}\times\boldsymbol{\mathcal{B}}) = \boldsymbol{\mathcal{S}}/c_0^2$. Therefore, this integral term can be rewritten as

$$\int_V \varepsilon_0\frac{\partial}{\partial t}(\boldsymbol{\mathcal{E}}\times\boldsymbol{\mathcal{B}})\,dV = \frac{d}{dt}\int_V \frac{\boldsymbol{\mathcal{S}}}{c_0^2}\,dV = \frac{d}{dt}\mathbf{P}_{field}. \tag{2.15}$$

Furthermore, in the first integral term on the right-handed side of Eq. (2.14), the electric field and magnetic field terms are found as

$$\begin{aligned}(\nabla\cdot\boldsymbol{\mathcal{E}})\boldsymbol{\mathcal{E}} - \boldsymbol{\mathcal{E}}\times(\nabla\times\boldsymbol{\mathcal{E}}) &= (\nabla\cdot\boldsymbol{\mathcal{E}})\boldsymbol{\mathcal{E}} + (\boldsymbol{\mathcal{E}}\cdot\nabla)\boldsymbol{\mathcal{E}} - \frac{1}{2}\nabla(\boldsymbol{\mathcal{E}}\cdot\boldsymbol{\mathcal{E}}) \\ &= \nabla\cdot[\boldsymbol{\mathcal{E}}\otimes\boldsymbol{\mathcal{E}} - \frac{1}{2}(\boldsymbol{\mathcal{E}}\cdot\boldsymbol{\mathcal{E}})\mathbf{I}],\end{aligned} \tag{2.16}$$

$$\begin{aligned}(\nabla\cdot\boldsymbol{\mathcal{B}})\boldsymbol{\mathcal{B}} - \boldsymbol{\mathcal{B}}\times(\nabla\times\boldsymbol{\mathcal{B}}) &= (\nabla\cdot\boldsymbol{\mathcal{B}})\boldsymbol{\mathcal{B}} + (\boldsymbol{\mathcal{B}}\cdot\nabla)\boldsymbol{\mathcal{B}} - \frac{1}{2}\nabla(\boldsymbol{\mathcal{B}}\cdot\boldsymbol{\mathcal{B}}) \\ &= \nabla\cdot[\boldsymbol{\mathcal{B}}\otimes\boldsymbol{\mathcal{B}} - \frac{1}{2}(\boldsymbol{\mathcal{B}}\cdot\boldsymbol{\mathcal{B}})\mathbf{I}],\end{aligned} \tag{2.17}$$

where $\otimes$ denotes the operation of the dyadic product. $\mathbf{I}$ is the unit dyadic. We can therefore rewrite Eq. (2.14) into

$$\frac{d}{dt}(\mathbf{P}_{mech} + \mathbf{P}_{field}) = \int_V \nabla\cdot\mathbf{T}_M\,dV, \tag{2.18}$$

where

$$\mathbf{T}_M = \varepsilon_0[\boldsymbol{\mathcal{E}}\otimes\boldsymbol{\mathcal{E}} + c_0^2\boldsymbol{\mathcal{B}}\otimes\boldsymbol{\mathcal{B}} - \frac{1}{2}(\boldsymbol{\mathcal{E}}\cdot\boldsymbol{\mathcal{E}} + c_0^2\boldsymbol{\mathcal{B}}\cdot\boldsymbol{\mathcal{B}})\mathbf{I}] \tag{2.19}$$

is called Maxwell stress tensor. Eq. (2.18) explicitly describes the conservation of the total linear momentum. Similar to the energy flux density, $-\mathbf{T}_M$ can be regarded as the flux density of linear momentum.

By using Gauss' theorem, the volume integral of the divergence of $\mathbf{T}_M$ can be substituted with an integral of its flux over a closed surface. This gives

$$\frac{d}{dt}(\mathbf{P}_{mech} + \mathbf{P}_{field}) = \oint_S \mathbf{T}_M \cdot \mathbf{n} dS, \tag{2.20}$$

where $\mathbf{n}$ is the outward normal unit vector to the closed surface S. The right-hand side of Eq (2.20) corresponds to the flux of linear momentum that enters the surface S. Therefore, the time-averaged optical force on the particle can be obtained by

$$\mathbf{f} = \oint_S \overline{\mathbf{T}}_M \cdot \mathbf{n}\, dS, \tag{2.21}$$

where $\overline{\mathbf{T}}_M$ is the time-averaged Maxwell stress tensor. Besides, Eq (2.18) can also be written into a differential form, that is, the continuity equation for linear momentum,

$$\frac{\partial}{\partial t}(\frac{\boldsymbol{\mathcal{S}}}{c_0^2}) - \nabla \cdot \mathbf{T}_M = -(\rho\boldsymbol{\mathcal{E}} + \boldsymbol{j} \times \boldsymbol{\mathcal{B}}), \tag{2.22}$$

which describes the exchange of linear momentum between the field and sources.

■ Conservation of angular momentum

The conservation of angular momentum can be analyzed in the same way as we have processed energy and linear momentum. One can define an angular momentum with the cross product of the position vector $\mathbf{r}$ and linear momentum $\mathbf{P}$, thus the change rate of the mechanical angular momentum $\mathbf{J}_{mech}$ can be written as

$$\frac{d}{dt}\mathbf{J}_{mech} = \frac{d}{dt}(\mathbf{r} \times \mathbf{P}_{mech}) = \int_V \mathbf{r} \times (\rho\boldsymbol{\mathcal{E}} + \boldsymbol{j} \times \boldsymbol{\mathcal{B}})\, dV. \tag{2.23}$$

Therefore, the conservation law for angular momentum is given by

$$\frac{d}{dt}(\mathbf{J}_{mech} + \mathbf{J}_{field}) = \oint_S (\mathbf{r} \times \mathbf{T}_M) \cdot \mathbf{n}\, dS, \tag{2.24}$$

where

$$\mathbf{J}_{field} = \int_V \mathbf{r} \times \frac{\boldsymbol{\mathcal{S}}}{c_0^2}\, dV \tag{2.25}$$

is the angular momentum of the field. The right-hand side of Eq (2.24) represents the flux of angular momentum that enters the surface S. The differential continuity equation for angular momentum can also be written as

$$\frac{\partial}{\partial t}(\mathbf{r} \times \frac{\boldsymbol{\mathcal{S}}}{c_0^2}) - \nabla \cdot (\mathbf{r} \times \mathbf{T}_M) = -\mathbf{r} \times (\rho \boldsymbol{\mathcal{E}} + \boldsymbol{j} \times \boldsymbol{\mathcal{B}}), \tag{2.26}$$

depicting the exchange of angular momentum between the field and sources.

Finally, the same as the optical force obtained by Eq (2.21), we can also get the time-averaged optical torque on the charged particle:

$$\boldsymbol{\tau}_{total} = \oint_S (\mathbf{r} \times \overline{\mathbf{T}}_M) \cdot \mathbf{n} \, dS. \tag{2.27}$$

Eq. (2.27) and (2.21) are quite general equations because the continuity equations, i.e., Eq. (2.26) and Eq. (2.22), are exact consequences of Maxwell's equations. Additionally, the integral surface S is an arbitrary closed surface containing the particle, hence Eq. (2.27) and (2.21) can be applied to particles of any size, shape, and composition in the presence of arbitrarily structured optical fields, as long as Maxwell's equations are available.

In Eq (2.27), we use the subscript "total" because the conservation law Eq (2.24) and the continuity equation Eq (2.26) we discussed above are valid for the total angular momentum. It involves both the spin angular momentum and orbital angular momentum, which will be expounded in Subsection 2.2.2. Therefore, the optical torque obtained based on the Maxwell stress tensor, i.e., Eq (2.27), is the total optical torque, including the contributions from the transfers of spin angular momentum and orbital angular momentum. The separation of the contributions from the transfers of spin and orbital angular momenta to the total optical torque will be presented in Chapter 3.

2.2.2 Spin and orbital angular momentum

We obtained Eq (2.25) as the expression for the angular momentum of an electromagnetic field. In the following, we will introduce the separation of angular momentum into the spin and orbital parts. Considering a transverse electromagnetic field in a source-free space, it is convenient to replace the electric and magnetic fields by introducing two vector

potentials, $\boldsymbol{\mathcal{A}}$ and $\boldsymbol{C}$, defined as the following relations [3, 4]:

$$\boldsymbol{\mathcal{B}} = \nabla \times \boldsymbol{\mathcal{A}} = -\frac{1}{c_0^2}\frac{\partial \boldsymbol{C}}{\partial t}, \tag{2.28}$$

$$\boldsymbol{\mathcal{E}} = -\nabla \times \boldsymbol{C} = -\frac{\partial \boldsymbol{\mathcal{A}}}{\partial t}. \tag{2.29}$$

Thus, Eq (2.25) can be rewritten as

$$\mathbf{J}_{field} = \frac{\varepsilon_0}{2}\int_V \mathbf{r} \times [\boldsymbol{\mathcal{E}} \times (\nabla \times \boldsymbol{\mathcal{A}}) + \boldsymbol{\mathcal{B}} \times (\nabla \times \boldsymbol{C})]\, dV. \tag{2.30}$$

By employing the vector identity,

$$\mathbf{a} \times (\nabla \times \mathbf{b}) = \sum_{j=x,y,z} a_j(\nabla) b_j - (\mathbf{a} \cdot \nabla)\mathbf{b}, \tag{2.31}$$

Eq (2.30) becomes

$$\begin{aligned}\mathbf{J}_{field} =& \frac{\varepsilon_0}{2}\int_V \sum_{j=x,y,z} \mathcal{E}_j(\mathbf{r} \times \nabla)\mathcal{A}_j\, dV - \frac{\varepsilon_0}{2}\int_V \mathbf{r} \times (\boldsymbol{\mathcal{E}} \cdot \nabla)\boldsymbol{\mathcal{A}}\, dV \\ &+ \frac{\varepsilon_0}{2}\int_V \sum_{j=x,y,z} \mathcal{B}_j(\mathbf{r} \times \nabla)C_j\, dV - \frac{\varepsilon_0}{2}\int_V \mathbf{r} \times (\boldsymbol{\mathcal{B}} \cdot \nabla)\boldsymbol{C}\, dV.\end{aligned} \tag{2.32}$$

Since we only consider a transverse electromagnetic field in a source-free space, $\nabla \cdot \boldsymbol{\mathcal{E}} = 0$ and $\nabla \cdot \boldsymbol{\mathcal{B}} = 0$, we can use the following relations

$$-\mathbf{r} \times (\boldsymbol{\mathcal{E}} \cdot \nabla)\boldsymbol{\mathcal{A}} = \boldsymbol{\mathcal{E}} \times \boldsymbol{\mathcal{A}}, \tag{2.33}$$

$$-\mathbf{r} \times (\boldsymbol{\mathcal{B}} \cdot \nabla)\boldsymbol{C} = \boldsymbol{\mathcal{B}} \times \boldsymbol{C}. \tag{2.34}$$

Hence, we can separate the angular momentum into two parts as

$$\mathbf{L} = \frac{\varepsilon_0}{2}\int_V (\sum_{j=x,y,z} \mathcal{E}_j(\mathbf{r} \times \nabla)\mathcal{A}_j + \sum_{j=x,y,z} \mathcal{B}_j(\mathbf{r} \times \nabla)C_j)\, dV, \tag{2.35}$$

$$\boldsymbol{\Sigma} = \frac{\varepsilon_0}{2}\int_V (\boldsymbol{\mathcal{E}} \times \boldsymbol{\mathcal{A}} + \boldsymbol{\mathcal{B}} \times \boldsymbol{C})\, dV. \tag{2.36}$$

We can see $\mathbf{L}$ is related to the position vector $\mathbf{r}$, corresponding to the orbital angular momentum. However, $\boldsymbol{\Sigma}$ depends on the vectorial nature of the field (polarization), therefore

it can be associated with the spin angular momentum.

Considering a monochromatic transverse electromagnetic field, $\boldsymbol{\mathcal{E}}(\mathbf{r},t) = \mathrm{Re}[\mathbf{E}(\mathbf{r})e^{-i\omega t}]$ and $\boldsymbol{\mathcal{B}}(\mathbf{r},t) = \mathrm{Re}[\mathbf{B}(\mathbf{r})e^{-i\omega t}]$, we have the relation between the vector potentials and electromagnetic fields as $\mathbf{E} = i\omega\mathbf{A}$, $\mathbf{B} = i\omega\mathbf{C}/c_0^2$, where ω is the angular frequency of the field. $\mathbf{A}$ and $\mathbf{C}$ are given by $\boldsymbol{\mathcal{A}}(\mathbf{r},t) = \mathrm{Re}[\mathbf{A}(\mathbf{r})e^{-i\omega t}]$ and $\boldsymbol{C}(\mathbf{r},t) = \mathrm{Re}[\mathbf{C}(\mathbf{r})e^{-i\omega t}]$, respectively. Accordingly, we can obtain the averaged spin ($\boldsymbol{\sigma}$) and orbital ($\boldsymbol{l}$) angular momentum densities in a form that is useful in many practical cases:

$$\boldsymbol{l} = \frac{1}{4\omega}\left\{\varepsilon_0 \sum_{j=x,y,z} \mathrm{Im}[\mathrm{E}_j^*(\mathbf{r}\times\nabla)\mathrm{E}_j] + \frac{1}{\mu_0}\sum_{j=x,y,z}\mathrm{Im}[\mathrm{B}_j^*(\mathbf{r}\times\nabla)\mathrm{B}_j]\right\}, \tag{2.37}$$

$$\boldsymbol{\sigma} = \frac{1}{4\omega}\{\varepsilon_0\mathrm{Im}[\mathbf{E}^*\times\mathbf{E}] + \frac{1}{\mu_0}\mathrm{Im}[\mathbf{B}^*\times\mathbf{B}]\}. \tag{2.38}$$

2.3 Localized surface plasmon

Surface plasmons are the collective oscillations of electron plasma at the interface between two materials with different signs of the real part of permittivity (e.g. the interface between a metal and a dielectric). The excitation of surface plasmon at a metal-dielectric interface, including both the charge motion and its produced electromagnetic field, can be divided into two categories: surface plasmon polariton (SPP) and localized surface plasmon (LSP) [5–8].

SPPs are electromagnetic excitations that propagate along an interface between metal and dielectric as shown in Figure 2.1(a), which are induced by the coupling of the electromagnetic fields and the oscillations of free electrons on a metal surface [9, 10]. For the excitation of SPP, the SPP resonance condition can not satisified by the electromagnetic field in the air because the dispersion curves of air and SPP do not intersect at any value of propagation constant except for the origin as shown in Figure 2.1(b). However, we can find an intersection between the dispersion curves of SPP and a proper dielectric medium. In this aspect, dielectric prisms are usually used to excite an SPP on a metal surface. And, another method to generate SPP is by using a grating structure to realize the phase matching. Interested readers are referred to Refs [6–8].

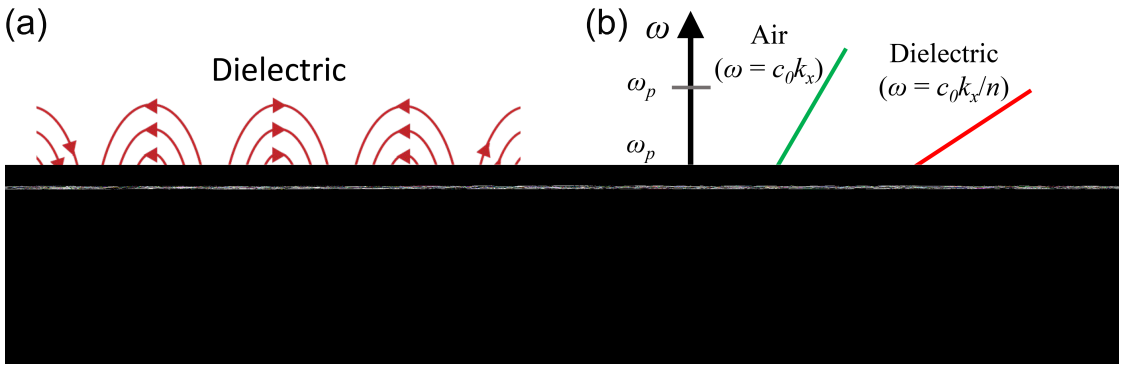

Figure 2.1: (a) Schematic illustration of SPPs. (b) Dispersion curve for air, dielectric medium, and SPP with an air-metal interface: ω is the angular frequency of light or SPP. c_0 is the speed of light in vacuum. k_x is the propagation constant of SPP. n is the refractive index of the dielectric medium.

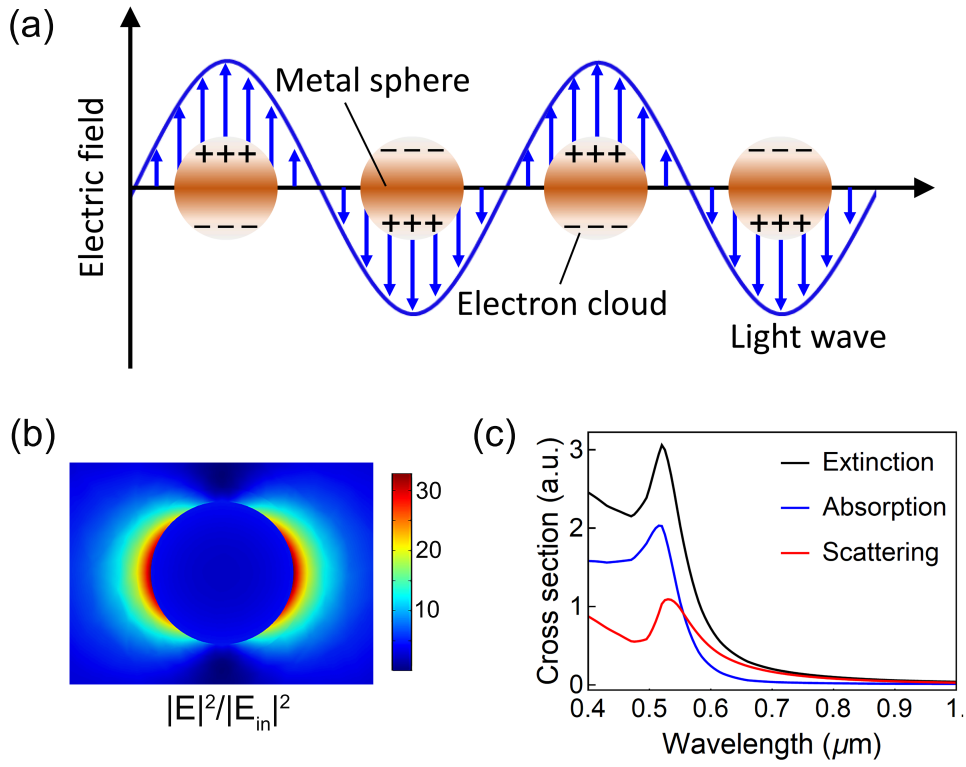

Figure 2.2: (a) Schematic illustration of LSPs. (b) Field enhancement distribution near the surface of a nanosphere with a diameter of 100 nm. (c) Extinction, absorption, and scattering cross sections of a nanosphere with a diameter of 100 nm.

On the other hand, LSPs are non-propagating excitation of the free electron at the closed surface of a nanometer-sized structure. In response to an external electromagnetic field, a collective oscillation of free electrons can be induced in the metal nanoparticle as shown in Figure 2.2. In this case, a restoring force on the oscillating electrons can be produced due to the curved surface of the nanoparticle, resulting in a resonance of the plasmon mode, which is called localized surface plasmon resonance (LSPR). Importantly, this resonance can be directly excited by the illumination of an external electromagnetic field. The excitation of LSPR gives rise to an intense field near the nanoparticle surface and enhances the optical cross section in absorption and scattering as shown in Figures 2.2(b) and 2.2(c) [11–13], which highly depends on the shape, size, and surrounding environment. These properties of LSPs lead to their various applications in the enhancement and manipulation of light-matter interaction in physics, chemistry, and biology [14–22].

In our study, the strong interaction between light and plasmonic nanostructures induced by the excitation of LSPs is employed to investigate the three important phenomena of the interaction of angular momentum between light and matter. Therefore, in this section, we will introduce the basic physics of LSPs.

2.3.1 Optical response of a metal nanosphere

It should be pointed out that the quasi-static approximation can be applied when a particle of size much smaller than the wavelength of light interacts with an electromagnetic field. In this case, it can be approximated as a particle in an electrostatic field because the phase of the time-harmonic oscillating electromagnetic field can be regarded as a constant over the particle. With this approximation, we can be obtained the spatial field distribution from the solution of the Laplace equation for the potential, $\nabla^2\Phi = 0$ [1]. Then, the time dependence can be directly added to the solution to describe the interaction of the particle with the time-varying field (without considering the spatial retardation effects).

Here, as shown in Figure 2.3, we consider a homogeneous isotropic metal nanosphere with a radius of a placed in a uniform electrostatic field $\mathbf{E} = \mathrm{E}_0\hat{\mathbf{z}}$. The dielectric permittivity of the metal nanosphere is denoted by a complex number depending on the angular frequency, $\varepsilon(\omega)$. The nanosphere is surrounded by an isotropic lossless medium with a dielectric constant of ε_m.

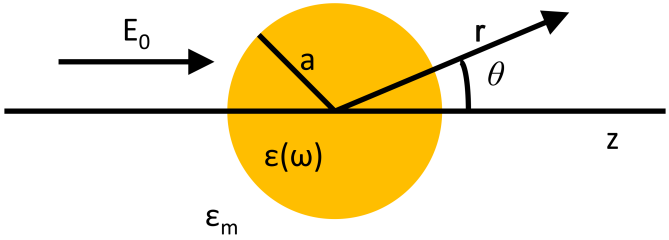

Figure 2.3: Schematic illustration of a metal nanosphere in an electrostatic field.

From the solution of the Laplace equation in a spherical coordinate and considering azimuthal symmetry in our system, we have the general solution of the potentials for the field distribution: [1]

$$\Phi(r,\theta) = \sum_{l=0}^{\infty}[A_l r^l + B_l r^{-(l+1)}]P_l(\cos\theta), \tag{2.39}$$

where θ is the angle between the position vector $\mathbf{r}$ and the z-axis. $P_l(\cos\theta)$ is the Legendre polynomials of order l. The coefficients A_l and B_l can be determined from the boundary conditions. Considering that the potential should not be divergent at the origin, we can define the potential inside the nanosphere as

$$\Phi_{in}(r,\theta) = \sum_{l=0}^{\infty} A_l r^l P_l(\cos\theta), \tag{2.40}$$

and the potential outside the nanosphere as

$$\Phi_{out}(r,\theta) = \sum_{l=0}^{\infty}[B_l r^l + C_l r^{-(l+1)}]P_l(\cos\theta). \tag{2.41}$$

Now, let's consider the boundary conditions. When $\mathbf{r} \to \infty$, $\Phi_{out} = \mathrm{E}_0\cos\theta$ should be satisfied, so that we can get $B_1 = -\mathrm{E}_0$ and $B_l = 0$ $(l \neq 1)$. Besides, at the boundary $r = a$, we have the boundary conditions for the tangential and normal components of electric and displacement fields as following

$$-\frac{1}{a}\frac{\partial\Phi_{in}}{\partial\theta}\bigg|_{r=a} = -\frac{1}{a}\frac{\partial\Phi_{out}}{\partial\theta}\bigg|_{r=a}, \tag{2.42}$$

$$-\varepsilon\frac{\partial\Phi_{in}}{\partial r}\bigg|_{r=a} = -\varepsilon_m\frac{\partial\Phi_{out}}{\partial r}\bigg|_{r=a}, \tag{2.43}$$

respectively. Therefore, by solving these two equations, we can obtained the final solution for the potentials as

$$\Phi_{in} = -\frac{3\varepsilon_m}{\varepsilon + 2\varepsilon_m}\mathrm{E}_0 r\cos\theta, \tag{2.44}$$

$$\Phi_{out} = -\mathrm{E}_0 r\cos\theta + \frac{\varepsilon - \varepsilon_m}{\varepsilon + 2\varepsilon_m}\mathrm{E}_0 a^3\frac{\cos\theta}{r^2}. \tag{2.45}$$

To understand Eq. (2.45), we now introduce a dipole moment $\mathbf{p}$ and Eq (2.45) can be rewrite as

$$\Phi_{out} = -\mathrm{E}_0 r\cos\theta + \frac{\mathbf{p}\cdot\mathbf{r}}{4\pi\varepsilon_m r^3}, \tag{2.46}$$

$$\mathbf{p} = 4\pi\varepsilon_m a^3\frac{\varepsilon - \varepsilon_m}{\varepsilon + 2\varepsilon_m}\mathbf{E}. \tag{2.47}$$

We can see the first term on the right-hand side of Eq (2.46) is related to the applied field. However, it is worth noting that the second term is associated with the dipole moment inside the nanosphere induced by the applied field, which is proportional to the magnitude of $\mathbf{E}$. Therefore, we can define the polarizability of the nanosphere as

$$\alpha = 4\pi\varepsilon_m a^3\frac{\varepsilon - \varepsilon_m}{\varepsilon + 2\varepsilon_m}. \tag{2.48}$$

Obviously, we can find a resonant enhancement when the relation

$$\mathrm{Re}[\varepsilon] = 2\varepsilon_m, \tag{2.49}$$

is satisfied. Eq. (2.49) is called the Frohlich condition. What is more, the resonance is known as LSPR in an oscillating field.

We have described the optical response of a metal nanosphere in an electrostatic field. As we mentioned above, this description as an induced dipole moment is also valid in the quasi-static regime. Considering a time-harmonic electric field, $\mathbf{E}(\mathbf{r}, t) = \mathbf{E}_0 e^{-i\omega t}$, the induced oscillating dipole moment can still be written as $\mathbf{p} = \alpha\mathbf{E}_0 e^{-i\omega t}$ with the α defined as Eq. (2.48).

2.3.2 Oscillating electric dipole

We have seen that the interaction of a metal nanosphere with an oscillating electromagnetic field can be described by the induced oscillating dipole. Next, we will continue to discuss the properties of the oscillating dipole.

■ Electric dipole radiation

We consider an electric dipole induced by a time-harmonic electromagnetic field $\mathbf{E}_\mathrm{i}(t) = \mathbf{E}_\mathrm{i}e^{-i\omega t}$ in vacuum, which has the same time dependence as $\mathbf{p}_\mathrm{d}(t) = \mathbf{p}_\mathrm{d}e^{-i\omega t}$, where ω is the angular frequency. Here, $\mathbf{p}_\mathrm{d}$ is given by

$$\mathbf{p}_\mathrm{d} = \alpha(\omega)\mathbf{E}_\mathrm{i}e^{-i\omega t}, \tag{2.50}$$

where α is the complex electric polarizability depending on the angular frequency.

Consequently, the oscillating electric dipole can produce a radiation field. Here, we consider that a dipole is along the polar axis s at the origin of a spherical coordinate, which can be expressed as

$$\mathbf{p}_\mathrm{d} = p_\mathrm{d}\hat{\mathbf{s}}. \tag{2.51}$$

Therefore, the radiation field can be written as

$$\mathbf{E}_\mathrm{d} = \frac{p_\mathrm{d}k_0^3}{4\pi\varepsilon_0}\frac{e^{ik_0r}}{k_0r}\left\{2\cos\theta\left[\frac{1}{(k_0r)^2} - \frac{i}{k_0r}\right]\hat{\mathbf{r}} + \sin\theta\left[\frac{1}{(k_0r)^2} - \frac{i}{k_0r} - 1\right]\hat{\boldsymbol{\theta}}\right\}, \tag{2.52}$$

where k_0 is the wavenumber in vacuum, $\hat{\mathbf{r}}$ is the radial unit vector, r is the radial distance, $\hat{\boldsymbol{\theta}}$ is the polar unit vector, θ is the polar angle, and ϕ is the azimuthal angle. In the far field ($k_0r \gg 1$), the radiation field becomes an outwards propagating spherical wave, which can be expressed as

$$\mathbf{E}_{\mathrm{d},far} = -\frac{p_\mathrm{d}k_0^3}{4\pi\varepsilon_0}\frac{e^{ik_0r}}{k_0r}\sin\theta\hat{\boldsymbol{\theta}}. \tag{2.53}$$

■ Cross sections

We now consider the cross sections of an electric dipole $\mathbf{p}_\mathrm{d}$ induced by an incident electromagnetic field $\mathbf{E}_\mathrm{i}$ in vacuum. The absorption cross section σ_{abs} is defined as the ratio

of the absorption rate of energy to the power density of the incident field. The scattering cross section σ_{sca} multiplied by the power density of the incident field is equivalent to the rate of the energy removed via the scattering field in all directions. The sum of the scattering cross section and absorption cross section is referred to as the extinction cross section $\sigma_{ext} = \sigma_{abs} + \sigma_{sca}$.

We first consider the extinction cross section of the electric dipole. The intensity of the incident electromagnetic field is given by

$$I_{\mathrm{i}} = \frac{1}{2} c_0 \varepsilon_0 |\mathrm{E_i}|^2. \tag{2.54}$$

The total power removed by the dipole is equal to the rate of the work done on the dipole by the incident field, which can be expressed as

$$P_{ext} = \frac{1}{2} \int_V \mathrm{Re}[\boldsymbol{j}_{\mathrm{d}} \cdot \mathbf{E}_{\mathrm{i}}^*] \, dV, \tag{2.55}$$

where $\boldsymbol{j}_{\mathrm{d}}$ is the current density induced by the oscillating electric dipole. Here, $\boldsymbol{j}_{\mathrm{d}}$ can be written as

$$\boldsymbol{j}_{\mathrm{d}} = -i\omega \mathbf{p}_{\mathrm{d}} \delta(\mathbf{r} - \mathbf{r}_{\mathrm{d}}), \tag{2.56}$$

where $\mathbf{r}_{\mathrm{d}}$ is the position vector of the dipole. Therefore, Eq. (2.55) becomes

$$P_{ext} = \frac{\omega}{2} \mathrm{Im}[\mathbf{p}_{\mathrm{d}} \cdot \mathbf{E}_{\mathrm{i}}^*]. \tag{2.57}$$

Hence, the extinction cross section can be expressed as

$$\sigma_{ext} = \frac{P_{ext}}{I_{\mathrm{i}}} = \frac{k_0}{\varepsilon_0} \mathrm{Im}[\alpha]. \tag{2.58}$$

Then, in order to calculate the work done on the dipole by the scattered field at the location of the dipole for the scattering cross section, only the scattered field parallel to the dipole need to be considered, which is given by

$$\mathbf{E}_{\mathrm{d}} \cdot \hat{\mathbf{s}} = \frac{p_{\mathrm{d}} k_0^3}{4\pi\varepsilon_0} \frac{e^{ik_0 r}}{k_0 r} \left\{ 2\cos^2\theta \left[\frac{1}{(k_0 r)^2} - \frac{i}{k_0 r} \right] + \sin^2\theta \left[\frac{1}{(k_0 r)^2} - \frac{i}{k_0 r} - 1 \right] \right\}. \tag{2.59}$$

At the location of the dipole ($k_0 r \ll 1$), we can use the Taylor series expansion, i.e., $e^{ik_0 r} \approx 1 + ik_0 r - \frac{1}{2}(k_0 r)^2 - \frac{i}{6}(k_0 r)^3$, and rewrite Eq. (2.59) into

$$\mathbf{E}_\mathrm{d} \cdot \hat{\mathbf{s}} = \frac{p_\mathrm{d} k_0^3}{4\pi\varepsilon_0} \frac{1}{(k_0 r)^3} \left[(3\cos^2\theta - 1) + \frac{1}{2}(\cos^2\theta + 1)(k_0 r)^2 + \frac{2i}{3}(k_0 r)^3 \right]. \tag{2.60}$$

Therefore, the work done on the dipole by the scattered field can be expressed as

$$P_{sca} = -\frac{\omega}{2}\mathrm{Im}[\mathbf{p}_\mathrm{d} \cdot \mathbf{E}_\mathrm{d}^*(\mathbf{r}_\mathrm{d})] = \frac{\omega k_0^3 |p_\mathrm{d}|^2}{12\pi\varepsilon_0}. \tag{2.61}$$

Hence, the scattering cross section can be written as

$$\sigma_{sca} = \frac{P_{sca}}{I_\mathrm{i}} = \frac{k_0^4}{6\pi\varepsilon_0^2}|\alpha|^2. \tag{2.62}$$

Finally, we can also obtain the absorption cross section by

$$\sigma_{abs} = \sigma_{ext} - \sigma_{sca} = \frac{k_0}{\varepsilon_0}\mathrm{Im}[\alpha] - \frac{k_0^4}{6\pi\varepsilon_0^2}|\alpha|^2. \tag{2.63}$$

References

[1] J. D. Jackson, *Classical Electrodynamics*. New York: John Wiley & Sons, 1999.

[2] P. H. Jones, O. M. Maragò, and G. Volpe, *Optical tweezers: Principles and applications*. Cambridge, England: Cambridge University Press, 2015.

[3] G. Nienhuis, "Conservation laws and symmetry transformations of the electromagnetic field with sources," *Phys. Rev. A*, vol. 93, no. 2, p. 023840, 2016.

[4] J. B. Götte and S. M. Barnett, *Light beams carrying orbital angular momentum*, p. 1–30. Cambridge University Press, 2012.

[5] H. Raether, "Surface plasmons on smooth and rough surfaces and on gratings," *Springer Tracts Mod. Phys.*, vol. 111, p. 1, 1988.

[6] S. A. Maier, *Plasmonics: fundamentals and applications*. New York: Springer Science & Business Media, 2007.

[7] M. Dragoman and D. Dragoman, "Plasmonics: Applications to nanoscale terahertz and optical devices," *Prog. Quantum Electron.*, vol. 32, no. 1, pp. 1–41, 2008.

[8] A. V. Zayats and I. I. Smolyaninov, "Near-field photonics: surface plasmon polaritons and localized surface plasmons," *J. Opt. A: Pure Appl. Opt.*, vol. 5, no. 4, p. S16, 2003.

[9] M. L. Juan, M. Righini, and R. Quidant, "Plasmon nano-optical tweezers," *Nat. Photonics*, vol. 5, no. 6, p. 349, 2011.

[10] W. L. Barnes, A. Dereux, and T. W. Ebbesen, "Surface plasmon subwavelength optics," *Nature*, vol. 424, no. 6950, pp. 824–830, 2003.

[11] V. Giannini, A. I. Fernández-Domínguez, S. C. Heck, and S. A. Maier, "Plasmonic nanoantennas: fundamentals and their use in controlling the radiative properties of nanoemitters," *Chem. Rev.*, vol. 111, no. 6, pp. 3888–3912, 2011.

[12] K. E. Fong and L.-Y. L. Yung, "Localized surface plasmon resonance: a unique property of plasmonic nanoparticles for nucleic acid detection," *Nanoscale*, vol. 5, no. 24, pp. 12043–12071, 2013.

[13] K. L. Kelly, E. Coronado, L. L. Zhao, and G. C. Schatz, "The optical properties of metal nanoparticles: The influence of size, shape, and dielectric environment," *J. Phys. Chem. B*, vol. 107, no. 3, pp. 668–677, 2003.

[14] Y. Choi, T. Kang, and L. P. Lee, "Plasmon resonance energy transfer (pret)-based molecular imaging of cytochrome c in living cells," *Nano Lett.*, vol. 9, no. 1, pp. 85–90, 2009.

[15] Y. Y. Tanaka and T. Shimura, "Tridirectional polarization routing of light by a single triangular plasmonic nanoparticle," *Nano Lett.*, vol. 17, no. 5, pp. 3165–3170, 2017.

[16] G. Baffou, R. Quidant, and F. J. García de Abajo, "Nanoscale control of optical heating in complex plasmonic systems," *ACS Nano*, vol. 4, no. 2, pp. 709–716, 2010.

[17] L. Michaeli, S. Keren-Zur, O. Avayu, H. Suchowski, and T. Ellenbogen, "Nonlinear surface lattice resonance in plasmonic nanoparticle arrays," *Phys. Rev. Lett.*, vol. 118, no. 24, p. 243904, 2017.

[18] B. Metzger, M. Hentschel, and H. Giessen, "Probing the near-field of second-harmonic light around plasmonic nanoantennas," *Nano Lett.*, vol. 17, no. 3, pp. 1931–1937, 2017.

[19] T. H. Le and T. Tanaka, "Plasmonics–nanofluidics hydrid metamaterial: an ultrasensitive platform for infrared absorption spectroscopy and quantitative measurement of molecules," *ACS Nano*, vol. 11, no. 10, pp. 9780–9788, 2017.

[20] E. Mohammadi, K. Tsakmakidis, A. Askarpour, P. Dehkhoda, A. Tavakoli, and H. Altug, "Nanophotonic platforms for enhanced chiral sensing," *ACS Photonics*, vol. 5, no. 7, pp. 2669–2675, 2018.

[21] Y. Tanaka, S. Kaneda, and K. Sasaki, "Nanostructured potential of optical trapping using a plasmonic nanoblock pair," *Nano Lett.*, vol. 13, no. 5, pp. 2146–2150, 2013.

[22] P. Anger, P. Bharadwaj, and L. Novotny, "Enhancement and quenching of single-molecule fluorescence," *Phys. Rev. Lett.*, vol. 96, no. 11, p. 113002, 2006.

Chapter 3

Quantification of the optical spin-orbit transformation in light-matter interaction

3.1 Introduction

When light carrying angular momentum interacts with matter, an exchange can occur between the spin and orbital parts of the angular momentum. In recent years, this spin-orbit interaction of light has been attracting rapidly growing interest due to its promising potential in nano-optics, photonics, and plasmonics [1–5]. Therefore, it is of great significance to find a method that can quantify the transformation between spin angular momentum (SAM) and orbital angular momentum (OAM) in the light-matter interaction. The transfer of angular momentum between light and matter enables an optical torque that acts on the matter [6–8]. Optical torque has gained considerable attention owing to the crucial role it plays in optical manipulation, especially leading to a variety of applications in nanoelectromechanical systems [9, 10], biological science [11, 12], and chemistry [13]. In the analysis of the transfer of angular momenta between light and matter, as we discussed in Chapter 2, the Maxwell stress tensor (MST) method has been extensively used to calculate the optical torque on the matter, which can be derived from the continuity equation for angular momentum. Optical torque arises both from the transfers of the SAM and OAM of light [6–8]. Therefore, the study of the respective contributions of SAM and

OAM to the optical torque, that is, the separate characterization of the SAM transfer and OAM transfer will greatly facilitate the quantification of the optical spin-orbit transformation. However, the MST method cannot separate them because it is restricted to the optical toque resulting from the total angular momentum.

In this chapter, we propose an approach to quantifing the optical spin-orbit transformation in the interaction between light and matter by separately characterizing the transfer of SAM from that of OAM. We start by introducing another important quantity of electromagnetic field, i.e., optical chirality density. In analogy with the MST method, we then obtain the continuity equation for SAM from the flux of optical chirality density, which provides a method to separate the contributions of the SAM and OAM to the total optical torque. Finally, we apply this method to some examples with the electromagnetic fields calculated by the finite element method to verify the correctness of our equation and show an application of the analysis of spin-orbit transformation in light-matter interaction by combining with the MST method.

3.2 Optical chirality density

In 1964, Lipkin gave evidence of ten new independent conservation laws to characterize the physical states of an electromagnetic field in vacuum [14]. Initially, only mathematical aspects of these new extensive quantities were analyzed, lacking specific physical interpretation assigned to these quantities. Seeing electromagnetic field properties can be described by many conserved quantities, such as energy, linear momentum, and angular momentum, it is widely believed that every conserved quantity is physically significant. Therefore, researchers have put a lot of effort into searching for the physical meaning of these quantities [15–19].

Several years ago, the research on the interaction between chiral molecules and electromagnetic field has restarted a considerable interest in Lipkin's zilches. In order to enhance the optical enantioselectivity of an electromagnetic field, Tang and Cohen proposed and demonstrated the use of "superchiral" electromagnetic fields that yield ultra-dichroic interactions with chiral molecules [19, 20]. They introduced the 00-zilch as a measure of the local density of the chirality of the electromagnetic field. They named it as optical

chirality density. Recently, this quantity has been widely studied and employed in the chirality characterization of molecules and electromagnetic fields [21–25]. The optical chirality density in a medium with electric permittivity ε and magnetic permeability μ can be expressed as [26]

$$C = \frac{\varepsilon}{2}\boldsymbol{\mathcal{E}} \cdot \nabla \times \boldsymbol{\mathcal{E}} + \frac{1}{2\mu}\boldsymbol{\mathcal{B}} \cdot \nabla \times \boldsymbol{\mathcal{B}}, \tag{3.1}$$

where $\boldsymbol{\mathcal{E}}$ and $\boldsymbol{\mathcal{B}}$ are the time-dependent electric field and magnetic induction, respectively. While many studies on optical chirality have been published, it is definitely surprising that its physical aspects or relation to well-known quantities have not been well described. Even though the continuity equation was proposed and discussed by many researchers, it is still unable to be clearly depicted with the consideration of source terms (charges and currents).

We will now reveal the relation between the SAM and optical chirality of an electromagnetic field in a general source-added space, which is an important relation to find the continuity equation for SAM. In an electromagnetic field, the conserved quantities should satisfy their continuity equations, indicating their exchange between the field and sources. As introduced in Chapter 2 (Section 2.2), Poynting's theorem is the most elementary continuity equation, which explicates the energy transfer between field and sources. In the following, we restrict our discussion to a homogeneous, isotropic, lossless medium. In relation to an electromagnetic field, we regard a particle as a distribution of charges with density $\rho(\mathbf{r}, t)$ and currents with density $\boldsymbol{j}(\mathbf{r}, t)$. The continuity equation for optical chirality is given in analogy with the Poynting's theorem. By taking the time derivative of Eq. (3.1) and using Maxwell's equations, we get [19, 26]

$$\frac{\partial C}{\partial t} + \nabla \cdot \boldsymbol{\mathcal{F}} = -\frac{1}{2}[\boldsymbol{j} \cdot (\nabla \times \boldsymbol{\mathcal{E}}) + \boldsymbol{\mathcal{E}} \cdot (\nabla \times \boldsymbol{j})], \tag{3.2}$$

where

$$\boldsymbol{\mathcal{F}} = \frac{1}{2\mu}[\boldsymbol{\mathcal{E}} \times (\nabla \times \boldsymbol{\mathcal{B}}) - \boldsymbol{\mathcal{B}} \times (\nabla \times \boldsymbol{\mathcal{E}})] \tag{3.3}$$

is the chirality flux density. Eq. (3.2) and Eq. (3.3) have been widely used for characterizing the optical chirality density. Considering a monochromatic field in a source-free

space ($\boldsymbol{j} = 0$), $\boldsymbol{\mathcal{E}}(\mathbf{r},t) = \mathrm{Re}[\mathbf{E}(\mathbf{r})e^{-i\omega t}]$ and $\boldsymbol{\mathcal{B}}(\mathbf{r},t) = \mathrm{Re}[\mathbf{B}(\mathbf{r})e^{-i\omega t}]$, some studies have shown that $\boldsymbol{\mathcal{F}}$ is proportional to the SAM density of light, one of the well-known important physical quantities, which is defined as Eq. (2.38).

By using Maxwell's equations, $\boldsymbol{\mathcal{F}}$ can be written as

$$\boldsymbol{\mathcal{F}} = \boldsymbol{\mathcal{R}} + \frac{1}{2}\boldsymbol{\mathcal{E}} \times \boldsymbol{j}, \tag{3.4}$$

$$\boldsymbol{\mathcal{R}} = \frac{1}{2}(\varepsilon\boldsymbol{\mathcal{E}} \times \frac{\partial \boldsymbol{\mathcal{E}}}{\partial t} + \frac{1}{\mu}\boldsymbol{\mathcal{B}} \times \frac{\partial \boldsymbol{\mathcal{B}}}{\partial t}). \tag{3.5}$$

$\boldsymbol{\mathcal{R}}$, the first term on the right-hand side in Eq. (3.4), can be expressed as

$$\boldsymbol{\mathcal{R}} = \frac{\omega}{4}\{\varepsilon \mathrm{Im}[\mathbf{E}^* \times \mathbf{E}] + \frac{1}{\mu}\mathrm{Im}[\mathbf{B}^* \times \mathbf{B}]\} \tag{3.6}$$

in a monochromatic field, which is proportional to the definition of SAM density, i.e., Eq. (2.38). The second term on the right-hand side in Eq. (3.4) is related to the sources. We note that the current density $\boldsymbol{j}$ can be considered as $\partial \boldsymbol{\mathcal{P}}_c/\partial t$, where $\boldsymbol{\mathcal{P}}_c$ is the polarization that induces the current. The term $(\boldsymbol{\mathcal{E}} \times \boldsymbol{j})/2$ can be written as $(\boldsymbol{\mathcal{E}} \times \partial \boldsymbol{\mathcal{P}}_c/\partial t)/2$, which shows the same intrinsic physics as that of Eq. (3.5). Therefore, in a monochromatic field, the quantity

$$\frac{\boldsymbol{\mathcal{F}}}{\omega^2} = \frac{1}{2\omega^2}(\varepsilon\boldsymbol{\mathcal{E}} \times \frac{\partial \boldsymbol{\mathcal{E}}}{\partial t} + \frac{1}{\mu}\boldsymbol{\mathcal{B}} \times \frac{\partial \boldsymbol{\mathcal{B}}}{\partial t} + \boldsymbol{\mathcal{E}} \times \boldsymbol{j}) \tag{3.7}$$

can be regarded as the SAM density of the total field, including the contribution from the first two terms by the light field and the last term by the current.

3.3 Optical chirality and optical helicity

We have seen that the optical chirality density is typically associated with the SAM density. At the same time, it is known that optical helicity is also a conserved quantity in electromagnetic theory that describes the angular momentum associated with circular polarization. In this section, we will show the relation between the optical chirality and optical helicity.

Optical helicity density has its natural expression in terms of magnetic and electric

vector potentials. Therefore, we now introduce the uniquely defined potentials by the relations

$$\boldsymbol{\mathcal{B}} = \nabla \times \boldsymbol{\mathcal{A}}, \tag{3.8}$$

$$\boldsymbol{\mathcal{E}} = -\nabla \times \boldsymbol{\mathcal{C}}, \tag{3.9}$$

under the condition that the vector potentials are purely transverse, so that $\nabla \cdot \boldsymbol{\mathcal{A}} = 0$ and $\nabla \cdot \boldsymbol{\mathcal{C}} = 0$. The optical helicity density of electromagnetic field is defined by [16]

$$H = \frac{\varepsilon}{2c}(c^2 \boldsymbol{\mathcal{A}} \cdot \boldsymbol{\mathcal{B}} - \boldsymbol{\mathcal{C}} \cdot \boldsymbol{\mathcal{E}}), \tag{3.10}$$

where c is the light speed in the medium.

We now consider a monochromatic field in a source-free space, $\boldsymbol{\mathcal{E}}(\mathbf{r},t) = \mathrm{Re}[\mathbf{E}(\mathbf{r})e^{-i\omega t}]$, $\boldsymbol{\mathcal{B}}(\mathbf{r},t) = \mathrm{Re}[\mathbf{B}(\mathbf{r})e^{-i\omega t}]$, and $\boldsymbol{j} = 0$, we have the relation between the vector potentials and electromagnetic fields as $\mathbf{E} = i\omega\mathbf{A}$, $\mathbf{B} = i\omega\mathbf{C}/c^2$, where $\mathbf{A}$ and $\mathbf{C}$ are given by $\boldsymbol{\mathcal{A}}(\mathbf{r},t) = \mathrm{Re}[\mathbf{A}(\mathbf{r})e^{-i\omega t}]$ and $\boldsymbol{\mathcal{C}}(\mathbf{r},t) = \mathrm{Re}[\mathbf{C}(\mathbf{r})e^{-i\omega t}]$, respectively. For the optical helicity density, Eq. (3.10), this gives the result

$$H_{mon} = \frac{c\varepsilon}{2\omega}\mathrm{Im}[\mathbf{E} \cdot \mathbf{B}^*]. \tag{3.11}$$

Meanwhile, for the optical chirality density, Eq. (3.1) can be rewritten as

$$C_{mon} = \frac{\varepsilon\omega}{2}\mathrm{Im}[\mathbf{E} \cdot \mathbf{B}^*]. \tag{3.12}$$

Thus, the relation between the optical chirality density and optical helicity density is greatly simplified in the case of monochromatic fields in a source-free space: $H_{mon} = cC_{mon}/\omega^2$. Note that the optical helicity is a conserved quantity, it should obey its continuity equation just like the optical chirality does. Due to the proportional relation between the optical chirality density and optical helicity density, it is obvious that the chirality flux density and helicity flux density follows the same proportional relation with factor c/ω^2. Moreover, the expression for the chirality flux density in the special case of monochromatic fields in a source-free region is proportional to the SAM density of light. Therefore,

in this case, both the chirality flux density and helicity flux density are proportional to the SAM density of light, which is related to the local degree of circular polarization.

3.4 Continuity equation for spin angular momentum

In the preceding sections, we have revealed the relation between the SAM density of the field and the chirality flux density. We now turn our attention to the angular momentum transfer in light-matter interaction. The angular momentum transfer can induce an optical torque acting on the matter. It is worth mentioning that light possesses both SAM and OAM. Both can interact with matter to produce optical torques acting on the matter. Consequently, the optical torque calculated by the MST method, i.e., Eq. (2.27), includes both the contribution from the SAM transfer and OAM transfer. In other words, the MST method has not been able to characterize the SAM transfer and OAM transfer separately thus far.

As we discussed in Eq. (3.7), $\mathcal{F}/\omega^2$ is the SAM density of the field, which is related to the chirality flux density. This relation is similar to that the linear momentum density of the field can be denoted by the energy flux density, $\boldsymbol{S}/c^2$, which has been discussed in Chapter 2 (Section 2.2). Accordingly, in analogy with the continuity equation for linear momentum, by taking the time derivative of $\mathcal{F}/\omega^2$ and applying Maxwell's equations, we obtain the exact continuity equation for SAM:

$$\frac{\partial}{\partial t}\left(\frac{\mathcal{F}}{\omega^2}\right) - \nabla \cdot \mathbf{T}_S = -\frac{c^2}{2\omega^2}[\rho(\nabla \times \boldsymbol{\mathcal{E}}) + \boldsymbol{j} \times (\nabla \times \boldsymbol{\mathcal{B}}) + (\nabla \times \boldsymbol{j}) \times \boldsymbol{\mathcal{B}}], \tag{3.13}$$

$$\begin{aligned} \mathbf{T}_S = &\frac{\varepsilon c^2}{2\omega^2}\{[\boldsymbol{\mathcal{E}} \otimes (\nabla \times \boldsymbol{\mathcal{E}}) + (\nabla \times \boldsymbol{\mathcal{E}}) \otimes \boldsymbol{\mathcal{E}}] \\ &+ c^2[\boldsymbol{\mathcal{B}} \otimes (\nabla \times \boldsymbol{\mathcal{B}}) + (\nabla \times \boldsymbol{\mathcal{B}}) \otimes \boldsymbol{\mathcal{B}}]\} - \frac{c^2}{\omega^2} C\mathbf{I}. \end{aligned} \tag{3.14}$$

The symmetric tensor $\mathbf{T}_S$ resembles the MST $\mathbf{T}_M$. $-\mathbf{T}_S$ represents the flux density of SAM. The terms on the right-hand side of Eq. (3.13) account for the loss rate of the SAM density of the field. Eq. (3.13) indicates the SAM transfer between the light and matter. As the same as the continuity equations for energy Eq. (2.12), linear momentum Eq. (2.22), and total angular momentum Eq. (2.26), Eq. (3.13) is also an exact consequence of Maxwell's equations, which holds instantaneously for each position without

any averaging. Note that Eq. (2.26) describes the total angular momentum transfer in light-matter interaction and it is a conserved quantity, consequently, the OAM transfer can be obtained by combining Eq. (2.26) and Eq. (3.13). This makes it possible to separately characterize the SAM transfer and OAM transfer. As a result of the SAM transfer and OAM transfer, the optical torques originated from them can be produced on the matter, which we call the spin-transfer torque and orbit-transfer torque, respectively. Thus, the terms on the right-hand side of Eq. (3.13) can be regarded as the spin-transfer torque density on the particle. Based on the flux density of SAM, we can obtain the time-averaged spin-transfer torque:

$$\boldsymbol{\tau}_{spin} = \oint_S \overline{\mathbf{T}}_S \cdot \mathbf{n}\, dS, \tag{3.15}$$

where $\overline{\mathbf{T}}_S$ is the time-averaged $\mathbf{T}_S$.

Furthermore, Eq. (3.15) is a general equation as the same as Eq. (2.27), hence Eq. (3.15) can also be applied to particles of any size, shape, and composition in the presence of arbitrarily structured optical fields. Therefore, the orbit-transfer torque can be obtained by subtracting the spin-transfer torque, i.e., Eq. (3.15), from the total optical torque, i.e., Eq. (2.27). This may help to study the rotational states of nanoparticles and molecules in some opto-mechanical systems.

Up to this point, we have shown the continuity equation for optical chirality and mentioned the continuity equation for optical helicity, as well as their fluxes. Based on the Noether's theorem, they must be associated with symmetries of the electromagnetic action. A requirement for the continuity equations to be true is that these quantities are defined to respect the dual electric-magnetic symmetry, which implies that they are invariant under a duality rotation:

$$\boldsymbol{\mathcal{E}} \rightarrow \boldsymbol{\mathcal{E}}' = \boldsymbol{\mathcal{E}}\cos\theta + c\boldsymbol{\mathcal{B}}\sin\theta, \tag{3.16}$$

$$c\boldsymbol{\mathcal{B}} \rightarrow c\boldsymbol{\mathcal{B}}' = -\boldsymbol{\mathcal{E}}\sin\theta + c\boldsymbol{\mathcal{B}}\cos\theta, \tag{3.17}$$

for any angle θ. Interested readers are referred to Ref [27–29].

3.5 Verification and application

In this section, we will apply Eq. (3.15) and Eq. (2.27) to several examples (*A*, *B*, *C*). *A* and *B* are given as an applicability verification and *C* is an application of our method to analyze the angular momentum transfer between light and matter. The electromagnetic fields were calculated using the finite element method (Simulation software: COMSOL Multiphysics). All the following results were obtained with air as the medium, and the circularly and linearly polarized light used in *A* and *C* were plane waves. We chose plasmonic gold nanostructures as samples due to the strong interaction between them and light. In *A* and *B*, the plasmonic structures were nanorods. Since the transverse plasmon modes of the nanorods with the dimensions we used are negligible relative to their longitudinal plasmon modes, the nanorods can be treated as "needle" particles and the scattered light from them is linearly polarized without SAM or OAM. Therefore, there is no spin-orbit transformation in the interaction between the light and nanorods in the examples. This makes it much easier to analyze the physical mechanism of the spin- and orbit-transfer torque based on the incident light.

■ Verification

A. Gold nanorod illuminated by circularly or linearly polarized light. A circularly polarized light intrinsically has a SAM of $\pm\hbar$ per photon depending on the field rotation direction. On the other hand, a linearly polarized light has no angular momenta because it is given by the sum of the circularly polarized lights with different signs for SAM. Figure 3.1(a) schematically shows the geometric model. A nanorod lying along the *y*-axis is illuminated by a plane wave with an incident angle of φ in the *xz* plane. For the circularly polarized incident light, the optical torque arises from the absorption of the SAM carried by the incident light and the scattering of the incident light with the radiation of the linearly polarized light, i.e., the extinction of the incident SAM. On the other hand, for the linearly polarized incident light without any angular momenta, the optical torque is produced by the generation of SAM in the interference field between the scattered light and the incident light. In both cases, only SAM transfer exists. Therefore, the spin-transfer torque ($\boldsymbol{\tau}_{spin}$) calculated by Eq. (3.15) should be equal to the total optical torque ($\boldsymbol{\tau}_{total}$)

calculated by Eq. (2.27), as shown in Figure 3.1(b). We can see that each component of the spin-transfer torque and that of the total optical torque are equal to each other, which is consistent with the analysis of the physical mechanism.

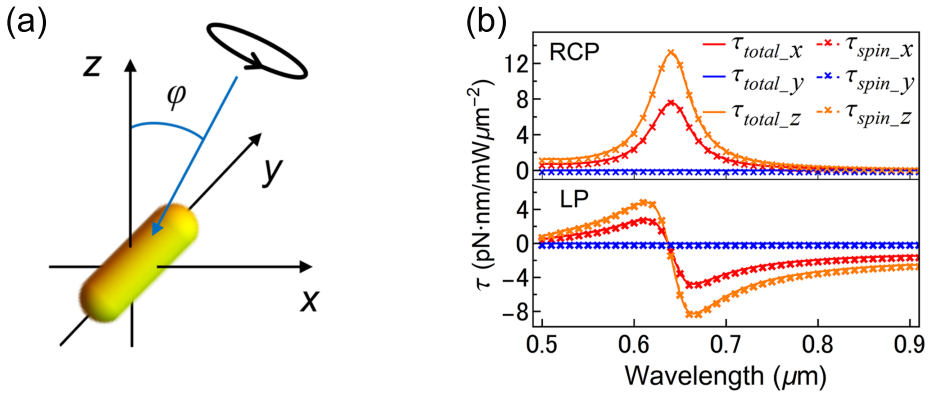

Figure 3.1: (a) Geometric model of a gold nanorod (length: 120 nm, diameter: 40 nm) illuminated by circularly or linearly polarized light. (b) Wavelength dependence of optical torques τ_{total} and τ_{spin} calculated by Eq. (2.27) and Eq. (3.15), respectively, with right circularly (top) and linearly (bottom) polarized light incident at an angle of $\varphi = 30°$. The polarization direction of the linearly polarized light is at an angle of 45° with respect to the longitudinal axis of the nanorod. τ_{total_i} and $\tau_{spin\_i}(i{=}x, y, z)$ represent the different components of the optical torque.

B. Gold nanorod illuminated by a Laguerre Gaussian (LG) beam. The properties of an LG beam can be quantified by its azimuthal mode index $l = 0, \pm1, \pm2, \cdots$, radial mode index $p = 0, 1, 2, \cdots$, and the handedness of circular polarization denoted by $s = \pm1$ [30,31]. l describes the phase distribution around the azimuthal direction of the beam, whereas p decides the number of nodes along the radial direction. Moreover, l and s give rise to an OAM of $l\hbar$ and a SAM of $s\hbar$ per photon, respectively. Here, for simplicity, we confine our discussion to $l = 1$, $p = 0$, that is, a single-ringed beam with an OAM of $\hbar$ per photon. For an LG beam with $l = 1$, the spin-transfer torque can be added to, or subtracted from the orbit-transfer torque to obtain the total optical torque [32].

As shown in Figure 3.2(a), a nanorod lies along the y-axis at the center of the incident LG beam propagating along the z-axis from the negative to the positive direction. Here, we only focus on the z-component of the torques on the nanorod since the torques are negligible for the other components. (i) $l = 1$, $s = 1$. The scattered light from the nanorod is linearly polarized without SAM or OAM. Therefore, optical torque is produced by

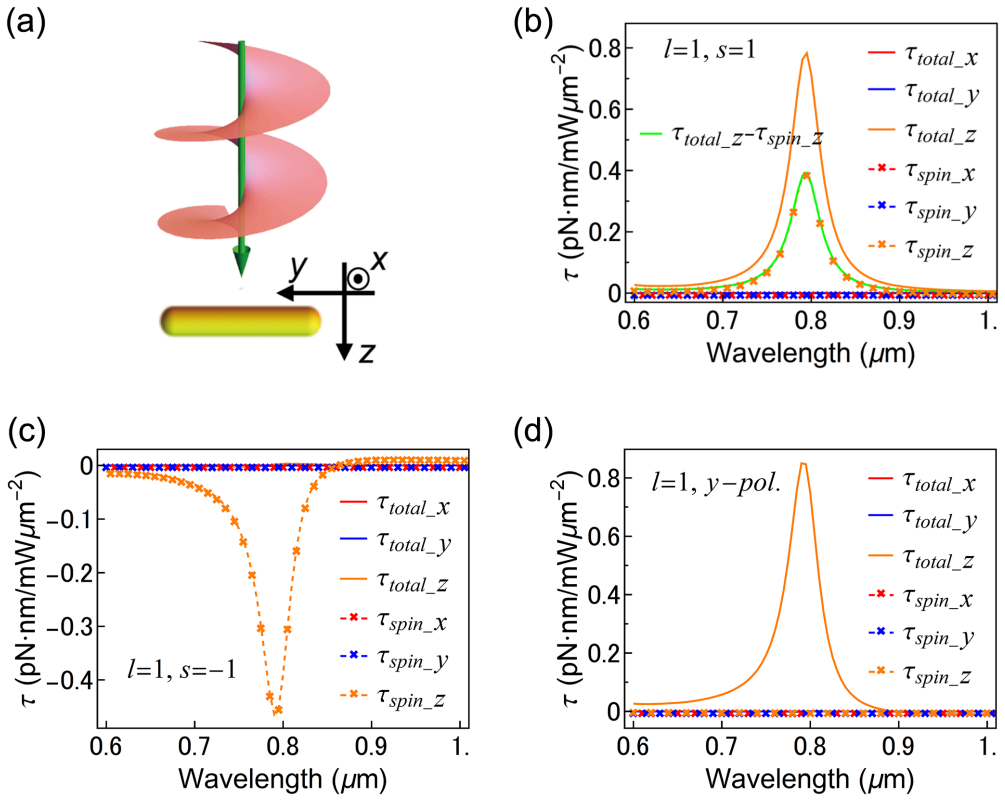

Figure 3.2: (a) Geometric model of a gold nanorod (length: 400 nm, diameter: 40 nm) illuminated by LG beam. (b-d) Wavelength dependence of optical torques τ_{total} and τ_{spin} with the incident light of LG beam with different modes: (b) $l = 1$, $s = 1$, (c) $l = 1$, $s = -1$, and (d) $l = 1$, *y-pol.*.

the extinction of the incident angular momentum. As each photon has SAM and OAM with the same magnitude and sign, the spin-transfer torque (τ_{spin}) and the orbit-transfer torque ($\tau_{total} - \tau_{spin}$) should be equal to each other. As shown in Figure 3.2(b), we can see the results of τ_{spin} obtained by Eq. (3.15) and τ_{total} obtained by Eq. (2.27) show a good agreement with our analysis. (ii) $l = 1$, $s = -1$. The optical torque is produced by the same mechanism as that in (i). The incident light has a negative SAM, producing a spin-transfer torque which has a direction different from that in (i). Therefore, the same magnitude but different signs of SAM and OAM produce the optical torques with the same magnitude but opposite directions, resulting in a total optical torque of zero. However, the spin-transfer torque can still be calculated by Eq. (3.15). This is also supported by the results in Figure 3.2(c). (iii) $l = 1$, *y-pol.*. In this case, only OAM transfer occurs between the nanorod and the light field, inducing an orbit-transfer torque on the nanorod.

Thus, the spin-transfer torque should be zero via the calculation of Eq. (3.15), while the total optical torque is equal to the orbit-transfer torque with a non-zero value, as shown in Figure 3.2(c).

All the above calculation results are consistent with those of previous studies and the analysis of physical mechanisms, indicating that Eq. (3.15) is effective for calculating the spin-transfer torque separately from the orbit-transfer torque. Furthermore, by combining with Eq. (2.27), it provides the potential to separately quantify the SAM transfer and OAM transfer in the interaction between light and matter. In order to obtain a physical insight into such quantification, we consider the following example.

■ Application

C. Gold nanosphere illuminated by circularly polarized light. The geometric model is shown in Figure 3.3(a). A nanosphere is illuminated by a right circularly polarized light propagating along the z-axis from the positive to the negative direction. Interestingly, even though it's an incident light without OAM, the spin-transfer torque (τ_{spin_z}) is not equal to the total optical torque (τ_{total_z}), as shown in Figure 3.3(b). Thus, the OAM along the z-axis should be generated by the interaction between the nanosphere and circularly polarized light. This generation of OAM produced a recoil orbit-transfer torque on the nanosphere. Considering this in Eq. (3.13), the terms on the right-hand side, that is, spin-transfer torque density, include the part that contributes to the generation of OAM due to the spin-orbit interaction, which leads to the difference between the spin-transfer torque and total optical torque in Figure 3.3(b). To confirm the OAM generation, we calculated the phase distribution of the scattered light around the nanosphere as shown in Figures 3.3(d) and 3.3(f). We can observe the phase gradient around the nanosphere in the plane parallel to the xy-plane, which shows the OAM along the z-axis in the scattering field. Additionally, some previous studies have also shown the OAM in the scattering field around the nanosphere illuminated by a circularly polarized light [33–36], which is consistent with our result. These findings may imply that all directions around the nanoparticle should be considered to analyze the OAM of a scattering field. Besides, as the spin-transfer torque and orbit-transfer torque are produced by the extinction of the incident SAM and the generation of OAM, respectively, our method to separately

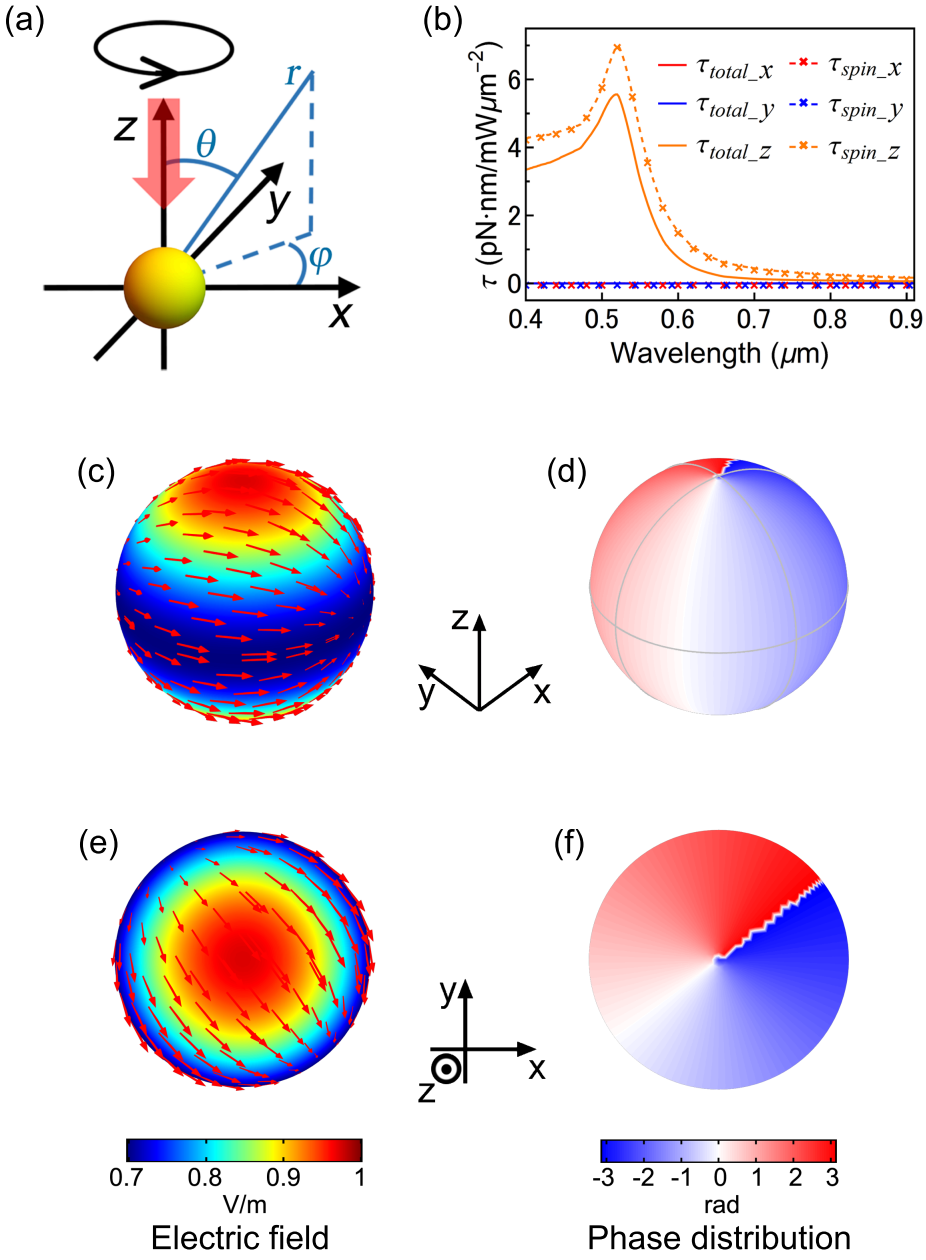

Figure 3.3: (a) Geometric model of a gold nanosphere (diameter: 100 nm) illuminated by right circularly polarized light. (b) Wavelength dependence of optical torques $\boldsymbol{\tau}_{total}$ and $\boldsymbol{\tau}_{spin}$. Electric field (c, e) and phase distribution (d, f) of the scattered light from the nanosphere illuminated by circularly polarized light in the far field at different viewpoints. The red arrows in (c) and (e) show the instantaneous polarization states at different positions on the far-field surface. The rainbow colors in (c) and (e) show the normalized amplitude of the electric field in different directions of the scattered light. The wavelight colors in (d) and (f) show the phase distribution on the far-field surface. The phase is defined as the phase of the φ component of the electric field in the spherical coordinate system (r, θ, φ) transformed from the Cartesian coordinate system (x, y, z) in the figure.

calculate them could be used to quantitatively characterize the transformation efficiency from SAM to OAM with the ratio of the orbit-transfer torque to spin-transfer torque. This quantitative analysis method for the spin-orbit transformation provides a new route to understand and design the spin-orbit interaction systems.

3.6 Summary

In summary, we have presented an approach to quantifing the spin-orbit transformation in the interaction between light and matter based on the separate calculation of spin-transfer torque and orbit-transfer torque. By extending the proportional relation between the chirality flux density and SAM density to sources-added space, we have derived the continuity equation for SAM in analogy with the continuity equation for linear momentum. The derived equation provides a method to separately calculate the spin-transfer torque and orbit-transfer torque by combining with the MST method related to the continuity equation for total angular momentum. This method makes it possible to realize the separate characterization of SAM transfer and OAM transfer between light and matter. What is more, this is a general method that can be applied to any size, shape, and constituent of matter in the presence of arbitrarily structured optical fields. In fact, we revealed that the scattered light of a nanosphere illuminated by circularly polarized light has OAM as well as SAM. The transformation capability from SAM to OAM can also be evaluated based on our method. The separation of spin-transfer torque and orbit-transfer torque may play a significant role in analyzing and designing a spin-orbit interaction system, which can be applied to many fundamental processes such as optical manipulation of nanoparticles and molecules, subwavelength optical probing, and generation of vortex beams. Our approach to separating the SAM transfer and OAM transfer will provide a better understanding of the fundamentals of the physics of the interaction between light and matter.

References

[1] K. Y. Bliokh, F. J. Rodríguez-Fortuño, F. Nori, and A. V. Zayats, "Spin–orbit interactions of light," *Nat. Photonics*, vol. 9, no. 12, p. 796, 2015.

[2] F. J. Rodríguez-Fortuño, N. Engheta, A. Martínez, and A. V. Zayats, "Lateral forces on circularly polarizable particles near a surface," *Nat. Commun.*, vol. 6, p. 8799, 2015.

[3] S. Sukhov, V. Kajorndejnukul, R. R. Naraghi, and A. Dogariu, "Dynamic consequences of optical spin–orbit interaction," *Nat. Photonics*, vol. 9, no. 12, p. 809, 2015.

[4] K. Y. Bliokh, D. Smirnova, and F. Nori, "Quantum spin hall effect of light," *Science*, vol. 348, no. 6242, pp. 1448–1451, 2015.

[5] V. S. Liberman and B. Y. Zel'dovich, "Spin-orbit interaction of a photon in an inhomogeneous medium," *Phys. Rev. A*, vol. 46, no. 8, p. 5199, 1992.

[6] M. J. Padgett and R. Bowman, "Tweezers with a twist," *Nat. Photonics*, vol. 5, no. 6, p. 343, 2011.

[7] K. Y. Bliokh, A. Y. Bekshaev, and F. Nori, "Extraordinary momentum and spin in evanescent waves," *Nat. Commun.*, vol. 5, p. 3300, 2014.

[8] D. Gao, W. Ding, M. Nieto-Vesperinas, X. Ding, M. Rahman, T. Zhang, C. Lim, and C.-W. Qiu, "Optical manipulation from the microscale to the nanoscale: fundamentals, advances and prospects," *Light Sci. Appl.*, vol. 6, no. 9, p. e17039, 2017.

[9] M. Liu, T. Zentgraf, Y. Liu, G. Bartal, and X. Zhang, "Light-driven nanoscale plasmonic motors," *Nat. Nanotechnol.*, vol. 5, no. 8, p. 570, 2010.

[10] A. Lehmuskero, R. Ogier, T. Gschneidtner, P. Johansson, and M. Käll, "Ultrafast spinning of gold nanoparticles in water using circularly polarized light," *Nano Lett.*, vol. 13, no. 7, pp. 3129–3134, 2013.

[11] Z. Bryant, M. D. Stone, J. Gore, S. B. Smith, N. R. Cozzarelli, and C. Bustamante, "Structural transitions and elasticity from torque measurements on dna," *Nature (London)*, vol. 424, no. 6946, p. 338, 2003.

[12] F. M. Fazal and S. M. Block, "Optical tweezers study life under tension," *Nat. Photonics*, vol. 5, no. 6, p. 318, 2011.

[13] X. Liu, J. Li, Q. Zhang, and M. G. Dirbeba, "Separation of chiral enantiomers by optical force and torque induced by tightly focused vector polarized hollow beams," *Phys. Chem. Chem. Phys.*, vol. 21, no. 28, pp. 15339–15345, 2019.

[14] D. M. Lipkin, "Existence of a new conservation law in electromagnetic theory," *J. Math. Phys.*, vol. 5, no. 5, pp. 696–700, 1964.

[15] K. Y. Bliokh and F. Nori, "Characterizing optical chirality," *Phys. Rev. A*, vol. 83, no. 2, p. 021803, 2011.

[16] G. Nienhuis, "Conservation laws and symmetry transformations of the electromagnetic field with sources," *Phys. Rev. A*, vol. 93, no. 2, p. 023840, 2016.

[17] T. G. Philbin, "Lipkin's conservation law, noether's theorem, and the relation to optical helicity," *Phys. Rev. A*, vol. 87, no. 4, p. 043843, 2013.

[18] M. M. Coles and D. L. Andrews, "Chirality and angular momentum in optical radiation," *Phys. Rev. A*, vol. 85, no. 6, p. 063810, 2012.

[19] Y. Tang and A. E. Cohen, "Optical chirality and its interaction with matter," *Phys. Rev. Lett.*, vol. 104, no. 16, p. 163901, 2010.

[20] Y. Tang and A. E. Cohen, "Enhanced enantioselectivity in excitation of chiral molecules by superchiral light," *Science*, vol. 332, no. 6027, pp. 333–336, 2011.

[21] L. V. Poulikakos, P. Gutsche, K. M. McPeak, S. Burger, J. Niegemann, C. Hafner, and D. J. Norris, "Optical chirality flux as a useful far-field probe of chiral near fields," *ACS photonics*, vol. 3, no. 9, pp. 1619–1625, 2016.

[22] M. Schäferling, D. Dregely, M. Hentschel, and H. Giessen, "Tailoring enhanced optical chirality: design principles for chiral plasmonic nanostructures," *Phys. Rev. X*, vol. 2, no. 3, p. 031010, 2012.

[23] T. J. Davis and E. Hendry, "Superchiral electromagnetic fields created by surface plasmons in nonchiral metallic nanostructures," *Phys. Rev. B*, vol. 87, no. 8, p. 085405, 2013.

[24] E. Hendry, T. Carpy, J. Johnston, M. Popland, R. V. Mikhaylovskiy, A. J. Lapthorn, S. M. Kelly, L. D. Barron, N. Gadegaard, and M. Kadodwala, "Ultrasensitive detection and characterization of biomolecules using superchiral fields," *Nat. Nanotechnol.*, vol. 5, no. 11, p. 783, 2010.

[25] L. Kang, Q. Ren, and D. H. Werner, "Leveraging superchiral light for manipulation of optical chirality in the near-field of plasmonic metamaterials," *ACS Photonics*, vol. 4, no. 6, pp. 1298–1305, 2017.

[26] J. E. Vázquez-Lozano and A. Martínez, "Optical chirality in dispersive and lossy media," *Phys. Rev. Lett.*, vol. 121, no. 4, p. 043901, 2018.

[27] M. Calkin, "An invariance property of the free electromagnetic field," *Am. J. Phys.*, vol. 33, no. 11, pp. 958–960, 1965.

[28] S. M. Barnett, "Rotation of electromagnetic fields and the nature of optical angular momentum," *J. Mod. Opt.*, vol. 57, no. 14-15, pp. 1339–1343, 2010.

[29] R. P. Cameron, S. M. Barnett, and A. M. Yao, "Optical helicity, optical spin and related quantities in electromagnetic theory," *New J. Phys.*, vol. 14, no. 5, p. 053050, 2012.

[30] Q. Zhan, "Cylindrical vector beams: from mathematical concepts to applications," *Adv. Opt. Photonics*, vol. 1, no. 1, pp. 1–57, 2009.

[31] L. Allen and M. J. Padgett, "The poynting vector in laguerre–gaussian beams and the interpretation of their angular momentum density," *Opt. Commun.*, vol. 184, no. 1-4, pp. 67–71, 2000.

[32] N. B. Simpson, K. Dholakia, L. Allen, and M. J. Padgett, "Mechanical equivalence of spin and orbital angular momentum of light: an optical spanner," *Opt. Lett.*, vol. 22, no. 1, pp. 52–54, 1997.

[33] C. Triolo, A. Cacciola, S. Patanè, R. Saija, S. Savasta, and F. Nori, "Spin-momentum locking in the near field of metal nanoparticles," *ACS Photonics*, vol. 4, no. 9, pp. 2242–2249, 2017.

[34] J. Olmos-Trigo, C. Sanz-Fernández, F. S. Bergeret, and J. J. Sáenz, "Asymmetry and spin-orbit coupling of light scattered from subwavelength particles," *Opt. Lett.*, vol. 44, no. 7, pp. 1762–1765, 2019.

[35] C. Schwartz and A. Dogariu, "Conservation of angular momentum of light in single scattering," *Opt. Express*, vol. 14, no. 18, pp. 8425–8433, 2006.

[36] K. Y. Bliokh, E. A. Ostrovskaya, M. A. Alonso, O. G. Rodríguez-Herrera, D. Lara, and C. Dainty, "Spin-to-orbital angular momentum conversion in focusing, scattering, and imaging systems," *Opt. Express*, vol. 19, no. 27, pp. 26132–26149, 2011.

Chapter 4

Optical torque between twisted metal nanorods induced by plasmon coupling

4.1 Introduction

In Chapter 3, we have proposed a quantitative analysis method for the optical spin-orbit transformation in light-matter interaction. This method is based on the transfer of angular momentum between light and matter, which produces optical torque on the matter. Here, we continue the discussion of optical torque.

Optical torque is a measure of how much a force acting on an object causes that object to rotate. Compared with the optical force, it provides a rotational mechanical degree of freedom to manipulate objects. The optical torque can be produced via absorption and scattering processes in light-matter interaction [1–4]. Figure 4.1(a) describes that a particle absorbs the spin angular momentum carried by incident circularly polarized

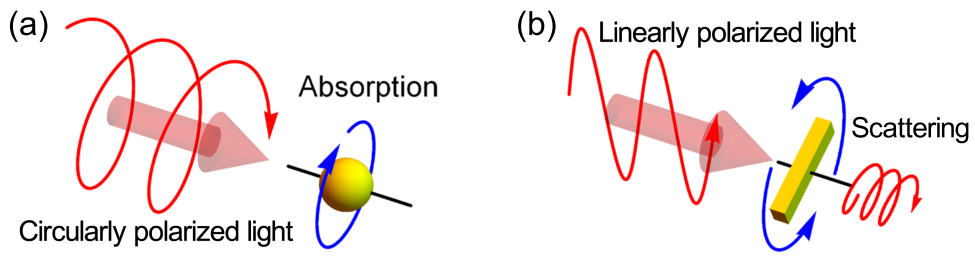

Figure 4.1: Schematic illustration of optical torque produced via absorption (a) and scattering (b).

light to produce the optical torque. However, in Figure 4.1(b), the incident light is a linearly polarized light without angular momentum. In this case, due to the interference between the scattered light from the plasmonic metal nanorod and incident light, angular momentum can be generated and results in a recoil optical torque on the nanorod. Therefore, owing to the important role of optical torque in optical manipulation, it has been attracting widespread attention with a variety of applications in physics, chemistry, and biology [5–10].

In recent years, with the development of plasmonics and nanotechnology, plasmonic nanostructures have significantly furthered these studies due to the excitation of localized surface plasmon resonance (LSPR). As introduced in Chapter 2, the excitation of LSPR gives rise to an intense near field on the nanoparticle surface and enhances the optical cross section in absorption and scattering [11–13]. Furthermore, the plasmonic characteristics strongly depend not only on the nanoparticle size and shape but also on the configurations of the particles, e.g., their separation, orientation, and so on [14–17]. In particular, when two nanoparticles are close to each other, their plasmon coupling occurs owing to the strong interactions as shown in Figure 4.2 [15–17], resulting in an appearance of two plasmon modes different from individual constituents. The plasmon resonances and the near-field enhancement effects of these hybridized modes are significantly changed by the nanoparticle configurations [18–22]. In other words, we can efficiently control the plasmon characteristics through the configurations with the plasmon coupling. The plasmon coupling between nanoparticles drastically enhances the electromagnetic (EM) field in the narrow gap separating them. Over many decades, extensive investigations on the basis of plasmon coupling have been carried out, promoting the applications of plasmonics, such as surface-enhanced fluorescence [23, 24], surface-enhanced Raman scattering [25, 26], chemical sensors, and biosensors [27, 28], and high harmonic generation [29, 30].

In some previous studies, it has been reported that the strong interaction between plasmonic nanoparticles induced by plasmon coupling can produce an interaction optical force between the nanoparticles as shown in Figure 4.2 [31, 32]. This interaction optical force provides a possible approach for assembly control of the nanoparticles [33–35], which plays a crucial role in optical arrangement with a variety of applications, such as contactless control of plasmonic properties, e.g., plasmon resonance control and field en-

hancement, and high-precision plasmonic nanodevices. However, it is easy to imagine that interaction optical torque can also play a significant role in the optical arrangement because it provides a rotational mechanical degree of freedom to manipulate particles. However, it is certainly surprising that few works are trying to systematically study the interaction optical torque.

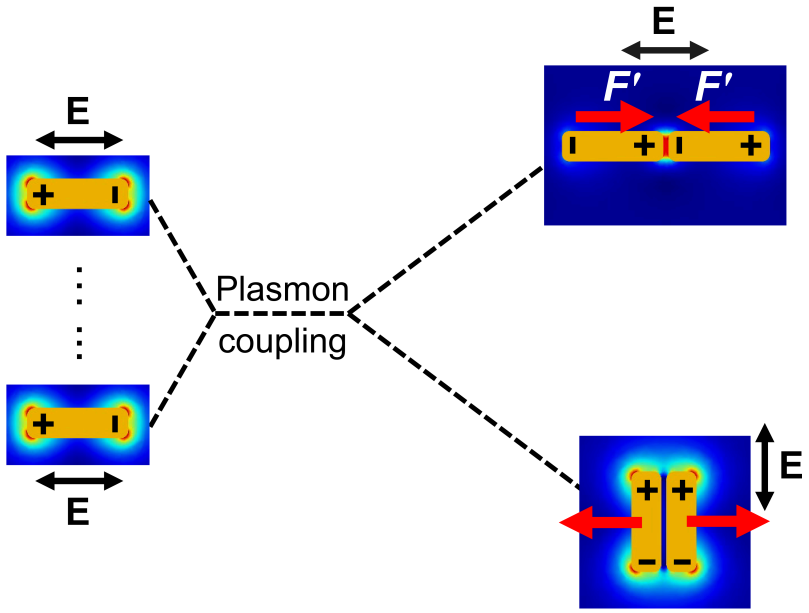

Figure 4.2: Schematic illustration of the interaction optical force induced by plasmon coupling between two nanorods.

Therefore, in this chapter, we study the interaction optical torque induced by plasmon coupling in a dimer of twisted metal nanorods. We start with the plasmon coupling in the dimer which can be explained by the theory of plasmon hybridization. We then discuss the optical torque in the twisted nanorods system. We study the direct relation between the optical torque and plasmon coupling between the twisted metal nanorods. The results indicate that the behaviors of the interaction optical torque at hybridized modes are different from that of an isolated nanorod, which depends not only on the gap size but also on the twisted angle between the nanorods. This interaction optical torque implements the rotations to mutually perpendicular and parallel arrangements of nanorods with the light excitations of different hybridized modes. Thus, the interaction optical torque induced by the plasmon coupling would play an important role to control the plasmonic characteristics and functions. We also analyze the interaction spin- and orbit-transfer torque between

the two nanorods based on the analysis method proposed in Chapter 3, which leads to the topic we will discuss in Chapter 5.

4.2 Simulation method

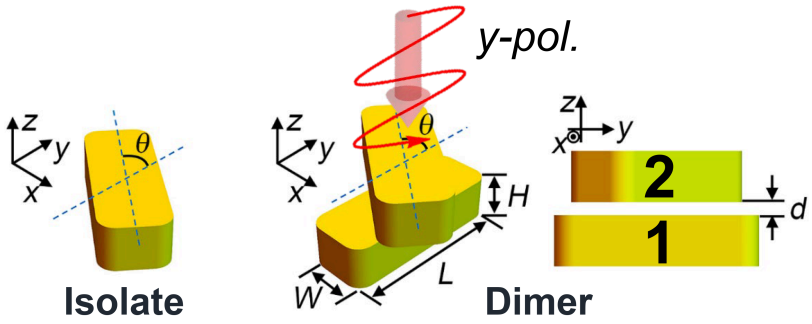

Figure 4.3: Schematic illustration of twisted gold nanorods with gap size d, twisted angle θ, and definitions of the geometrical parameters: L = 165 nm, W = 50 nm, H = 40 nm.

In order to simply excite and observe the plasmon hybridized modes, we chose a dimer of twisted nanorods as shown in Figure 4.3. The two nanorods are separated by gap size d, and they are twisted by angle θ. The dimer was comprised of twisted gold nanorods with definitions of the geometrical parameters: L = 165 nm, W = 50 nm, H = 40 nm. The long axis of Rod 1 was fixed along the y-axis. Conversely, Rod 2 was rotatable for changing the twisted angle. The dimer was irradiated by a y-polarized plane wave to propagate along the z-axis from the positive to the negative direction. We chose the linearly polarized light without any intrinsic angular momentum, which simplifies the analysis of the physical mechanism on the optical torque. The refractive index of the surrounding medium was 1.45.

The optical torque on the nanorods was calculated based on the Maxwell stress tensor (MST) method introduced in Chapter 2 and the equation proposed in Chapter 3, i.e., Eq. (2.27) and Eq. (3.15), with the EM field simulated by using the finite element method (COMSOL Multiphysics). Another approach based on the dipole approximation is also presented to qualitatively study the physics of optical torque in the dimer. Here, we discuss the optical torque only along the z-axis because the torques along the x-and y-axes

are negligibly small.

The plasmon coupling was characterized by the extinction cross section which is the sum of absorption and scattering cross sections. In our simulation, the scattering cross section is defined as

$$\sigma_{sc} = \frac{1}{I_0} \oint_S \boldsymbol{S} \cdot \mathbf{n}\, dS, \tag{4.1}$$

where $\boldsymbol{S}$ is the Poynting vector, I_0 is the incident intensity, S is an arbitrary closed surface surrounding the dimer, $\mathbf{n}$ is the outward normal unit vector to its surface. The absorption cross section is defined as

$$\sigma_{abs} = \frac{1}{I_0} \int_V Q\, dV, \tag{4.2}$$

where Q is the power loss density in the dimer and the integral is taken over its volume V. Therefore, the extinction cross section can be obtained by

$$\sigma_{ext} = \sigma_{sc} + \sigma_{abs}, \tag{4.3}$$

4.3 Plasmon coupling between twisted nanorods

4.3.1 Plasmon spectra of twisted nanorods

In the dimer of twisted nanorod, the gap size d and twisted angle θ are two crucial parameters to determine its configuration. Therefore, we calculated both the gap size dependence and twisted angle dependence of the plasmon coupling between the two nanorods. Figure 4.4(a) shows the plasmon resonance spectra of an isolated nanorod and its dimer at a twisted angle of $\pi/6$ with different gap sizes. As the gap size decreases, the resonance peak of individual nanorods, i.e., the isolated nanorod, starts to split and shifts to short and long wavelengths due to the plasmon coupling between the nanorods in short and long wavelength ranges, respectively. We can also observe similar spectral behavior in the twisted angle dependence for the dimer with a gap size of 15 nm, as shown in Figure 4.4(b). As the twisted angle increases and decreases, the separation between two resonance peaks decreases and increases, respectively. At the twisted angle of $\pi/2$, the dimer exhibits only one resonance peak with a small shift from the resonance peak of the isolated nanorod, in other words, the interaction between the two nanorods with a twisted

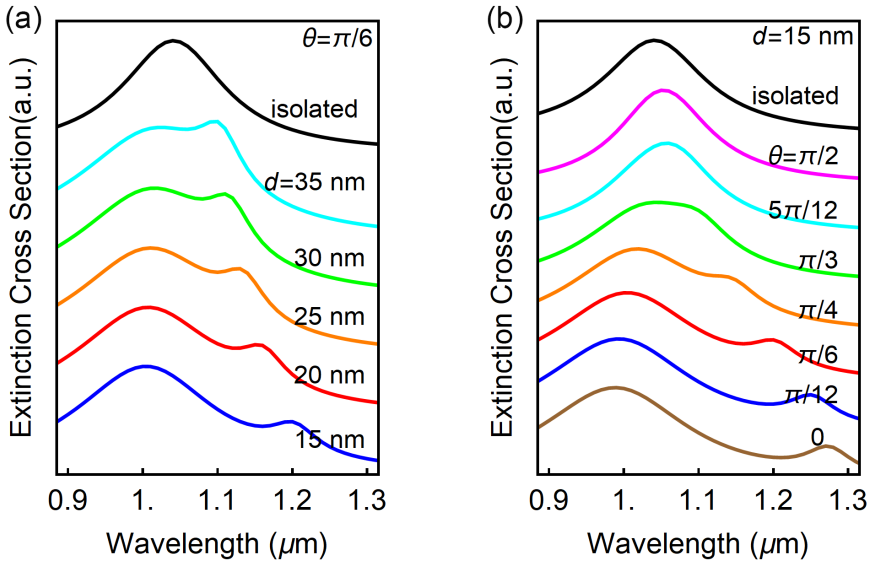

Figure 4.4: Plasmon resonance spectra of an isolated nanorod and its dimer: (a) gap size dependence ($\theta = \pi/6$) and (b) twisted angle dependence (d = 15 nm).

angle of $\pi/2$ is not strong enough to induce plasmon coupling between them. These results indicate that the plasmon coupling between twisted nanorods can be controlled by not only the gap size but also the twisted angle and increases with the decreases of gap size and twisted angle.

4.3.2 Plasmon hybridization of twisted nanorods

To understand the plasmon coupling between the twisted nanorods, it can be described as an elegant physical picture which is plasmon hybridization in analogy with molecular orbital theory [15-19]. Each nanorod can be approximated as a dipole with energy U. When two nanorods are close to each other, plasmon hybridization occurs, generating two new plasmon modes: anti-bonding mode and bonding mode as shown in Figure 4.5. These two hybridized modes are corresponding to a higher energy U_+ and a lower energy U_- respectively, which are produced by splitting from the degenerate energy level U. For the anti-bonding mode, two dipoles are arranged in a parallel manner, i.e., in phase. The charges with the same sign at the edges of nanorods result in a higher energy mode due to the charge repulsion. In this case, the dipole moments add up constructively. It is therefore referred to as a bright plasmon mode that shows a large cross section (see Figure 4.4).

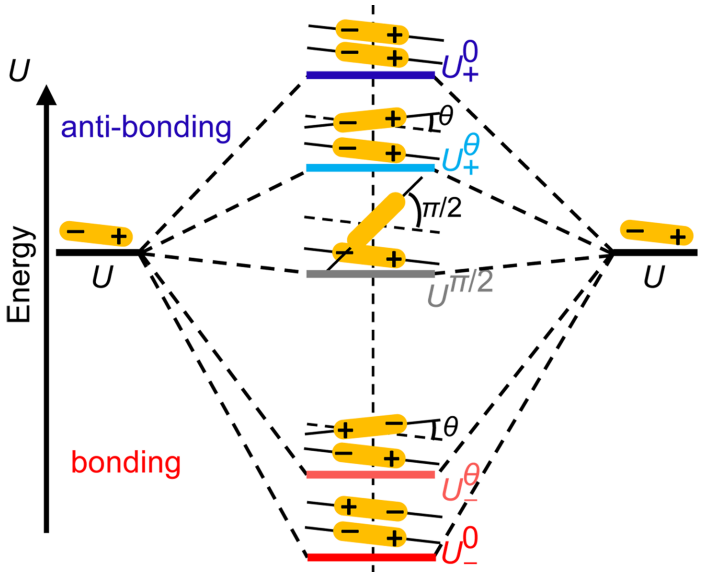

Figure 4.5: Plasmon hybridization diagram in nanorod dimer with twisted angle θ. The polarization direction of the incident light is along the longitudinal axis of the bottom nanorod.

However, for the bonding mode, the dipoles are in an anti-parallel alignment that shows opposite charges at the edges of the nanorods, reducing the charge repulsion and leading to a lower energy. In this case, the destructive superposition of the dipole moment produces a dark plasmon mode that exhibits a small cross section (see Figure 4.4) with a strong enhanced near field. In the dimer of twisted nanorods (Figure 4.5), the decrease of the twisted angle, as well as the gap size, would relieve the charge repulsion for bonding mode but inverse for anti-bonding mode, resulting in the LSPR redshift and blueshift at bonding mode and anti-bonding mode, respectively. Additionally, at the twisted angle of $\pi/2$, the charge repulsion between two nanorods vanishes away due to the orthogonal dipoles, so that plasmon hybridization (coupling) does not occur.

4.4 Optical torque on the twisted nanorods

4.4.1 Optical torque calculated by the Maxwell stress tensor method

In this section, we will discuss the optical torque on the twisted nanorods based on the MST method and the relation with the plasmon coupling. Figure 4.6 shows the optical

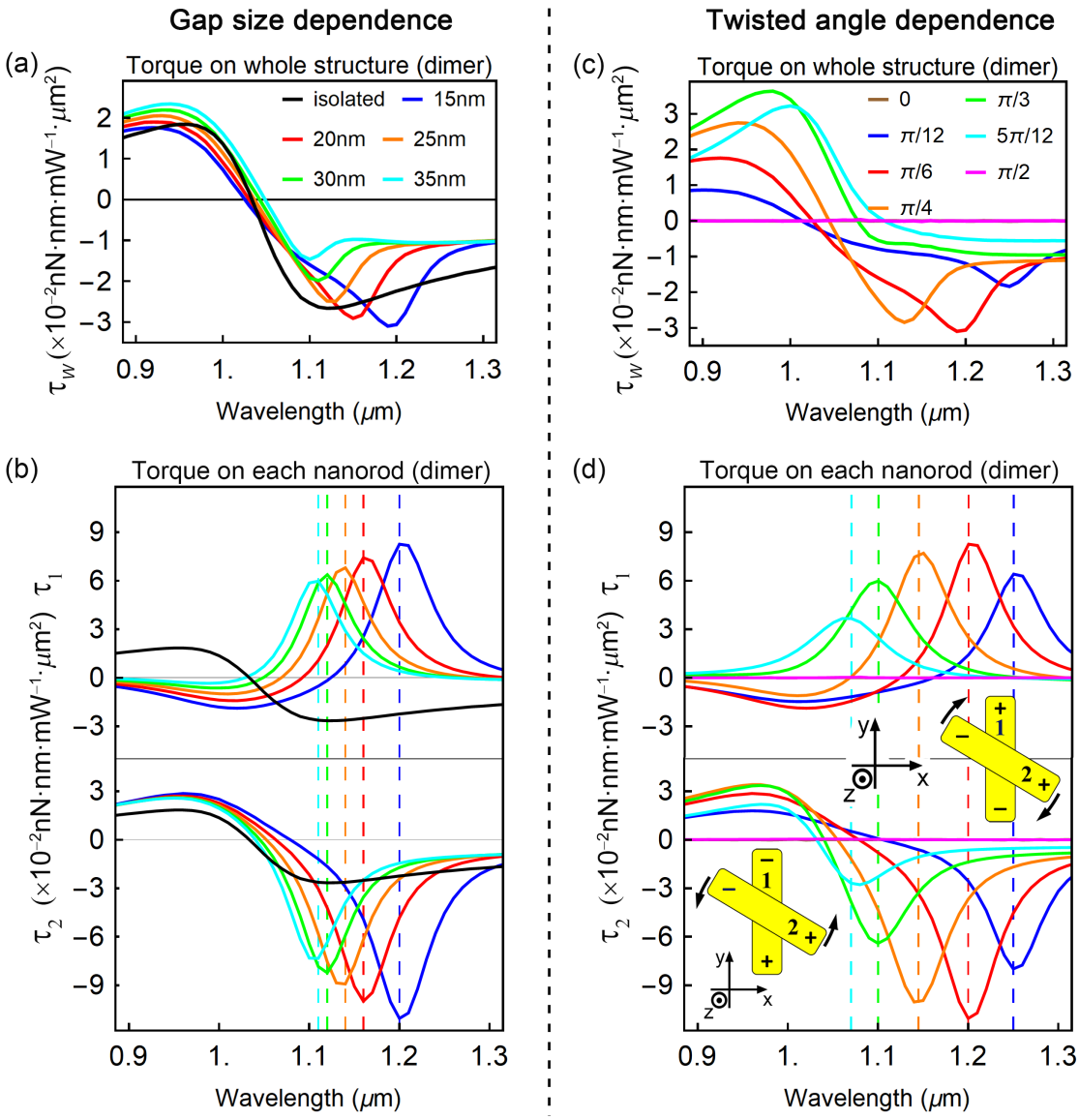

Figure 4.6: Optical torque acting on (a, c) the whole dimer and (b, d) on each nanorod: (a, b) gap size dependence ($\theta = \pi/6$) and (c, d) twisted angle dependence (d = 15 nm). The dashed lines show the peak wavelengths at the redshifted resonance. The insets in (d) show the rotation directions of Rod 2 at the anti-bonding mode and bonding mode.

torque applied to the twisted nanorods. The behaviors of the optical torque strongly depend on the gap size and the twisted angle between the nanorods. The magnitude of the torque on the whole dimer at the resonance wavelength is similar to that on the isolated nanorod, even in the case of the strong plasmon coupling between the nanorods, i.e., small gap size and twisted angle. However, the optical torque on each nanorod in the dimer can be remarkably enhanced by the plasmon coupling, leading to more than 4.2 times as large as that on the isolated nanorod. It should be noted that the extinction cross section at the redshifted plasmon resonance (bonding mode) is much smaller than that at the blueshifted plasmon resonance (anti-bonding mode) in Figure 4.4, whereas the magnitude of the optical torque at the redshifted resonance is much larger than that at the blueshifted resonance in Figures 4.6(b) and 4.6(d).

Let us discuss the spectral shape and the mechanism of the optical torques on the twisted nanorods. When a linearly polarized field **E** illuminates an isolated nanorod, the time-averaged optical torque on the induced dipole moment **p** of the nanorod can be simply expressed as [36, 37]

$$\boldsymbol{\tau}_i = \frac{1}{2}\mathrm{Re}[\mathbf{p} \times \mathbf{E}^*], \tag{4.4}$$

where $*$ denotes the operation of conjugation. This optical torque is produced by the generation of the angular momentum owing to the interference between scattered light from the oscillating dipole moment **p** and the incident light field **E**. For longer and shorter wavelengths of the incident light than the wavelength at plasmon resonance peak of isolated nanorod in Figure 4.4, the nanorod experiences the negative and positive torque, respectively, as shown in Figure 4.6 (a) (also see Figure 4.10 in Subsection 4.4.2), because the phase difference between the dipole moment **p** and the incident light **E** changes from 0 to π around the resonance peak. At the resonance peak, the total angular momentum of the interference field keeps zero, hence, there is no optical torque on the nanorod. In addition, when the incident field is polarized parallel or perpendicular to the long axis of the nanorod, i.e., $\theta = 0, \pi/2$, the optical torque disappears because of no generation of the angular momentum. In the case of the twisted nanorod dimer, the optical torque in Figures 4.6(a) and 4.6(c) arises from two different mechanisms. One of them is due to the angular momentum in the interference field between the scattered light and the incident light, which is similar to that for the isolated nanorod. The other one is due to the different

absorption cross section of the left-handed and the right-handed circularly polarized light with positive and negative spin angular momentums, respectively, because of the chirality of the dimer ($\theta \neq 0, \pi/2$), which is highly associated with the plasmon coupling in the dimer. At the anti-bonding mode, the optical torque induced by the former is dominant because it is a bright mode with a large scattering cross section, resulting in the spectral behavior similar to that of the isolated nanorod. However, at the bonding mode, the optical torque induced by the latter is dominant because it is a dark mode with much small scattering cross section comparing with that at anti-bonding mode while the difference between the absorption cross sections of the left-handed and the right-handed circularly polarized light shows a very large chirality of the dimer as shown in Figure 4.7. Therefore, its spectral shape is similar to the absorption cross section.

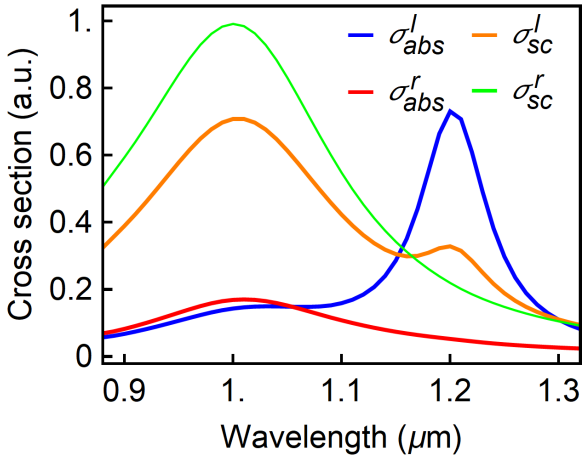

Figure 4.7: Absorption and scattering cross sections of the twisted gold nanorods dimer with gap size and twisted angle of 15 nm and $\pi/6$, respectively, for the illumination of left- and right-handed circularly polarized light.

For each nanorod in the dimer, the optical torque is determined by the scattered field from the other nanorod together with the incident light. In Figures 4.6(b) and 4.6(d), the directions of optical torque on the two nanorods are opposite while their magnitudes are close to each other. In other words, each nanorod dominantly experiences an optical torque due to the angular momentum of the EM field arising from the interaction between the two nanorod-plasmons, i.e., interaction optical torque. Therefore, the sign of the optical torque on the nanorods should be decided by the phase difference between the dipole moments of the two nanorods. For the anti-bonding mode, the two dipoles are in phase,

producing a negative torque on Rod 1 and a positive torque on Rod 2. Conversely, for the bonding mode, the dipoles are out of phase. The optical torques on Rod 1 and Rod 2 are positive and negative, respectively. Moreover, because the scattering loss at the bonding mode is much smaller than that at the anti-bonding mode, the near field between two nanorods can be much more strongly enhanced at the bonding mode than at the anti-bonding mode, as shown in Figure 4.8. This results in a much larger magnitude of the interaction optical torque at the bonding mode than at the anti-bonding mode even though the extinction cross section at the bonding mode is smaller than that at the anti-bonding mode. Additionally, in the case of the two nanorods parallel and perpendicular to each other, i.e., $\theta = 0, \pi/2$, the EM field does not possess the angular momentum, resulting in no optical torque on the nanorods.

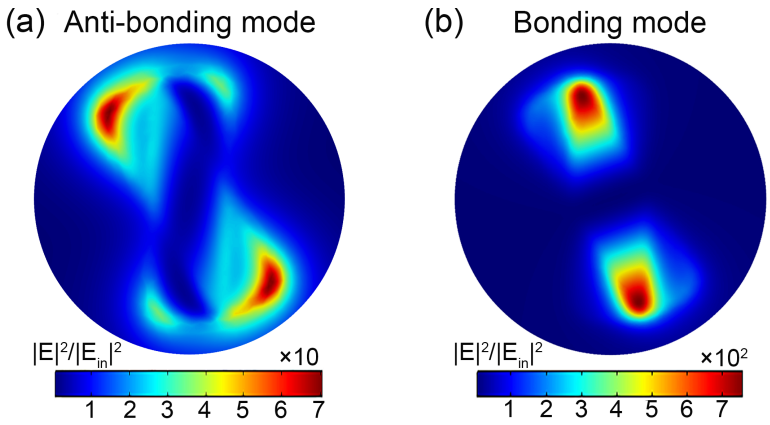

Figure 4.8: Distributions of the field (intensity) enhancement at the gap center plane between the two nanorods at (a) anti-bonding mode (λ = 1000 nm) and (b) bonding mode (λ = 1200 nm), respectively, with the gap size of 15 nm and twisted angle of $\pi/6$.

4.4.2 Optical torque calculated by the dipole approximation method

In the preceding subsection, we have discussed the optical torque on the twisted nanorods calculated by the MST method using the finite element method. Here, we introduce another approach based on the dipole approximation to confirm the spectral behavior of the optical torque on each nanorod. The dipole approximation method is a widely utilized method to calculate the optical torque. A nanorod can be approximated as a dipole with dipole moment $\mathbf{p}$, which is decided by the polarizability $\boldsymbol{\alpha}$ of the nanorod. The induced dipole moment $\mathbf{p}$ of the nanorod illuminated by an arbitrary monochromatic incident elec-

tric field $\mathbf{E}$ can be expressed as $\mathbf{p} = \boldsymbol{\alpha} \cdot \mathbf{E}$.

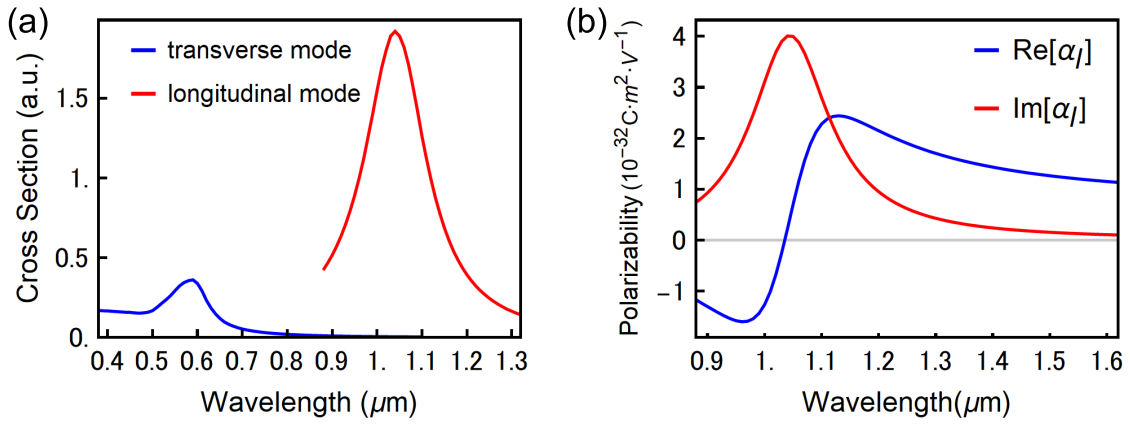

Figure 4.9: (a) Plasmon resonance spectra of an isolated gold nanorod at longitudinal mode and transverse mode. (b) Longitudinal polarizability of the gold nanorod calculated by the finite element method. The definitions of the geometrical parameters of the nanorod: $L = 165$ nm, $W = 50$ nm, $H = 40$ nm

Since the transverse plasmon modes of the nanorods with the dimensions we used are negligible relative to their longitudinal plasmon modes as shown in Figure 4.9(a), the transverse polarizability of the nanorod is negligible and we only consider the longitudinal polarizability α_l. Figure 4.9(b) shows the real part and imaginary part of α_l. Hence, with the incident field of y-polarized plane wave $\mathbf{E}$ to propagate along the z-axis from the positive to the negative direction as shown in Figure 4.3, the time-averaged optical torque on an isolated nanorod rotated with an angle of θ can be obtained by [36, 37]

$$\boldsymbol{\tau}_i = \frac{1}{2}\mathrm{Re}[\mathbf{p} \times \mathbf{E}^*] = -\frac{1}{4}\mathrm{Re}[\alpha_l]\sin 2\theta |\mathbf{E}|^2 \mathbf{e}_z, \tag{4.5}$$

where $\mathbf{e}_z$ is the unit vector along the z-axis. Eq. (4.5) shows a good agreement with the results calculated by the MST method as shown in Figure 4.10. According to Eq. (4.5), the direction of optical torque is decided by the sign of the real part of α_l. Under the situation of $0 < \theta < \pi/2$, $\mathrm{Re}[\alpha_l]$ is positive in the longer wavelength region than the resonance peak wavelength. The phase difference between the dipole moment $\mathbf{p}$ and the incident electric field $\mathbf{E}$ is in the range of 0 to $\pi/2$. The optical torque is negative. In the short wavelength region, $\mathrm{Re}[\alpha_l]$ is negative, that is, the phase difference between $\mathbf{p}$ and $\mathbf{E}$ is in the range of $\pi/2$ to π. The optical torque is positive. Additionally, when the phase

difference between **p** and **E** is $\pi/2$, i.e., $\mathrm{Re}[\alpha_l] = 0$, the optical torque is 0.

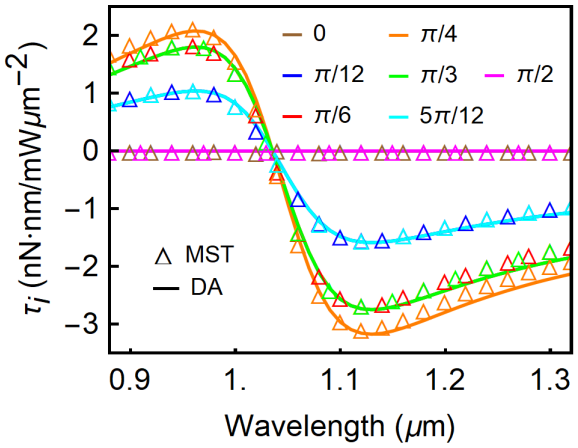

Figure 4.10: Optical torque on an isolated nanorod with different rotation angles. The solid line and triangle with different colors represent the torques calculated by the dipole approximation method and MST method, respectively.

In order to calculate the optical torque acting on each nanorod in the dimer of twisted nanorods, we need to calculate the electric field on each nanorod. Base on the dipole radiation introduced in Subsection 2.3.2, each component of the electric field on each nanorod can be expressed as

$$\mathbf{E}_1 = \begin{pmatrix} -\frac{A+A^2\exp[ik(d+H)]}{1-A^2\cos^2\theta}\sin\theta\cos\theta \mathrm{E}_y \\ \frac{\exp[ik(d+H)]+A\cos^2\theta}{1-A^2\cos^2\theta}\mathrm{E}_y \\ 0 \end{pmatrix}, \tag{4.6}$$

$$\mathbf{E}_2 = \begin{pmatrix} 0 \\ \frac{1+A\exp[ik(d+H)]}{1-A^2\cos^2\theta}\mathrm{E}_y \\ 0 \end{pmatrix}, \tag{4.7}$$

$$A = \frac{\alpha_l \exp[ik(d+H)]}{4\pi\varepsilon(d+H)}[k^2 + \frac{ik(d+H)-1}{(d+H)^2}], \tag{4.8}$$

where θ is the twisted angle of the dimer, k is the wavenumber, ε is the permittivity of the surrounding medium, d is the gap size in the dimer, H is the height of the nanorods, and

E_y is the y component of the incident light. Thus, the optical torques on Rod 1 and Rod 2 can be expressed as

$$\boldsymbol{\tau}_1 = \frac{1}{4}\mathrm{Re}[\alpha_l \frac{(A + A^2\exp[ik(d+H)])^*(\exp[ik(d+H)] + A\cos^2\theta)}{|1 - A^2\cos^2\theta|^2}]\sin 2\theta |\mathbf{E}|^2 \mathbf{e}_z, \quad (4.9)$$

$$\boldsymbol{\tau}_2 = \frac{1}{4}\mathrm{Re}[\alpha_l](\frac{|1 + A\exp[ik(d+H)]|^2}{|1 - A^2\cos^2\theta|^2}]\sin 2\theta |\mathbf{E}|^2 \mathbf{e}_z, \quad (4.10)$$

where $*$ denotes the operation of conjugation.

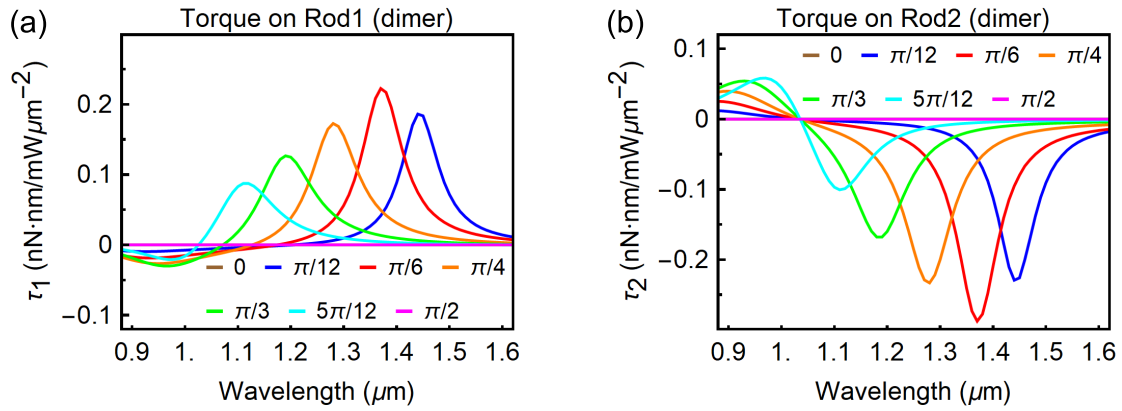

Figure 4.11: Twisted angle dependence of optical torques on (a) Rod 1 and (b) Rod 2 calculated by the dipole approximation method as a function of wavelength. The gap size was fixed as 40 nm .

Though the dipole approximation method can not perfectly describe the plasmon coupling between the twisted nanorods, it is a helpful method to qualitatively reveal the physics of the interaction optical torque between the twisted nanorods. Figure 4.11 shows the twisted angle dependence of the optical torques on the Rod 1 and Rod 2 calculated by Eqs. (4.9) and (4.10), respectively. The shapes of the curves show a similar tendency with the results calculated by the MST method in Figure 4.6(d). For the optical torque on Rod 2, we can see the enhancement of optical torque arises from the enhancement of the electric field that illuminates on the nanorods by comparing Eqs. (4.10) and (4.5). In the redshifted resonance region (bonding mode), because the real part of polarizability changes slowly, as shown in Figure 4.9(b), the enhancement of the electric field dominates the change of the optical torque, which is associated with the plasmon coupling resonance. Thus, the peak of optical torque is corresponding to that of the plasmon

coupling resonance. In the blueshifted resonance region (anti-bonding mode), the real part of polarizability varies drastically, determining the variation tendency of the optical torque. At the peak wavelength of the plasmon resonance of an individual nanorod, we can find the optical torque is 0 in Figure 4.11(b) because the real part of polarizability is 0. However, the dipole approximation method cannot completely describe the plasmon-coupling-determined characteristics of the near field in the dimer, such as the polarization state distribution in the near field. Therefore, the optical torque shows slight changes from that in Figure 4.6(d) (τ_2). For the optical torque on Rod 1, we can see the electric field on Rod 1 is not a linearly polarized light as described by Eq. (4.6). In this case, the optical torque calculated by Eq. (4.9) is decided by not only the real part of polarizability but also the imaginary part of polarizability. Hence, in the blueshifted resonance region, the spectral behavior of optical torque is different from that of the optical torque on Rod 2. On the other hand, in the redshifted resonance region, it is similar to the optical torque on Rod 2 because the enhancement of the electric field dominates the variation of optical torque. The peak of optical torque is in accordance with that of plasmon coupling resonance as well.

4.4.3 Optical arrangement in practical application

Having investigated the optical torque on the twisted nanorods, we further explore the optical arrangement of the twisted nanorods in a practical application induced by the interaction optical torque. As shown in the inset of Figure 4.6(d), the optical torques on Rod 2 show different signs at the anti-bonding mode and bonding mode, leading to an anti-clockwise rotation and a clockwise rotation at the anti-bonding mode and bonding mode, respectively. As the Rod 1 is fixed along the y-axis, the rotations of Rod 2 at the anti-bonding mode and bonding mode result in mutually perpendicular and parallel arrangements of the nanorods, i.e., $\theta = \pi/2$ and 0, respectively.

Considering this optical arrangement dependent on the incident light wavelength in a practical application, the rotational potential energy induced by the torque on the Rod 2 should be large enough to overcome the Brownian motion energy, which should be considered in dealing with optical trapping and manipulation. The average energy of the Brownian motion associated with each degree of freedom can be expressed as $k_B T/2$ in a

system at thermodynamic equilibrium, where k_B is the Boltzmann constant, and T is the absolute temperature. Interested readers in the detail of Brownian motion are referred to Ref [38]. In this system, the temperature T will increase due to the light absorption of the nanorods which depends on their configurations. To simplify the discussion, we keep T at 300 K. We define the rotational potential energy as

$$U_P = \int_{\theta_0}^{\theta} \tau \, d\theta, \tag{4.11}$$

where θ_0 is the starting angle of the integral.

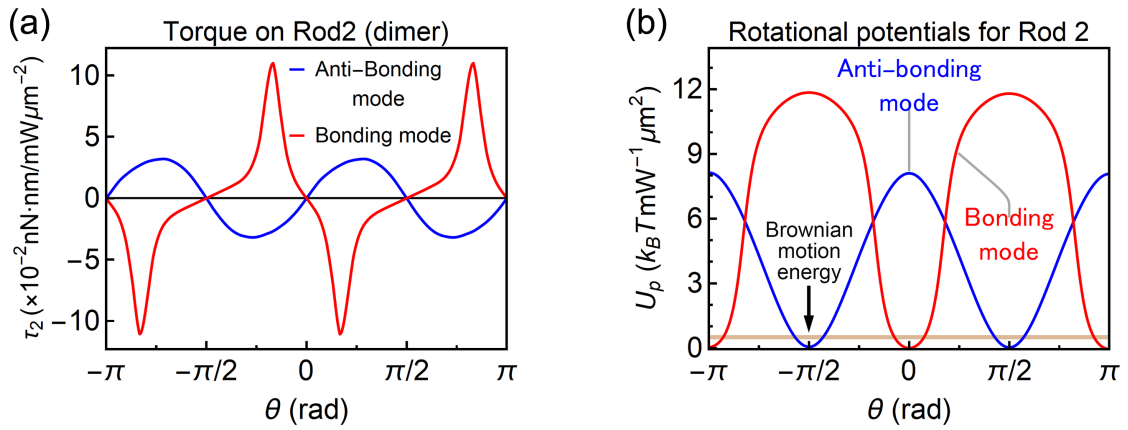

Figure 4.12: (a) Calculated optical torque on Rod 2 at the anti-bonding mode (λ = 930 nm) and bonding mode (λ = 1200 nm). (b) Rotational potentials in units of k_BT (T = 300 K) for Rod 2 as a function of the twisted angle at the anti-bonding mode (λ = 930 nm) and bonding mode (λ = 1200 nm). The gap size between the twisted nanorods was fixed as 15 nm. The brown line shows the Brownian motion energy $k_BT/2$.

Here, we chose a wavelength of 930 nm at the anti-bonding mode and 1200 nm at the bonding mode. Figure 4.12(a) shows the optical torques on Rod 2 depending on the twisted angle at the anti-bonding mode and bonding mode. Based on the data of optical torque in Figure 4.12(a) and Eq. (4.11), we can obtain the rotational potentials for Rod 2 depending on the twisted angle at anti-bonding mode and bonding mode as shown in Figure 4.12(b). θ_0 is $\pi/2$ and 0 for the anti-bonding mode and bonding mode, respectively. The minimum values of potential energy identify the equilibrium positions of Rod 2 at the different plasmon modes. Due to the Brownian motion, the final angle of Rod 2 can not keep an exact value, which fluctuates around the angle determined by the minimum

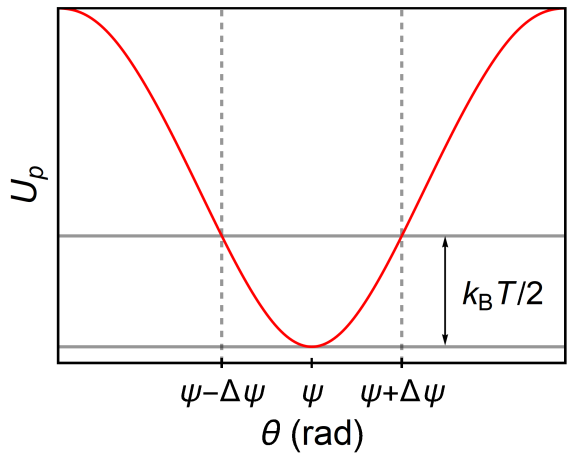

Figure 4.13: Schematic diagram for the calculation of angle fluctuation.

value of potential energy. To obtain the angle fluctuation, we compare the average energy of the Brownian motion with the potential energy and get two values of angle ($\psi \pm \Delta\psi$) as shown in Figure 4.13. In the range of $\psi - \Delta\psi$ to $\psi + \Delta\psi$, the potential energy is unable to overcome the Brownian motion. Therefore, $\pm\Delta\psi$ is regarded as the angle fluctuation. For an incident intensity of 10 mW/μm^2, the potential depths are more than 160 times as large as the Brownian motion energy $k_B T/2$. These potential wells enable the perpendicular and parallel alignments of the nanorods with angle fluctuations of $\sim \pm 4.2°$ and $\sim \pm 4.4°$, respectively.

We have discussed the different arrangements at different plasmon modes under the irradiation of y-polarized light. However, this can only be realized in two ways: perpendicular and parallel to each other by changing the incident wavelength. It can not produce the arrangements of the twisted nanorods in any other direction. To realize the full angle control of the arrangement, we introduce a new variable parameter, which is the polarization state of incident light as shown in Figure 4.14(a). By treating the optical torque and potential energy in the same way as we have introduced above, we can obtain the final equilibrium angle of Rod 2 under the irradiation of linearly polarized incident light with different polarization directions as shown in Figure 4.14(b). We can see, at the bonding mode, it can only realize the arrangement in a small angle range. Rod 2 is bound to the angle near the long axis of Rod 1 due to the strong enhanced interaction optical torque at the bonding mode comparing with the optical torque produced by the incident light.

However, at the anti-bonding mode, the final equilibrium angle of Rod 2 can be adjusted in a full angle range by changing the incident polarization state. In this case, the interaction optical torque can not be strongly enhanced, keeping a comparable magnitude to that of the optical torque produced by incident light. Thus, the balance between them can realize the full angle management of the arrangement. This provides an effective method to dynamically control the configuration of the nanorods.

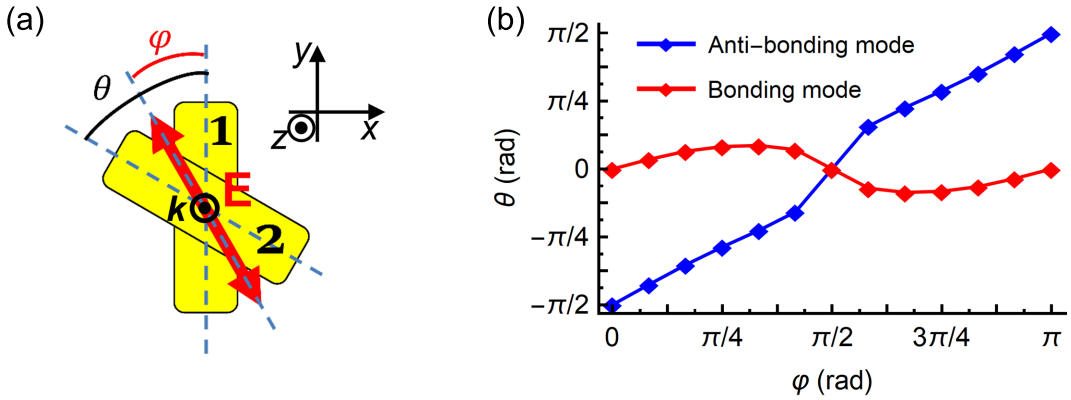

Figure 4.14: (a) Schematic diagram for twisted nanorods illuminated by linearly polarized light propagating along the z-axis from the positive to the negative direction. The polarization state is determined by the angle ϕ. (b) The final equilibrium angle θ of Rod 2 depending on the polarization angle ϕ of the incident light at the anti-bonding mode (λ = 930 nm) and bonding mode (λ = 1200 nm).

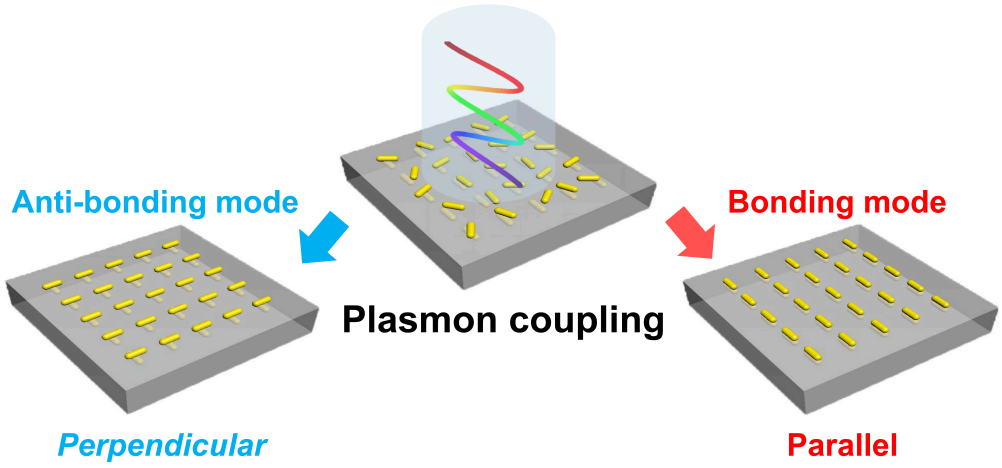

Figure 4.15: Concept of the experiment for optical arrangement.

To achieve such optical arrangements in a practical application, we propose a concept of the experiment as shown in Figure 4.15. Firstly, we can fabricate a nanorod array embedded in a transparent substrate, e.g., silicon dioxide, by etching trenches in the substrate. By controlling the depth of the trenches and the thickness of metal evaporated into the trenches, we can get a nanorod array a few nanometers below the surface of the substrate. The roughness of the surface can also be controlled within a few nanometers. Such fabrication has been realized by electron beam lithography and reactive ion etching in some previous studies already [39, 40]. This will also be introduced in detail and realized in Chapter 5. Then, we put nanorods dispersed in a solvent on the nanorod array. The dispersed nanorods would be aligned by controlling the wavelength and polarization state of the incident light.

4.4.4 Spin- and orbit-transfer torques between twisted nanorods

We now turn our attention to the origin of the interaction optical torque with regard to the transfers of spin and orbital angular momenta based on the analysis method proposed in Chapter 3. We calculated the spin- and orbit-transfer torques on each nanorod in the dimer as shown in Figure 4.16. Even though the incident light was linearly polarized light without any angular momenta, the interaction between two nanorods can generate spin and orbital angular momenta in the near field between them and produce interaction spin- and orbit-transfer torques on each nanorod. This indicates that spin-orbit interaction occurs in the narrow gap between the twisted nanorods. As the same as the total optical torque on each nanorod, the spin- and orbit-transfer torques also depend not only on the gap size but also on the twisted angle. From Figures 4.16(b) and 4.16(c), we can see the plasmon coupling between the twisted nanorod can enhance the interaction spin- and orbit-transfer torques and the enhancements increase with the decrease of the gap size due to the increase of plasmon coupling between the twisted nanorods. Comparing the total optical torque, spin-transfer torque, and orbit-transfer torque, we can find that the spin-transfer torque is the main contribution to the total optical torque at the bonding mode. However, at the anti-bonding mode, the spin-transfer torque and orbit-transfer torque provide almost equal contributions.

Additionally, we can see the spin-transfer torque is very large at the bonding mode

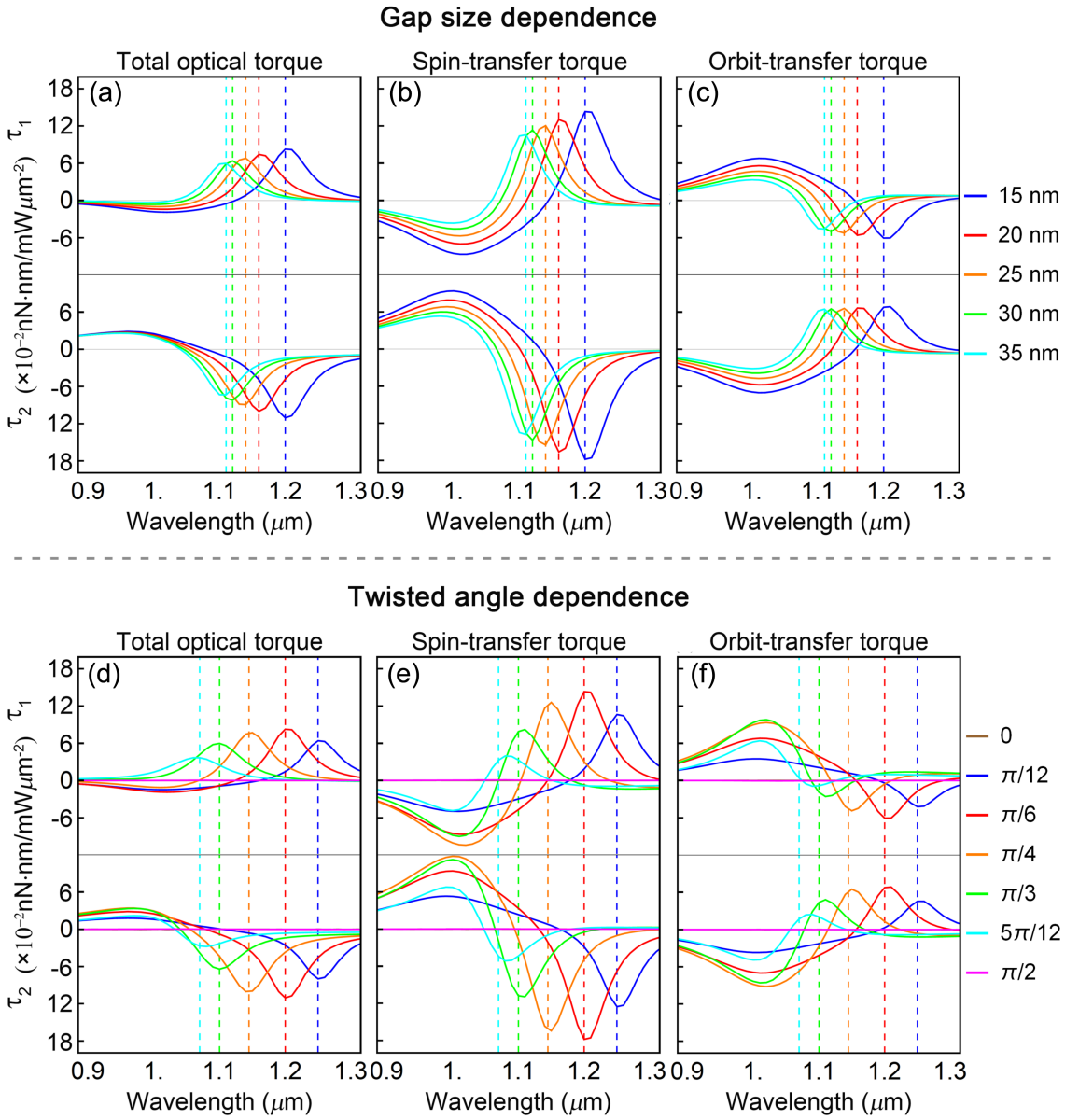

Figure 4.16: Gap size dependence of (a) total optical torque, (b) spin-transfer torque, and (c) orbit-transfer torque on each nanorod with the twisted angle fixed as $\pi/6$. Twisted angle dependence of (d) total optical torque, (e) spin-transfer torque, and (f) orbit-transfer torque on each nanorod with the gap size fixed as 15 nm

comparing with the orbit-transfer torque. When the gap size and twisted angle are small, in other words, in the range of strong plasmon coupling, the spin-transfer torque at the bonding mode is also larger than that at the anti-bonding mode. As introduced in Chapter 3, the spin-transfer torque is produced by the interaction of spin angular momentum between light and matter. This means the strong plasmon coupling can result in a strong interaction of spin angular momentum. Moreover, the interaction of spin angular momentum between light and matter can be related to the absorptions of the left- and right-handed circularly polarized light which induces the chiroptical response. Therefore, the results of spin-transfer torque on the twisted nanorods imply that the strong plasmon coupling can lead to a large chiroptical response of the twisted nanorods at the bonding mode. This may provide a new strategy for the enhancement of the chiroptical response of chiral plasmonic structures, which will be discussed in detail in Chapter 5.

4.5 Summary

In summary, we have presented a study of the interaction optical torque between twisted metal nanorods induced by plasmon coupling. Firstly, we have explained the physical description of plasmon coupling in the dimer using the theory of plasmon hybridization, which depends not only on the gap size but also on the twisted angle between the nanorods. This twisted angle dependence of plasmon coupling provides a new dimension to tune the plasmon coupling. Then, we have demonstrated the interaction optical torque is highly associated with the plasmon coupling by comparing the optical torques on the nanorods with the plasmon resonance spectra. At the same time, the dipole approximation method has also been applied to analyzed and confirmed the spectral behavior of the optical torque on each nanorod. The physical mechanism of the interaction optical torque can be clearly explained based on the plasmon-coupling-induced dipole moments in the nanorods. The optical torque behaviors are decided by the relative phase between the coupled dipole moments of the two nanorods. In order to show how one can apply our findings to practical experiments and applications, we have obtained the rotational potential energy by using the calculated optical torques on Rod 2 in comparison with the Brownian motion energy. When the two-coupled dipoles are in phase and out of phase, i.e.,

hybridized anti-bonding and bonding modes, their rotations lead to mutually perpendicular and parallel arrangements, respectively. Such arrangements can be extended to a full angle control by changing the polarization state of the incident light. In addition, we have discussed the experimental realization for the optical arrangement. The optical arrangements depending on the hybridized modes with the different wavelength excitations and the polarization states of the incident light will realize the dynamical contactless control of the plasmonic characteristics and functions, e.g., the EM field enhancement, plasmon resonance, and chirality, through the nanoparticle configurations with the plasmon coupling. Our findings will open a new route to all-optical active plasmonic and metamaterial devices, such as high-precision plasmonic nanodevices and nanomachines.

References

[1] R. A. Beth, "Mechanical detection and measurement of the angular momentum of light," *Phys. Rev.*, vol. 50, no. 2, pp. 115–125, 1936.

[2] D. Gao, W. Ding, M. Nieto-Vesperinas, X. Ding, M. Rahman, T. Zhang, C. Lim, and C.-W. Qiu, "Optical manipulation from the microscale to the nanoscale: fundamentals, advances and prospects," *Light: Sci. Appl.*, vol. 6, no. 9, pp. e17039–e17039, 2017.

[3] M. Padgett and R. Bowman, "Tweezers with a twist," *Nat. photonics*, vol. 5, no. 6, pp. 343–348, 2011.

[4] Y. E. Lee, K. H. Fung, D. Jin, and N. X. Fang, "Optical torque from enhanced scattering by multipolar plasmonic resonance," *Nanophotonics*, vol. 3, no. 6, pp. 343–350, 2014.

[5] A. Ashkin, "History of optical trapping and manipulation of small-neutral particle, atoms, and molecules," *IEEE J. Sel. Top. Quantum Electron.*, vol. 6, no. 6, pp. 841–856, 2000.

[6] M. Liu, T. Zentgraf, Y. Liu, G. Bartal, and X. Zhang, "Light-driven nanoscale plasmonic motors," *Nat. nanotechnol.*, vol. 5, no. 8, pp. 570–573, 2010.

[7] L. Shao, Z.-J. Yang, D. Andrén, P. Johansson, and M. Käll, "Gold nanorod rotary motors driven by resonant light scattering," *ACS Nano*, vol. 9, no. 12, pp. 12542–12551, 2015.

[8] M. Friese, T. Nieminen, N. Heckenberg, and H. Rubinsztein-Dunlop, "Optical alignment and spinning of laser-trapped microscopic particles," *Nature*, vol. 394, no. 6691, pp. 348–350, 1998.

[9] W. D. Phillips, "Nobel lecture: Laser cooling and trapping of neutral atoms," *Rev. Mod. Phys.*, vol. 70, no. 3, p. 721, 1998.

[10] S. Franke-Arnold, L. Allen, and M. Padgett, "Advances in optical angular momentum," *Laser Photonics Rev.*, vol. 2, no. 4, pp. 299–313, 2008.

[11] S. A. Maier, "Plasmonics: fundamentals and applications," 2007.

[12] V. Giannini, A. I. Fernández-Domínguez, S. C. Heck, and S. A. Maier, "Plasmonic nanoantennas: fundamentals and their use in controlling the radiative properties of nanoemitters," *Chem. Rev.*, vol. 111, no. 6, pp. 3888–3912, 2011.

[13] T. W. Odom and G. C. Schatz, "Introduction to plasmonics," *Chem. Rev.*, vol. 111, no. 6, pp. 3667–3668, 2011.

[14] S. R. Pocock, X. Xiao, P. A. Huidobro, and V. Giannini, "Topological plasmonic chain with retardation and radiative effects," *Acs Photonics*, vol. 5, no. 6, pp. 2271–2279, 2018.

[15] L. Gunnarsson, T. Rindzevicius, J. Prikulis, B. Kasemo, M. Käll, S. Zou, and G. C. Schatz, "Confined plasmons in nanofabricated single silver particle pairs: experimental observations of strong interparticle interactions," *J. Phys. Chem. B*, vol. 109, no. 3, pp. 1079–1087, 2005.

[16] W. Rechberger, A. Hohenau, A. Leitner, J. Krenn, B. Lamprecht, and F. Aussenegg, "Optical properties of two interacting gold nanoparticles," *Opt. Commun.*, vol. 220, no. 1-3, pp. 137–141, 2003.

[17] K.-H. Su, Q.-H. Wei, X. Zhang, J. Mock, D. R. Smith, and S. Schultz, "Interparticle coupling effects on plasmon resonances of nanogold particles," *Nano Lett.*, vol. 3, no. 8, pp. 1087–1090, 2003.

[18] E. Prodan, C. Radloff, N. J. Halas, and P. Nordlander, "A hybridization model for the plasmon response of complex nanostructures," *Science*, vol. 302, no. 5644, pp. 419–422, 2003.

[19] K. D. Osberg, N. Harris, T. Ozel, J. C. Ku, G. C. Schatz, and C. A. Mirkin, "Systematic study of antibonding modes in gold nanorod dimers and trimers," *Nano Lett.*, vol. 14, no. 12, pp. 6949–6954, 2014.

[20] P. Nordlander, C. Oubre, E. Prodan, K. Li, and M. Stockman, "Plasmon hybridization in nanoparticle dimers," *Nano Lett.*, vol. 4, no. 5, pp. 899–903, 2004.

[21] H. M. Abdulla, R. Thomas, and R. S. Swathi, "Overwhelming analogies between plasmon hybridization theory and molecular orbital theory revealed: The story of plasmonic heterodimers," *J. Phys. Chem. C*, vol. 122, no. 13, pp. 7382–7388, 2018.

[22] P. K. Jain, S. Eustis, and M. A. El-Sayed, "Plasmon coupling in nanorod assemblies: optical absorption, discrete dipole approximation simulation, and exciton-coupling model," *J. Phys. Chem. B*, vol. 110, no. 37, pp. 18243–18253, 2006.

[23] Z. Zhu, P. Yuan, S. Li, M. Garai, M. Hong, and Q.-H. Xu, "Plasmon-enhanced fluorescence in coupled nanostructures and applications in dna detection," *ACS Appl. Bio Mater.*, vol. 1, no. 1, pp. 118–124, 2018.

[24] J. R. Lakowicz, K. Ray, M. Chowdhury, H. Szmacinski, Y. Fu, J. Zhang, and K. Nowaczyk, "Plasmon-controlled fluorescence: a new paradigm in fluorescence spectroscopy," *Analyst*, vol. 133, no. 10, pp. 1308–1346, 2008.

[25] X. Huang, I. H. El-Sayed, W. Qian, and M. A. El-Sayed, "Cancer cells assemble and align gold nanorods conjugated to antibodies to produce highly enhanced, sharp, and polarized surface raman spectra: a potential cancer diagnostic marker," *Nano Lett.*, vol. 7, no. 6, pp. 1591–1597, 2007.

[26] B. Nikoobakht and M. A. El-Sayed, "Surface-enhanced raman scattering studies on aggregated gold nanorods," *J. Phys. Chem. A*, vol. 107, no. 18, pp. 3372–3378, 2003.

[27] P. K. Jain and M. A. El-Sayed, "Noble metal nanoparticle pairs: effect of medium for enhanced nanosensing," *Nano Lett.*, vol. 8, no. 12, pp. 4347–4352, 2008.

[28] S. S. Aćimović, M. P. Kreuzer, M. U. González, and R. Quidant, "Plasmon near-field coupling in metal dimers as a step toward single-molecule sensing," *ACS Nano*, vol. 3, no. 5, pp. 1231–1237, 2009.

[29] J. Butet, P.-F. Brevet, and O. J. Martin, "Optical second harmonic generation in plasmonic nanostructures: from fundamental principles to advanced applications," *ACS Nano*, vol. 9, no. 11, pp. 10545–10562, 2015.

[30] S. Kim, J. Jin, Y.-J. Kim, I.-Y. Park, Y. Kim, and S.-W. Kim, "High-harmonic generation by resonant plasmon field enhancement," *Nature*, vol. 453, no. 7196, pp. 757–760, 2008.

[31] H. Xu and M. Käll, "Surface-plasmon-enhanced optical forces in silver nanoaggregates," *Phys. Rev. Lett.*, vol. 89, no. 24, p. 246802, 2002.

[32] K. Wang, E. Schonbrun, and K. B. Crozier, "Propulsion of gold nanoparticles with surface plasmon polaritons: evidence of enhanced optical force from near-field coupling between gold particle and gold film," *Nano Lett.*, vol. 9, no. 7, pp. 2623–2629, 2009.

[33] Y. Tanaka, H. Yoshikawa, T. Itoh, and M. Ishikawa, "Surface enhanced raman scattering from pseudoisocyanine on ag nanoaggregates produced by optical trapping with a linearly polarized laser beam," *J. Phys. Chem. C*, vol. 113, no. 27, pp. 11856–11860, 2009.

[34] Y. Tanaka, H. Yoshikawa, T. Itoh, and M. Ishikawa, "Laser-induced self-assembly of silver nanoparticles via plasmonic interactions," *Opt. Express*, vol. 17, no. 21, pp. 18760–18767, 2009.

[35] A. J. Hallock, P. Redmond, and L. Brus, "Optical forces between metallic particles," *Proc. Natl. Acad. Sci. U. S. A.*, vol. 102, no. 5, pp. 1280–1284, 2005.

[36] J.-W. Liaw, W.-J. Lo, and M.-K. Kuo, "Wavelength-dependent longitudinal polarizability of gold nanorod on optical torques," *Opt. Express*, vol. 22, no. 9, pp. 10858–10867, 2014.

[37] H. Chen, W. Lu, X. Yu, C. Xue, S. Liu, and Z. Lin, "Optical torque on small chiral particles in generic optical fields," *Opt. Express*, vol. 25, no. 26, pp. 32867–32878, 2017.

[38] P. H. Jones, O. M. Maragò, and G. Volpe, "Optical tweezers: Principles and applications," 2015.

[39] Y. Zhao, M. Belkin, and A. Alù, "Twisted optical metamaterials for planarized ultrathin broadband circular polarizers," *Nat. Commun.*, vol. 3, no. 1, pp. 1–7, 2012.

[40] Y. Zhao, A. N. Askarpour, L. Sun, J. Shi, X. Li, and A. Alù, "Chirality detection of enantiomers using twisted optical metamaterials," *Nat. Commun.*, vol. 8, no. 1, pp. 1–8, 2017.

Chapter 5

Enhancement of g factor of twisted metal nanorods by plasmon coupling

5.1 Introduction

In Chapter 3, we have discussed the interaction of spin angular momentum separately from that of orbital angular momentum between light and matter via the produced spin-transfer torque and orbit-transfer torque. Whereafter, we have described the optical torque on the twisted nanorods in Chapter 4. It clearly shows the interaction optical torque, specifically the interaction spin-transfer torque, can be strongly enhanced by the plasmon coupling, which implies that the plasmon coupling can enhance the chiroptical response of the twisted nanorods.

As introduced in Chapter 1, the chiroptical response is induced by the different absorption of left- and right-handed circularly polarized light. It is quantflied by the g factor, i.e., Eq. (1.1), within the range from -2 to $+2$. However, the chiroptical response of most natural chiral materials is typically weak with a very small value of g factor: $< 10^{-3}$. Therefore, it is very difficult to detect the chiroptical response, which makes the study of this phenomenon tough and limits its further applications. In recent years, chiral plasmonic nanostructures have attracted widely scientific interest because they can strongly interact with circularly polarized light as well as with chiral molecules and can be designed to mimic the properties of chiral molecules [1–5]. The excitation of localized surface plasmon resonance (LSPR) of plasmonic nanostructure gives rise to an intense

field near the surface of the nanostructure and enhances the optical cross section in absorption [6]. Hence, the g factor of the chiral plasmonic nanostructure can be several orders of magnitude larger than that of natural material. For example, the Nam group fabricated a helicoid nanoparticles with a high g factor of 0.31 through a multi-chirality-evolution step synthesis method [7, 8]. With the development of nanotechnology, chiral plasmonic structures with large g factor have shown promising potential for detecting and sensing applications [9–11], negative refraction materials [12–14], and optical elements with strong chiroptical effects [15, 16]. Therefore, the study of the enhancement of g factor will be of great significance to improve the insights into controllable chirality of nanostructure and to expand its application. However, in the previous studies, almost all the studies of the g factor enhancement are limited to the geometry design of the structure.

The characteristics of a plasmonic system are determined by the shape and size of the individual nanoparticles, and the configuration of the nanoparticles, such as the distance between them and their orientations [17–20]. When two nanoparticles are close enough to each other, the plasmon modes of the individual particles hybridize to generate two new hybridized plasmon modes due to the coupling between them. At these hybridized modes, the plasmon functions, especially the enhancement of near-field, vary significantly with the nanoparticle configurations [21–23]. Intuitively, the configuration of nanoparticles in a chiral plasmonic system should be crucial in mediating its chiroptical response.

In this chapter, we investigate the chiroptical response based on the dimer of twisted metal nanorods. The dimer of twisted nanorods, one of the simplest 3D chiral plasmonic structures, has been widely used to study the chiroptical response [24–27]. However, these studies only considered the chiroptical response with very weak plasmon coupling between the nanorods or the circular differential scattering, which could not characterize the chiroptical response at the hybridized modes. Here, we concentrate on the chiroptical response of twisted nanorods at the hybridized bonding mode induced by the strong plasmon coupling, which depends on its configuration. We study the effects of the configuration parameters, e.g., gap size and twisted angle, in the dimer on its chiroptical response. As a proof of concept, we realize the fabrication of twisted gold nanorods with different gap sizes and twisted angles utilizing electron-beam (EB) lithography. We experimentally observe the hybridized modes induced by the plasmon coupling between

the twisted nanorods, which depends not only on the gap size but also on the twisted angle. We find that the chiroptical response can be enhanced by the plasmon coupling between the two nanorods and observe a very high g factor at the bonding mode due to the plasmon-coupling-induced strong near-field enhancement. We believe that the study of chiroptical response with the consideration of the plasmon coupling in the plasmonic structure provides an efficient route for designing chiral metamaterial with a highly enhanced chiroptical response.

5.2 Fabrication of twisted nanorods

In this section, we will introduce the fabrication processes of the twisted gold nanorods. We realized the fabrication of the twisted nanorods structures with different gap sizes and twisted angles embedded in silicon dioxide (SiO_2) using the top-down technique of EB lithography combined with layer-by-layer stacking. Figure 5.1(b) shows the scanning electron microscope (SEM) images of fabricated twisted gold nanorods structures with different twisted angles.

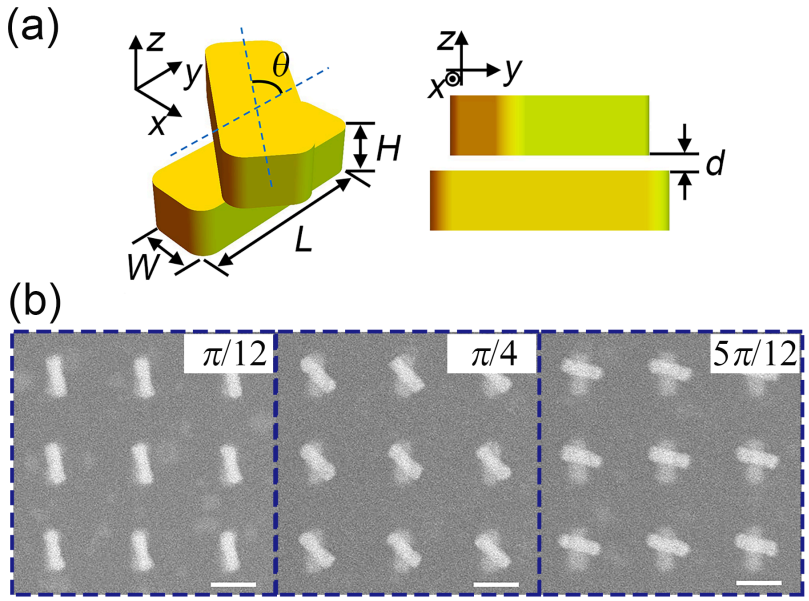

Figure 5.1: (a) Schematic illustration of the dimer of twisted gold nanorods with gap size d and twisted angle θ. (b) SEM images of the fabricated twisted nanorods structures with different twisted angles: $\pi/12$, $\pi/4$, and $5\pi/12$. Scale bar: 200 nm.

The fabrication can be divided into two steps: bottom layer fabrication and top layer fabrication, which mainly includes eight processes: substrate cleaning, sputtering, spin coating of resist, EB lithography, development, etching, evaporation, and lift-off. Next, we will introduce these processes in detail.

5.2.1 Bottom layer fabrication

Figure 5.2 describes the fabrication processes for the bottom layer fabrication. It includes the following steps.

Figure 5.2: Fabrication processes to realize the bottom layer of the twisted nanorods structure.

B1. *Substrate cleaning*

Before sputtering a dielectric layer on a substrate, we need to clean the substrate by using an ultrasonic cleaner to remove the dust on the substrate. Table 5.1 shows the specific conditions for substrate cleaning.

Table 5.1: Conditions for substrate cleaning

Acetone	3 min
Ethanol	3 min
Distilled water	3 min
Baking	110°C × 1 min

B2. *SiO_2 sputtering*

Sputtering refers to a process for thin film deposition. In order to ensure that the structure is surrounded by a homogenous medium, we deposited a 500 nm SiO_2 layer on the substrate (Ulvac SIH-450, Takeda super clean room, the University of Tokyo) as a dielectric layer.

B3. *Spin coating*

Resist is an electron-sensitive film on the surface of the sample. The solubility of the resist can be changed by the electron beam in the EB lithography process, enabling selective removal of either the exposed or non-exposed areas of the resist by immersing it in a developer. In our fabrication, we chose ZEP520A-7 as the resist. ZEP520A-7 is a high performance positive resist which will be removed in the beam exposure area. However, when EB lithography performs on insulating substrates, negative charge buildup can occur on the substrate surface causing beam deflection and thus pattern distortion. We solved this problem by spin coating Espacer (300Z) after the spin coating of resist. Espacer (300Z) is a kind of conductive polymer which can be simply applied by spin coating and simply removed by rinsing with water. Table 5.2 shows the specific conditions in the spin coating process.

Table 5.2: Conditions for spin coating

ZEP520A-7	300 rpm × 5 sec → 5000 rpm × 90 sec
Baking	120°C× 2 min
Espacer	1500 rpm × 60 sec

B4. *EB lithography*

EB lithography is a direct writing lithographic process that pattern is formed in a resist

layer by scanning with an electron beam. In our fabrication, we used the JEOL JBX-6300FS (Arakawa Lab., Institute of Industrial Science, the University of Tokyo) system for EB lithography. The pattern was written at a dose of 475 $\mu C/cm^2$ at an accelerating voltage of 100 kV.

B5. *Development*

After exposure in the EB lithography process, the designed pattern exists as a latent image in the resist layer. The exposed areas are chemically different from the non-exposed areas. The purpose of the development is to remove the exposed area (in the case of positive resists) of the resist by immersing it in a developer, resulting in the designed pattern in the resist layer. In our fabrication, the sample was developed in a developer (ZED-N50: n-Amyl acetate) for 20 sec and rinsed twice in ZED-B (Methyl isobutyl ketone 89% + Isopropyl alcohol 11%) for 5 sec.

B6. *SiO_2 etching*

SiO_2 etching is a process to make trenches in the SiO_2 layer. In this process, the designed pattern was transferred to the SiO_2 layer by inductively coupled plasma reactive ion etching (ICP-RIE Ulvac CE-300I, Takeda super clean room, the University of Tokyo) using the gas of CHF_3 to etch off 45 nm of SiO_2.

B7. *EB evaporation*

EB evaporation is a physical vapor deposition technique whereby a focused electron beam to heat source material (e.g. pellets of Au) and evaporates it within a vacuum environment. In our fabrication, a 2-nm titanium adhesion layer and 40 nm gold were sequentially deposited onto the sample (ULVAC EX-300, Arakawa Lab., Institute of Industrial Science, the University of Tokyo).

B8. *Lift-off*

Lift-off is a process for the removal of the resist layer in a solvent. The metal on the top of the resist will be removed along with the lift-off of the resist. Thus, the metal will only be deposited at sites that are not protected by the resist layer. In our case, the resist layer was removed by a remover (ZDMAC: Dimethylacetamide) on a hot plate at 80°C.

After these processes, we finished the bottom layer fabrication. It is important to note that the surface of the sample after the bottom layer fabrication should be very flat,

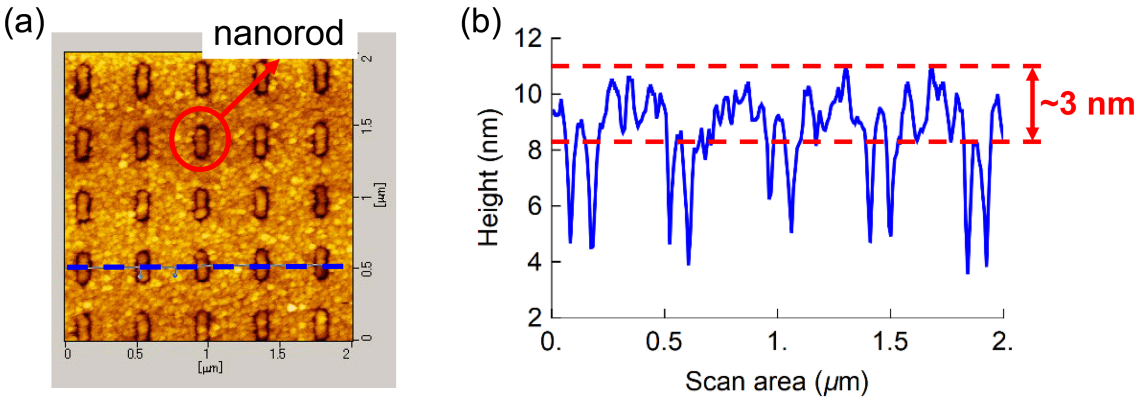

Figure 5.3: (a) AFM image of the sample after the bottom layer fabrication. (b) The surface profile to measure the flatness at the blue dashed line.

otherwise, we cannot fabricate the top layer well and it will be very difficult to control the gap size between the two layers. To obtain a flat surface, we should optimize the conditions in the etching and evaporation processes. In our fabrication, we made 45-nm-deep trenches in the SiO_2 layer in the etching process. A 2-nm titanium adhesion layer and a 40 nm gold layer was then deposited onto the sample using an EB evaporator. After the lift-off process, the gold nanorods were embedded in the trenches etched in the SiO_2 layer. Figure 5.3 shows the atomic force microscope (AFM) image of the sample after the bottom layer fabrication and corresponding surface profile to measure the flatness at the blue dashed line. We can see the peak to the valley of the surface is within about 7 nm and the peak of the surface to the top side of the nanorods is within 3 nm. This makes it is possible to control the gap size between the twisted nanorods within a very small error range.

5.2.2 Top layer fabrication

Figure 5.4 shows the fabrication processes for the top layer fabrication. In this step, we need to carefully consider the control of gap size and twisted angle between the two nanorods in the dimer.

T1. *SiO_2 sputtering*

After the bottom layer fabrication, we continued to sputter a 100 nm SiO_2 layer on the

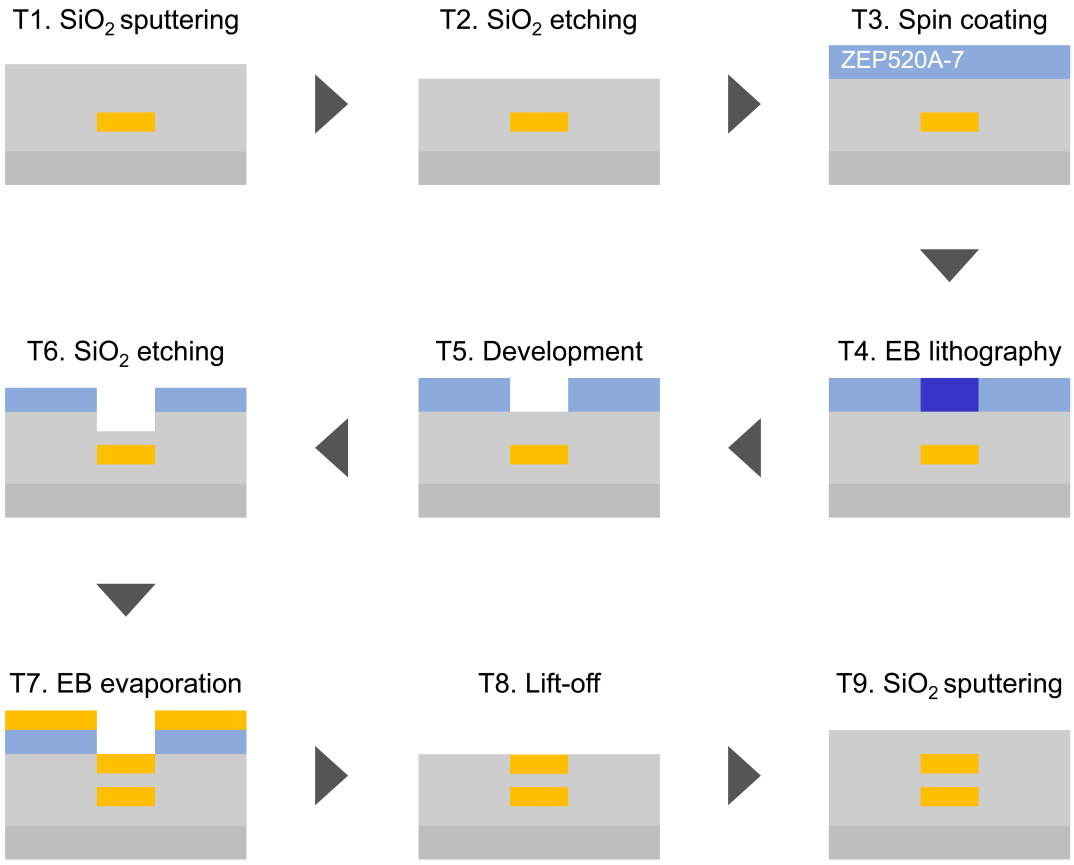

Figure 5.4: Fabrication processes to realize the top layer of the twisted nanorods structure.

sample as a dielectric layer for the top layer fabrication. This process can also facilitate the flattening of the sample surface.

T2. *SiO_2 etching*

In this etching process, the thickness of etched SiO_2 from the surface of the sample can be control by changing the etching time, so as to realize the control of gap size between the two layers.

T3. *Spin coating*

The same conditions as that in process B3.

T4. *EB lithography*

In this second EB lithography process, the twisted angle between the twisted nanorods can be controlled by designing the input pattern for the EB writing.

T5. *Development*, T6. *SiO_2 etching*, T7. *EB evaporation*, and T8. *Lift-off*

The same conditions as that in bottom layer fabrication.

T9. *SiO_2 sputtering*

We sputtered a 500 nm SiO_2 layer on the sample surface to cover the twisted nanorod structure to ensure that the structure is surrounded by a homogenous medium.

After the above processes, we finally realized the fabrication of twisted nanorods structure with different gap sizes and twisted angles.

5.3 Results and discussion

In this section, we will discuss the experimental results of the plasmon coupling and chiroptical response of the fabricated twisted gold nanorods. Figure 5.5 shows the experimental setup to collect the spectra. The incident light in our system was switchable among linearly, left- and right-handed circularly polarized light using a combination of a linear polarizer and a quarter-waveplate.

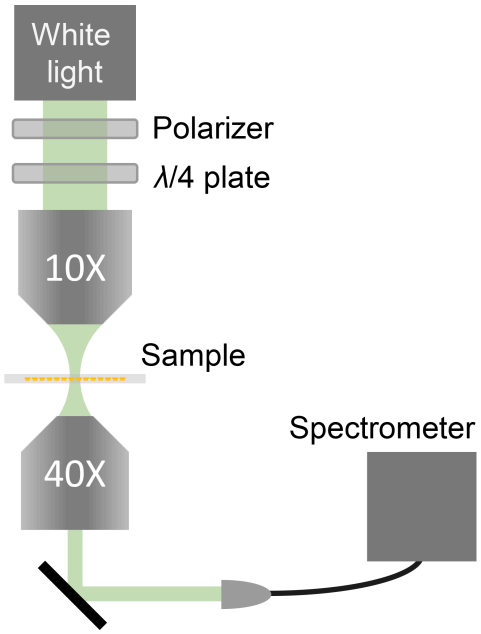

Figure 5.5: Schematic of the experimental setup for spectra collection.

5.3.1 Plasmon coupling between twisted nanorods

We start by considering the experimental results of the plasmon coupling between the twisted gold nanorods. The plasmon coupling was characterized by the extinction spectrum with y-polarized light (see the direction in Figure 5.1). The extinction spectrum can be obtained by [28]

$$A_{ext} = \frac{I_b(\lambda) - I_m(\lambda)}{I_b(\lambda)}, \tag{5.1}$$

where $I_m(\lambda)$ and $I_b(\lambda)$ are the spectra of the transmitted white light through substrates with and without nanostructures, respectively.

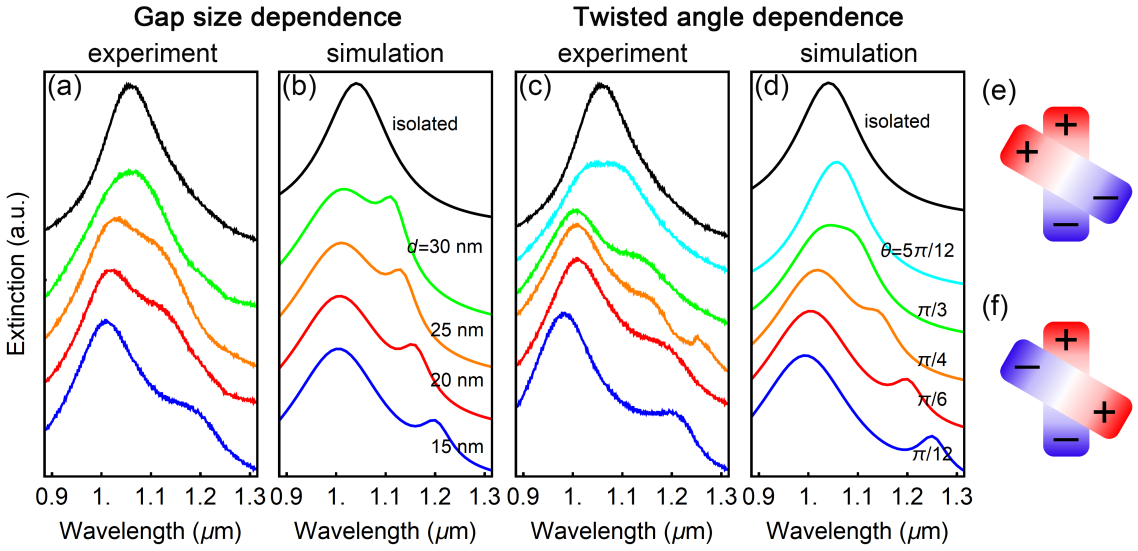

Figure 5.6: Experimental and simulation results of extinction spectra of an isolated nanorod and its dimers. (a) Gap size dependence ($\theta = \pi/6$) and (c) twisted angle dependence (d =15 nm) of extinction spectra recorded with incident y-polarized light. Panels (b) and (d) show the corresponding calculated spectra for the dimer comprised of gold nanorods with length × width × height dimension of 165 nm × 50 nm × 40 nm. Illustration of plasmon modes: (e) anti-bonding mode with in-phase dipoles in short wavelength range and (f) bonding mode with anti-phase dipoles in the long wavelength range.

In the dimer of twisted nanorods, the plasmon coupling is highly associated with its configuration, which is decided by the gap size d and twisted angle θ. Therefore, we experimentally characterized the plasmon coupling between the two nanorods with different gap sizes and twisted angles, as shown in Figure 5.6(a) and 5.6(c). In addition, these results were confirmed numerically in panels (b) and (d) using the finite element method (COMSOL Multiphysics). Based on these results, we can clearly observe the

plasmon coupling between the twisted nanorods. When two nanorods are close to each other, the resonance peak of isolated nanorod splits into two peaks due to the plasmon coupling between the two nanorods. With the decreases of the gap size and twisted angle, the two resonance peaks in short and long wavelength ranges shift to shorter and longer wavelengths than that of the resonance peak of the isolated nanorod, respectively. This indicates that the plasmon coupling increases with the decreases of the gap size and twisted angle. Therefore, we experimentally demonstrated that the plasmon coupling between the twisted nanorods depends not only on the gap size but also on the twisted angle. This is the first experimental demonstration for the twisted angle dependence of plasmon coupling, which provides a new dimension to tune the plasmon coupling.

A detailed explanation of the plasmon coupling between the twisted nanorods has been discussed in Chapter 4 (Subsection 4.3.2). The plasmon coupling between the two nanorods can be described by the theory of plasmon hybridization. In the dimer of twisted nanorods, the in-phase dipole coupling results in an anti-bonding mode as shown in Figure 5.6(e), which is a bright mode with a large cross section in the short wavelength range. However, the anti-phase dipole coupling leads to a bonding mode as shown in Figure 5.6(f), which is a dark mode with a small cross section but strongly enhanced near field in the long wavelength range.

5.3.2 *g* factor of twisted nanorods

We now turn our attention to the results of the g factor. For the characterization of the chiroptical response, we need to measure the g factor defined as Eq. (1.1). However, in contrast to the extinction spectrum, our setup does not allow measuring the absorption spectrum which is used in Eq. (1.1). It is known that the sum of the absorption cross section and the scattering cross section is referred to as the extinction cross section. Here, we focus on the chiroptical response at the bonding mode, which is a dark mode. The circular differential absorption is dominant compared with the circular differential scattering. Thus, in order to characterize the g factor, we define the quantity g_{ext} as

$$g_{ext} = \frac{A^l_{ext} - A^r_{ext}}{A^l_{ext} + A^r_{ext}}, \tag{5.2}$$

where A^l_{ext} and A^r_{ext} are the extinction spectrum for left- and right-handed circularly polarized light, respectively. Figure 5.7 shows the calculated $g_{ext}$and g_{abs} by using the finite element method with the designed parameters. Here, we put attention to the g factor at the hybridized bonding-mode, where the spectra of $g_{ext}$and g_{abs} show a similar shape and the same tendency.

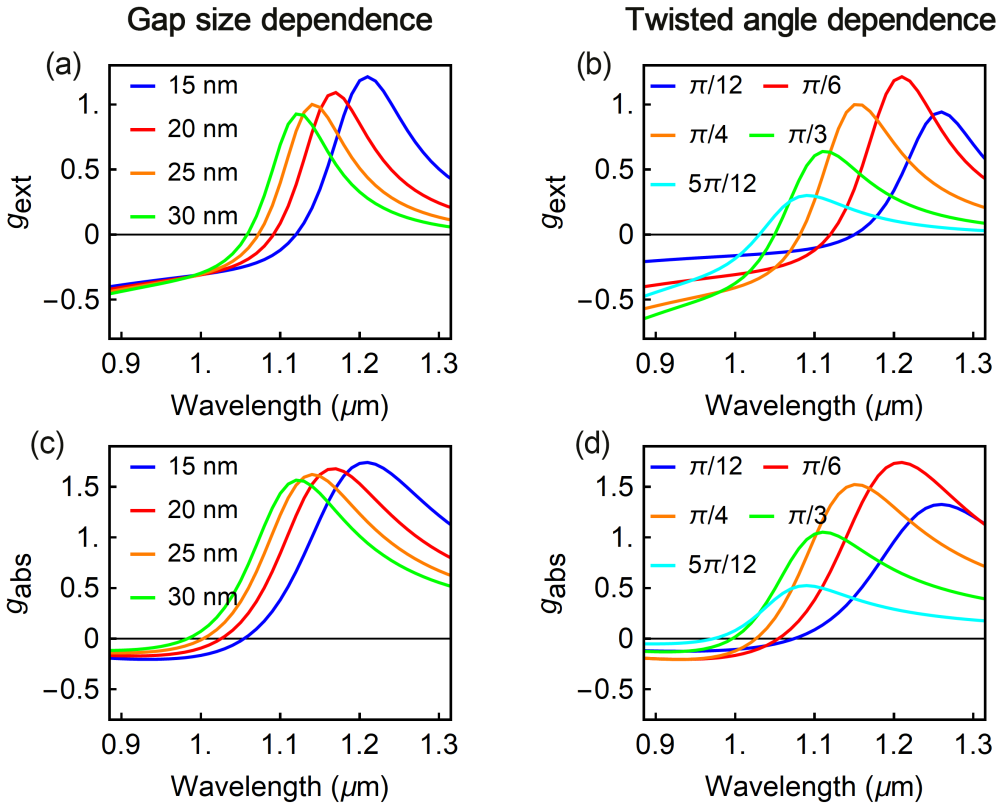

Figure 5.7: (a, c) Gap size dependence and (b, d) twisted angle dependence of g_{ext} and g_{abs} of twisted gold nanorods calculated using the finite element method (COMSOL Multiphysics) with the definitions of geometrical parameters: L = 165 nm, W = 50 nm, H = 40 nm.

Therefore, we first collected the extinction spectra of the dimer of twisted nanorods with incident left- and right-handed circularly polarized light as shown in Figure 5.8. The measured results were then substituted into Eq. (5.2) to calculate the g factor.

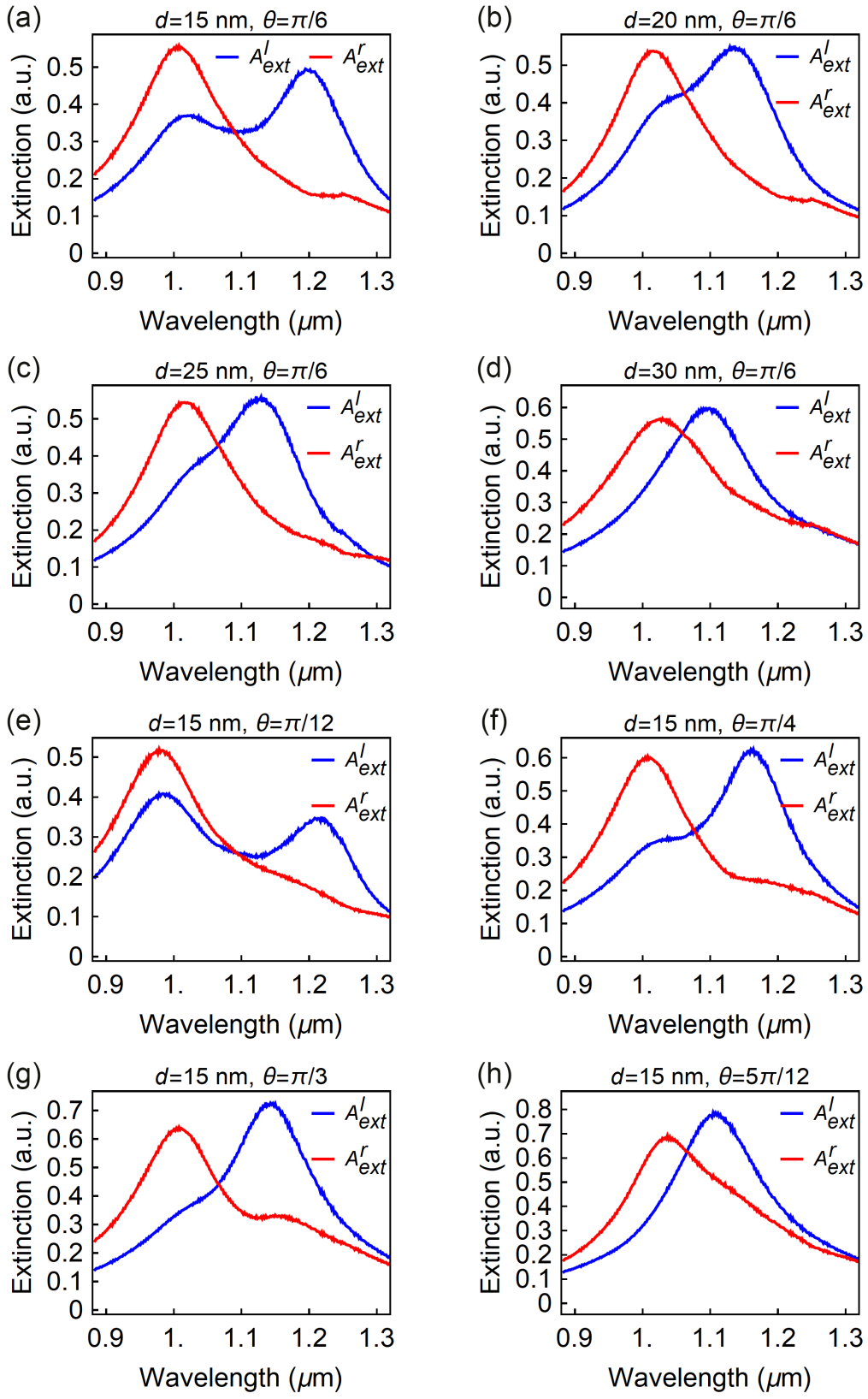

Figure 5.8: Measured extinction spectra recorded with incident left- and right-handed circularly polarized light of the dimer of twisted gold nanorods with different gap sizes and the twisted angles.

Figure 5.9 shows the experimental results of the g factor with different gap sizes and twisted angles. We can see that the g factor of the twisted nanorods is highly associated with both the gap size and twisted angle between the two nanorods. Besides, we can observe the opposite sign of g factor for the bonding mode and anti-bonding mode. At the bonding mode, the g factor exhibits a very large value. When the twisted angle is determined, the g factor increases with the decrease of gap size. For the twisted angle dependence, it also shows the same spectral behavior as that of the simulation results in Figure 5.7(b). These experimental results show a very good agreement with the simulation results in Figure 5.7.

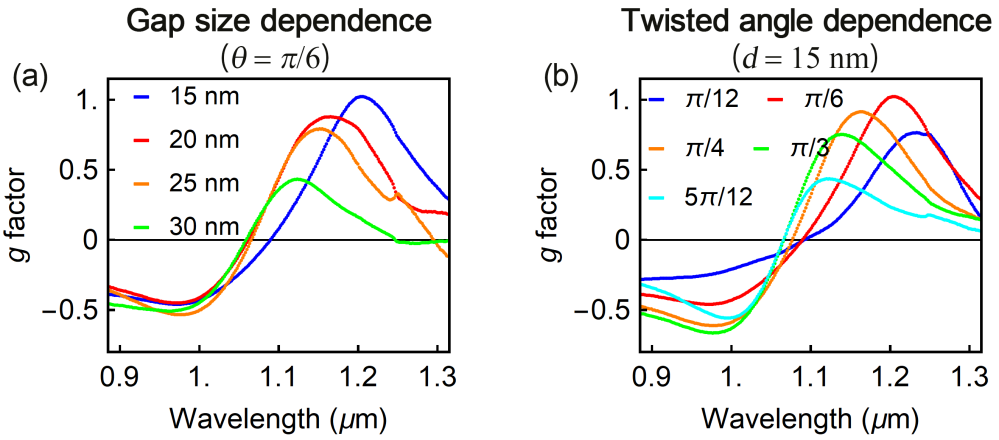

Figure 5.9: Experimental results of g factor of twisted gold nanorods with different (a) gap sizes with the fixed twisted angles of $\pi/6$ and (b) twisted angles with the fixed gap size of 15 nm.

The experimental value of the g factor reaches up to 1.03. This is orders of magnitude larger than that for most molecule system with g factor smaller than 10^{-3}. For a chiral molecule, the chiroptical response stems from the helical motion of displacement currents, which is induced by the interaction with circularly polarized light that causes the electron clouds of the molecule to move along helical paths. However, in the dimer of twisted gold nanorods, the interaction can excite real currents in the nanorods as well as the displacement currents between the nanorods. Compared to a molecule, the real currents and displacement currents in plasmonic structures are much stronger because of the massive free electrons in the metal nanoparticles. Hence, in a word, the strong chiroptical response of chiral plasmonic structures stems from the large dipole moments and currents

produced by the LSPR excitation.

Considering the g factor of the dimer of twisted nanorods, it is worth pointing out that the anti-bonding mode and bonding mode can be thought of as corresponding to different handedness. Meanwhile, circularly polarized light possesses the electromagnetic field with different handedness. Such an electromagnetic field can interact with the twisted nanorods by exciting plasmon modes. Therefore, the interaction between the nanorods in the dimer at different plasmon modes excited by left- and right-handedness circularly polarized light exhibits different strength due to the handedness matching (see Figure 5.8), resulting in the chiroptical response with the g factors of opposite sign at the two plasmon modes, as shown in Figures 5.9 as well as in Figures 5.7. Moreover, as we mentioned, the bonding mode is a dark plasmon mode, while the anti-bonding mode is a bright plasmon mode. The near-field enhancement at the bonding mode is much stronger than that at the anti-bonding mode, which leads to the larger g factor at the bonding mode than at the anti-bonding mode.

Compared with the previous studies on the chiroptical response of plasmonic structures, the strong plasmon coupling plays an important role in our work. We implemented the twisted nanorods structure with a small enough gap size to study the chiroptical response at the plasmon-coupling-induced hybridized mode. Owing to the plasmon coupling, the excited flow of real currents together with displacement currents in the structure can be strongly enhanced, resulting in the enhancement of chiroptical response. Therefore, we can obtain a much larger g factor than that in previous studies. For example, the Nam group realized a helicoid nanoparticles with a g factor of 0.31 [7].

5.3.3 *g* factor and plasmon coupling

In order to clear the direct relation between the g factor and the plasmon coupling in the dimer of twisted nanorod, we summarized the experimental results, as shown in Figure 5.10. It describes the maximum value of g factor we can obtain depending on the strength of plasmon coupling between the twisted nanorods. Here, the strength of the plasmon coupling was characterized by the separation between the resonance peaks of the bonding mode and anti-bonding mode. Based on the theory of plasmon hybridization, the bigger the separation, the stronger the plasmon coupling. For the gap size dependence

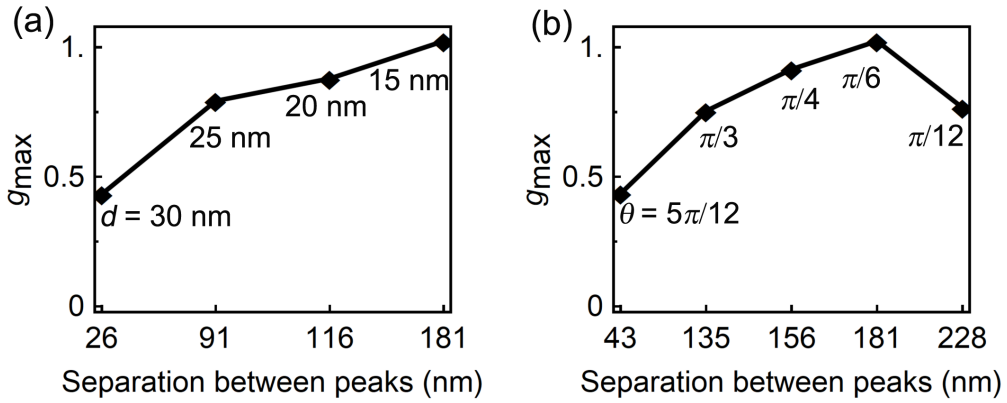

Figure 5.10: Summarized experimental results for the maximum value of g factor with different (a) gap sizes with the fixed twisted angle of $\pi/6$ and (b) twisted angles with the fixed gap size fixed of 15 nm, depending on the strength of plasmon coupling between the twisted nanorods. The strength of plasmon coupling is characterized by the separation between the resonance peaks of the bonding mode and anti-bonding mode.

(Figure 5.10(a)), when the twisted angle is determined, the plasmon coupling increases with the decrease of gap size. Accordingly, the maximum value of the g factor also increases. However, for the twisted angle dependence (Figure 5.10(b)), as the twisted angle decreases, the plasmon coupling increases when the gap size is determined. The maximum value of the g factor in our experiment was obtained at the twisted angle of $\pi/6$, while the strongest plasmon coupling was at the angle of $\pi/12$.

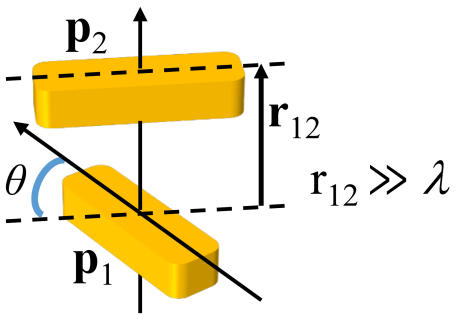

Figure 5.11: Schematic illustration of two dipoles produced by the twisted nanorods with center-to-center separation r_{12}.

To explain this, we first consider the g factor of twisted nanorods without plasmon coupling. In this case, the g factor can be related to the interaction strength and rota-

tional strength of the two dipoles produced by the two nanorods [29, 30]. For the twisted nanorods as shown in Figures 5.11, the interaction strength V_{12} and rotational strength R_{12} can be simply expressed as

$$V_{12} \propto \frac{1}{r_{12}^3}\mathbf{p}_1 \cdot \mathbf{p}_2 = \frac{1}{r_{12}^3}p_1 p_2 \cos\theta, \tag{5.3}$$

$$R_{12} \propto \pm\mathbf{r}_{12} \cdot (\mathbf{p}_1 \times \mathbf{p}_2) = r_{12} p_1 p_2 \sin\theta. \tag{5.4}$$

where $\mathbf{p}_1$ and $\mathbf{p}_2$ are the dipole moments of the two nanorods, $\mathbf{r}_{12}$ is the vector joining the centers of the two nanorods. The sign of R_{12} changes between the anti-bonding mode and bonding mode. As a result, the difference between the absorption of left- and right-handed circularly polarized lights is proportional to the product of V_{12} and R_{12}. Therefore, the g factor of the twisted nanorod can be simplified to be proportional to $\sin\theta\cos\theta$. This means that, without considering the plasmon coupling, the g factor of twisted nanorods has a maximum value at the twisted angle of $\pi/4$. Then, when the two nanorods are close to each other, plasmon coupling occurs. The plasmon coupling enhancement should be considered for the g factor. As we discussed in Subsection 5.3.1, the plasmon coupling increases with the decreases of gap size and twisted angle. Thus, the maximum value of g factor of the twisted nanorods increases with the decrease of gap size, and the twisted angle for the maximum value of g factor shifts from $\pi/4$ to a smaller angle.

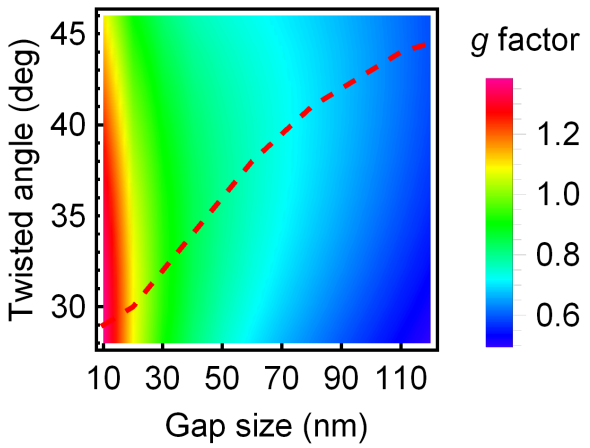

Figure 5.12: Optimization of g factor calculated using the finite element method (COMSOL Multiphysics). The red dashed line shows the twisted angle to obtain the maximum value of g factor at different gap sizes.

Figures 5.12 shows the optimization of g factor, which describes the maximum value of g factor at different gap sizes and twisted angles. The red dashed line shows the twisted angle to obtain the maximum value of g factor at different gap sizes. We can see that the maximum value of g factor increases with the decrease of gap size due to the increase of plasmon coupling. Besides, the twisted angle to obtain the maximum value of g factor shifts from $\pi/4$ to a smaller angle. These results also support the aforementioned analysis, which indicates that the plasmon coupling should be carefully considered for the enhancement of g factor.

5.4 Summary

In summary, we have studied the chiroptical response of the dimer of twisted nanorods concerning the plasmon coupling between the two nanorods. Firstly, we successfully fabricated the twisted gold nanorods structures with different gap sizes and twisted angles. Then, we experimentally characterized the plasmon coupling and g factor of the structures. We clearly observed the plasmon coupling between the twisted nanorods and demonstrated that the plasmon coupling highly depends not only on the gap size but also on the twisted angle between the nanorods. The demonstration of twisted angle dependence of plasmon coupling provides a new dimension to tune the plasmon coupling. What is more, due to the near-field enhancement induced by the plasmon coupling, the dimer of twisted nanorods shows a very strong chiroptical response with a large g factor at the hybridized bonding mode, which indicates that the plasmon coupling can enhance the g factor of chiral plasmonic structures and should be carefully considered for the enhancement of g factor. This designable chiroptical response depending on the configuration of the structure will pave the road for new metamaterials with modulated g factor distribution. We believe that the study of g factor at the hybridized plasmon mode provides a new perspective for the study of chirality and is generally applicable to other chiral plasmonic metamaterials for practical applications.

References

[1] M. Schäferling, *Chiral nanophotonics*. Switzerland: Springer, 2017.

[2] M. Hentschel, M. Schäferling, X. Duan, H. Giessen, and N. Liu, "Chiral plasmonics," *Sci. Adv.*, vol. 3, no. 5, p. e1602735, 2017.

[3] W. Du, X. Wen, D. Gérard, C.-W. Qiu, and Q. Xiong, "Chiral plasmonics and enhanced chiral light-matter interactions," *Sci. China: Phys., Mech. Astron.*, vol. 63, no. 4, p. 244201, 2020.

[4] M. Hentschel, M. Schäferling, T. Weiss, N. Liu, and H. Giessen, "Three-dimensional chiral plasmonic oligomers," *Nano Lett.*, vol. 12, no. 5, pp. 2542–2547, 2012.

[5] M. Kuwata-Gonokami, N. Saito, Y. Ino, M. Kauranen, K. Jefimovs, T. Vallius, J. Turunen, and Y. Svirko, "Giant optical activity in quasi-two-dimensional planar nanostructures," *Phys. Rev. Lett.*, vol. 95, no. 22, p. 227401, 2005.

[6] S. A. Maier, *Plasmonics: fundamentals and applications*. New York: Springer Science & Business Media, 2007.

[7] N. H. Cho, G. H. Byun, Y.-C. Lim, S. W. Im, H. Kim, H.-E. Lee, H.-Y. Ahn, and K. T. Nam, "Uniform chiral gap synthesis for high dissymmetry factor in single plasmonic gold nanoparticle," *ACS Nano*, vol. 14, no. 3, pp. 3595–3602, 2020.

[8] H.-E. Lee, H.-Y. Ahn, J. Mun, Y. Y. Lee, M. Kim, N. H. Cho, K. Chang, W. S. Kim, J. Rho, and K. T. Nam, "Amino-acid-and peptide-directed synthesis of chiral plasmonic gold nanoparticles," *Nature*, vol. 556, no. 7701, pp. 360–365, 2018.

[9] W. Li, Z. J. Coppens, L. V. Besteiro, W. Wang, A. O. Govorov, and J. Valentine, "Circularly polarized light detection with hot electrons in chiral plasmonic metamaterials," *Nat. Commun.*, vol. 6, no. 1, pp. 1–7, 2015.

[10] E. Hendry, T. Carpy, J. Johnston, M. Popland, R. Mikhaylovskiy, A. Lapthorn, S. Kelly, L. Barron, N. Gadegaard, and M. Kadodwala, "Ultrasensitive detection and characterization of biomolecules using superchiral fields," *Nat. Nanotechnol.*, vol. 5, no. 11, pp. 783–787, 2010.

[11] C. Jack, A. S. Karimullah, R. Leyman, R. Tullius, V. M. Rotello, G. Cooke, N. Gadegaard, L. D. Barron, and M. Kadodwala, "Biomacromolecular stereostructure mediates mode hybridization in chiral plasmonic nanostructures," *Nano Lett.*, vol. 16, no. 9, pp. 5806–5814, 2016.

[12] J. Pendry, "A chiral route to negative refraction," *Science*, vol. 306, no. 5700, pp. 1353–1355, 2004.

[13] S. Zhang, Y.-S. Park, J. Li, X. Lu, W. Zhang, and X. Zhang, "Negative refractive index in chiral metamaterials," *Phys. Rev. Lett.*, vol. 102, no. 2, p. 023901, 2009.

[14] E. Plum, J. Zhou, J. Dong, V. Fedotov, T. Koschny, C. Soukoulis, and N. Zheludev, "Metamaterial with negative index due to chirality," *Phys. Rev. B*, vol. 79, no. 3, p. 035407, 2009.

[15] N. Yu, F. Aieta, P. Genevet, M. A. Kats, Z. Gaburro, and F. Capasso, "A broadband, background-free quarter-wave plate based on plasmonic metasurfaces," *Nano Lett.*, vol. 12, no. 12, pp. 6328–6333, 2012.

[16] W. Ye, X. Yuan, C. Guo, J. Zhang, B. Yang, and S. Zhang, "Large chiroptical effects in planar chiral metamaterials," *Phys. Rev. Appl.*, vol. 7, no. 5, p. 054003, 2017.

[17] L. Gunnarsson, T. Rindzevicius, J. Prikulis, B. Kasemo, M. Käll, S. Zou, and G. C. Schatz, "Confined plasmons in nanofabricated single silver particle pairs: experimental observations of strong interparticle interactions," *J. Phys. Chem. B*, vol. 109, no. 3, pp. 1079–1087, 2005.

[18] W. Rechberger, A. Hohenau, A. Leitner, J. Krenn, B. Lamprecht, and F. Aussenegg, "Optical properties of two interacting gold nanoparticles," *Opt. Commun.*, vol. 220, no. 1-3, pp. 137–141, 2003.

[19] K.-H. Su, Q.-H. Wei, X. Zhang, J. Mock, D. R. Smith, and S. Schultz, "Interparticle coupling effects on plasmon resonances of nanogold particles," *Nano Lett.*, vol. 3, no. 8, pp. 1087–1090, 2003.

[20] E. Prodan, C. Radloff, N. J. Halas, and P. Nordlander, "A hybridization model for the plasmon response of complex nanostructures," *Science*, vol. 302, no. 5644, pp. 419–422, 2003.

[21] K. D. Osberg, N. Harris, T. Ozel, J. C. Ku, G. C. Schatz, and C. A. Mirkin, "Systematic study of antibonding modes in gold nanorod dimers and trimers," *Nano Lett.*, vol. 14, no. 12, pp. 6949–6954, 2014.

[22] P. Nordlander, C. Oubre, E. Prodan, K. Li, and M. Stockman, "Plasmon hybridization in nanoparticle dimers," *Nano Lett.*, vol. 4, no. 5, pp. 899–903, 2004.

[23] P. K. Jain, S. Eustis, and M. A. El-Sayed, "Plasmon coupling in nanorod assemblies: optical absorption, discrete dipole approximation simulation, and exciton-coupling model," *J. Phys. Chem. B*, vol. 110, no. 37, pp. 18243–18253, 2006.

[24] Y. Zhao, M. Belkin, and A. Alù, "Twisted optical metamaterials for planarized ultrathin broadband circular polarizers," *Nature Commun.*, vol. 3, no. 1, pp. 1–7, 2012.

[25] X. Lan, X. Lu, C. Shen, Y. Ke, W. Ni, and Q. Wang, "Au nanorod helical superstructures with designed chirality," *J. Am. Chem. Soc.*, vol. 137, no. 1, pp. 457–462, 2015.

[26] T. Liu, L. V. Besteiro, T. Liedl, M. A. Correa-Duarte, Z. Wang, and A. O. Govorov, "Chiral plasmonic nanocrystals for generation of hot electrons: toward polarization-sensitive photochemistry," *Nano Lett.*, vol. 19, no. 2, pp. 1395–1407, 2019.

[27] L.-Y. Wang, K. W. Smith, S. Dominguez-Medina, N. Moody, J. M. Olson, H. Zhang, W.-S. Chang, N. Kotov, and S. Link, "Circular differential scattering of single chiral

self-assembled gold nanorod dimers," *ACS Photonics*, vol. 2, no. 11, pp. 1602–1610, 2015.

[28] A. Movsesyan, A.-L. Baudrion, and P.-M. Adam, "Extinction measurements of metallic nanoparticles arrays as a way to explore the single nanoparticle plasmon resonances," *Opt. Express*, vol. 26, no. 5, pp. 6439–6445, 2018.

[29] B. Auguié, J. L. Alonso-Gómez, A. Guerrero-Martínez, and L. M. Liz-Marzán, "Fingers crossed: Optical activity of a chiral dimer of plasmonic nanorods," *J. Phys. Chem. Lett.*, vol. 2, no. 8, pp. 846–851, 2011.

[30] N. Berova, L. Di Bari, and G. Pescitelli, "Application of electronic circular dichroism in configurational and conformational analysis of organic compounds," *Chem. Soc. Rev.*, vol. 36, no. 6, pp. 914–931, 2007.

Chapter 6

Summary

In this dissertation, based on the three interesting phenomena in the interaction of angular momentum between light and plasmonic nanostructures: optical spin-orbit interaction, optical torque, and chiroptical response, we investigated the urgent issues in each phenomenon to improve the insights into the physics of light-matter interaction and to expand the further applications. In this chapter, we will summarize the results and describe the prospects.

■ Quantification of the optical spin-orbit transformation in light-matter interaction

We proposed a quantitative analysis method for the optical spin-orbit transformation in light-matter interaction, which is is a general method that can be applied to any size, shape, and constituent of matter in the presence of arbitrarily structured optical fields. We introduced a physical quantity called optical chirality density and reveal its relation with the spin angular momentum of the field. Based on this relation, we derived the continuity equation for spin angular momentum in analogy with the continuity equation for linear momentum. By combining with the continuity equation for total angular momentum, the transfers of spin and orbital angular momenta can be treated independently by considering the optical torques originated from them, which we called the spin-transfer torque and orbit-transfer torque. The separation of spin-transfer torque and orbit-transfer torque provides a quantitative analysis method for the optical spin-orbit transformation, which plays a significant role in analyzing and designing a spin-orbit interaction system.

We believe that the discovered results provide non-trivial insight into our understand-

ing of light-matter interactions. This new understanding of light-matter interaction will open a new avenue for the control of rotational states of nanoparticles and molecules, or the generation of light with specific states of spin angular momentum or orbital angular momentum.

■ Optical torque between twisted metal nanorods induced by plasmon coupling

We presented a systematic study of the interaction optical torque between twisted nanorods induced by plasmon coupling. We built a physical model of the dimer of twisted gold nanorods and start with the discussion of plasmon coupling between the twisted nanorods. The plasmon resonance spectra of the dimer indicate that the plasmon coupling depends not only on the gap size but also on the twisted angle. Then, we analyzed the interaction optical torque between the twisted nanorods with considering the plasmon coupling with them. The results show that the interaction optical torque can be enhanced by the plasmon coupling and can lead to mutually perpendicular and parallel arrangements of the two nanorods with the excitations of plasmon-coupling-induced anti-bonding mode and bonding mode, respectively. Additionally, such arrangements can be extended to a full angle control by changing the polarization state of the incident light. Besides, the discussion of spin- and orbit-transfer torques predicts that the strong plasmon coupling can lead to a large chiroptical response of the twisted nanorods at the bonding mode.

The twisted angle dependence of the plasmon coupling provides a new dimension to tune the plasmon coupling. Therefore, the optical arrangement depending on the wavelength and polarization state of the incident light makes it possible to control the plasmonic characteristics and functions dynamically and contactlessly. This shows a vast potential for the all-optical active plasmonic and metamaterial devices. For example, the precise arrangement of nanoparticles can be applied to make high-precision plasmonic nanodevices. Nanomachines are also possible that can switch conformations or functions with different incident light.

■ Enhancement of *g* factor of twisted metal nanorods by plasmon coupling

We experimentally demonstrated that the plasmon coupling can enhance the *g* factor of the dimer of twisted gold nanorods. Inspired by the result in the second topic, we fabricated

the structures of twisted gold nanorods with different gap sizes and twisted angles. The plasmon coupling and g factor were characterized to study the relation between them. We experimentally demonstrated that the plasmon coupling depends not only on the gap size but also on the twisted angle. The g factor at the hybridized bonding mode exhibits a large value (~ 1.03) due to the plasmon-coupling-induced strong near-field enhancement. The experimental results show a good agreement with the theoretical predictions. It was found that the plasmon coupling should be carefully considered to obtain a large g factor in a chiral plasmonic system.

We believe that the study of g factor enhancement concerning the plasmon coupling provides a new efficient route for the study of chiral plasmonic structures. We anticipate that our study will aid in the design of chiral plasmonic structures for use in metamaterial applications. For example, the metamaterials with large chiroptical effect can be applied to the optical elements. For the chirality detection of molecular, the detection signal can be strongly enhanced by the plasmonic structures with a large g factor. Strong chirality of chiral metamaterials can also realize the negative refractive index.

Publication list

■ Papers on Scientific Journals

1. An'an Wu, Yoshito Y. Tanaka, and Tsutomu Shimura,
"Plasmon-hybridization-induced optical torque between twisted metal nanorods",
Optics Express,**28**, 2398-2410 (2020).

2. An'an Wu, Yoshito Y. Tanaka, Ryoma Fukuhara, and Tsutomu Shimura,
"Continuity equation for spin angular momentum in relation to optical chirality",
Physical Review A,**102**, 023531 (2020).

3. An'an Wu, Yoshito Y. Tanaka, and Tsutomu Shimura,
"Plasmon-coupling-enhanced dissymmetry factor of twisted metal nanorods",
In preparation.

■ Presentations at International Conference

1. An'an Wu, Yoshito Y. Tanaka, Ryoma Fukuhara, and Tsutomu Shimura,
"Interaction optical torque between twisted metal nanorods through surface plasmon coupling",
Optical Trapping and Optical Micromanipulation XVI (SPIE), 11083-116, San Diego, United States (2019).

2. An'an Wu, Yoshito Y. Tanaka, Ryoma Fukuhara, and Tsutomu Shimura,
"Interaction optical torque between twisted nanorods with plasmon hybridization",
The International Symposium on Plasmonics and Nano-photonics, P22, Kobe, Japan (2019).

■ Presentations at Domestic Conference

1. An'an Wu, Yoshito Tanaka, Ryoma Fukuhara, and Tsutomu Shimura,
"Surface plasmon enhanced optical torque between twisted nanorods",
The 79th JSAP Autumn Meeting, 18p-231C-8, Nagoya, Japan (2018).

2. An'an Wu, and Yoshito Tanaka,
"Surface-plasmon-enhanced optical torque between twisted nanorods",
新学術領域研究「光圧によるナノ物質操作と秩序の創生」第 3 回公開シンポジウム, P40, Nagoya, Japan (2019).

3. An'an Wu, Yoshito Tanaka, Ryoma Fukuhara, and Tsutomu Shimura, "Optical spin-transfer torque calculated in relation with optical chirality", The 80th JSAP Autumn Meeting, 18a-E204-7, Hokkaido, Japan (2019).

■ Scholarship

1. 日本政府（文部科学省）奨学金 (2017.04–2020.03).
2. 東京大学外国人支援基金 (2020.04–2020.12).